C 1

# A SEISMIC REFRACTION STUDY OF THE QUEEN CHARLOTTE FAULT ZONE

by

SONYA ASTRID DEHLER

B.Sc.(Geophysics), The University of Calgary, 1983

A THESIS SUBMITTED IN PARTIAL FULFILLMENT OF

THE REQUIREMENTS FOR THE DEGREE OF

MASTER OF SCIENCE

in

THE FACULTY OF GRADUATE STUDIES

Department of Geophysics and Astronomy

We accept this thesis as conforming

to the required standard

THE UNIVERSITY OF BRITISH COLUMBIA

April 1986



78

In presenting this thesis in partial fulfilment of the requirements for an advanced degree at the University of British Columbia, I agree that the Library shall make it freely available for reference and study. I further agree that permission for extensive copying of this thesis for scholarly purposes may be granted by the head of my department or by his or her representatives. It is understood that copying or publication of this thesis for financial gain shall not be allowed without my written permission.

Department of GEOPHYSICS & ASTRONOMY

The University of British Columbia
1956 Main Mall
Vancouver, Canada
V6T 1Y3

Date 30 April 1986

## ABSTRACT

The margin between the continental North American and oceanic Pacific plates west of the Queen Charlotte Islands is uniquely marked by an active transform fault zone. The region is the locus of oblique convergence between the two lithospheric plates. West of the fault zone the absent continental shelf is replaced by a 25 km wide scarp–bounded terrace at 2 km depth which separates the oceanic and continental crust.

An onshore–offshore seismic refraction survey was carried out in 1983 across the Queen Charlotte Islands region. Thirty–two explosive charges and several airgun lines were recorded on eleven land–based and six ocean–bottom instruments. A subset of the resulting data set was chosen to study the structure of the Queen Charlotte Fault zone and adjacent terrace.

Two–dimensional ray tracing and synthetic seismogram modelling produced a velocity structural model of the fault region. Underlying the deformed terrace sediments is an upper 3 km thick faulted unit with velocity 3.8 km/s and a high gradient. The lower crustal region is on average 10 km thick and has velocity 5.3 km/s and a slightly lower gradient. Beneath this unit the Moho increases in dip from 5° to 19° eastward. The terrace velocities are anomalously low compared to the adjacent oceanic and continental crustal structures. Velocities of the oceanic crust are consistent with those observed in ophiolite sequences. The velocity structure of the continental crust is not well–defined; however, vertical offset of 1.1 km is seismically observed on the Rennell–Louscoone Fault on Moresby Island.

Two tectonic mechanisms are proposed to explain the anomalous terrace structure. Subduction of the oceanic lithosphere beneath the terrace would accrete sediments to the seaward edge of the terrace and subduct material beneath it. Upthrusting of terrace

material along near–vertical fault planes would result from compression at the transform fault above an inactive subduction zone. A combination or alternation of the two mechanisms would explain the observed fault zone structure.

# TABLE OF CONTENTS

# LIST OF TABLES

# LIST OF FIGURES

## ACKNOWLEDGEMENTS

*To my parents with gratitude for their years of love, support, and encouragement.*

I would like to thank my supervisor, Dr. Ron M. Clowes, for his support and guidance over the years and the many helpful discussions which kept me "on track". I would also like to thank Dr. Robert M. Ellis for critically reviewing this thesis.

I am greatly indebted to Bob Meldrum for his patient and thorough explanations of the more technical (and mystical) aspects of this study. My thanks also go to David Mackie for his invaluable assistance with the processing, and to many others who helped with the thesis, in particular Joane Bérubé, Jeff Drew, Chris Pike, Alex von Breymann, and Barry Zelt.

The members of the department (faculty, staff, and students) have made this an enjoyable place to study. My thanks to all of them for their friendship.

Financial support for data acquisition and analysis was provided by NSERC through Operating Grant A7707 and Strategic (Oceans) Grant G0738, and by D.S.S. contracts 05SU.23235-3-1089 from the Earth Physics Branch, E.M.R., and 06SB.23227-4-0904 from the Pacific Geoscience Centre, E.M.R. Also, E.M.R. Research Agreement 287 provided support in 1983/84. Additional support was provided by Chevron Canada Resources Ltd. and Shell Canada Resources Ltd.

# CHAPTER I INTRODUCTION

The Queen Charlotte Fault zone marks the active boundary west of central British Columbia, Canada, between the North American and Pacific lithospheric plates. Coincident with the fault zone between 52° and 54° is the western margin of the Queen Charlotte Islands (figure 1). The transition across the margin is structurally complex, a product of the long and complicated geologic history of the region. A brief review of this history will provide a tectonic framework for newly developed structural models.

## 1.1 Regional Geotectonic History

### 1.1.1 Terrane accretion

Much of the North American Cordillera is composed of "suspect" terranes of uncertain paleogeographic origins (figure 2). Most of these terranes are allochthonous to North America and were accreted to the cratonic margin as a result of plate interactions (Coney et al., 1980). The Queen Charlotte Islands and immediate vicinity are underlain by two such terranes, Alexander and Wrangellia.

The Alexander terrane is a continental edge fragment (Coney et al., 1980) consisting of a complex assemblage of volcanic, clastic, and limestone rocks of primarily Late Precambrian to Late Paleozoic age (approximately 650 to 250 Ma). Wrangellia is a submarine arc complex composed of Middle to Upper Triassic tholeiitic basalts and calcareous sedimentary rocks and Early to Middle Jurassic terrigenous clastics and volcanics (Coney et al., 1980). Wrangellia terrane rocks are represented on the Queen Charlotte Islands by the Karmutsen, Kunga, Maude, and Yakoun Formations (Yorath and Chase, 1981; Sutherland Brown, 1968).

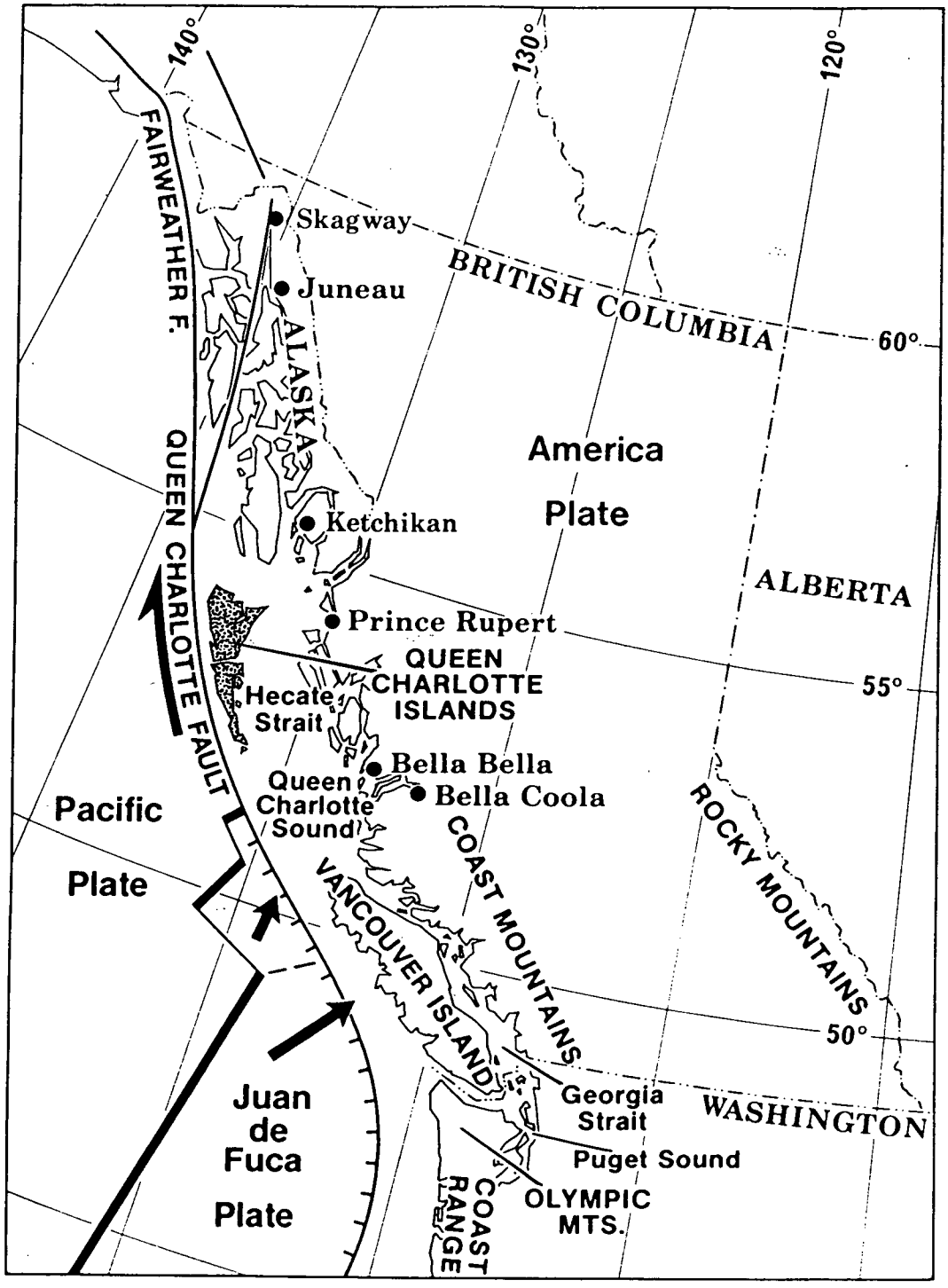


**Figure 1.** Plate tectonics off Canada's west coast (after Riddihough, 1982a).

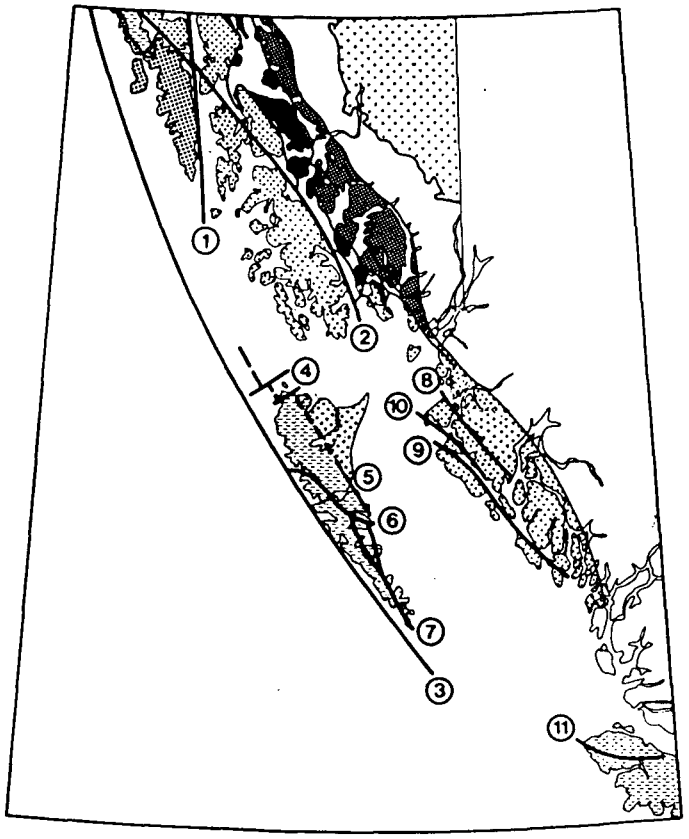


CHUGACH TERRANE — Cretaceous sediments and mélange

TRACY ARM TERRANE — Central Gneiss complex: Late Mesozoic and Cenozoic plutons of Coast Plutonic Complex

GRAVINA - NUTZOTIN BELT — Jurrassic and Cretaceous arc volcanics and sediments

TAKU TERRANE — Upper Paleozoic to Triassic volcanics, sediments

WRANGELLIA — Late Triassic to Jurassic volcanics, sediments, Paleozoic basement

STIKINE TERRANE — Late Paleozoic to Jurassic volcanics, sediments

ALEXANDER TERRANE — Paleozoic volcanics, sediments, plutonic rocks

③ Faults —

1. Chatham Strait Fault
2. Clarence Strait Fault
3. Queen Charlotte Fault
4. Beresford Bay and Langara Faults
5. Sandspit Fault
6. Rennell Sound Fault
7. Louscoone Inlet Fault
8. Grenville Channel Fault
9. Principe Laredo Fault
10. Kitkalta Fault
11. Holberg Fault

**Figure 2.** Suspect terranes of the Queen Charlotte Islands region (after Yorath and Chase, 1981).

Both terranes are believed to have moved northwards from their places of origin before accreting to North America. Paleomagnetic studies (van der Voo et al., 1980) indicate that Alexander terrane moved 1800 km northwards with respect to cratonic North America during Late Carboniferous and Triassic time (300 to 180 Ma). Wrangellia is believed to have originated within approximately 15° of the paleo-equator (in either the northern hemisphere or the southern hemisphere, the latter more favoured by Irving, 1979, and Hilde et al., 1977) and subsequently travelled between 3000 and 6300 km northwards.

Wrangellia collided with the western edge of Alexander terrane during Middle to Late Jurassic time (170 to 130 Ma) along a suture zone marked by the present Sandspit Fault on the Queen Charlotte Islands and Rennell Sound Fault through Hecate Strait (figure 2). During the collision the terranes were uplifted and intruded by plutons dated at 144 Ma (Young, 1981). The amalgamated superterrane collided with the westward moving North America plate in the Late Cretaceous or Early Tertiary period (90 to 40 Ma) resulting in plutonic uplift of the Coast Mountains and a westward jump of the active continental margin to the seaward edge of the terrane (Yorath and Cameron, 1982).

### 1.1.2 Plate interactions

The concept of seafloor spreading has enabled researchers to reconstruct plate motions and interactions off western North America using magnetic anomalies, hot spot traces, and paleomagnetism (eg. Atwater,1970; Coney, 1970; Stone,1977; and Riddihough, 1982b). All models propose convergence and strike-slip faulting along the

margin for the past 100 Ma, although the details of the interactions do not always agree.

A generalized plate motion reconstruction presented by Riddihough (1982b) shows the types and rates of past plate interactions off western Canada (figure 3). Three plates interacted with the America (A) plate: the Pacific (P) plate, the Kula (K) plate which once existed north of the Pacific plate, and the large Farallon (F) plate east of the Pacific plate. During the Middle to Late Cretaceous (100 to 80 Ma) the Farallon plate interacted in a generally north to northeast direction with the America plate at an estimated rate of 60 to 120 mm/a. By Late Cretaceous to Eocene time (80 to 40 Ma) the rate had increased to 120 to 170 mm/a in a northeast direction. The Kula plate was obliquely converging at 100 to 150 mm/a with the America plate at this time and the K–F–A triple junction was migrating either southwards along the coast from Alaska (Stone, 1977) or northwards from southern California (Atwater, 1970) to a position near Vancouver Island. In Late Eocene time (45 to 40 Ma) the Pacific plate changed its direction of motion by 50°, as indicated by the bend in the Emperor–Hawaii chain, resulting in a reduction of all interaction rates across the North American margin by one–half (Riddihough, 1982b).

During the Oligocene to Early Miocene (40 to 20 Ma) a number of plate adjustments occurred as a southern part of the P–F spreading ridge started subducting beneath California, and transcurrent motion was initiated between 30 and 20 Ma along the San Andreas Fault (Atwater, 1970). The northern part of the Farallon plate broke off and began to move independently as the Juan de Fuca (J) plate around 20 Ma ago. The K–F–A triple junction had meanwhile continued migrating rapidly northwards along the margin and the remainder of the Kula plate was subducted during this time.

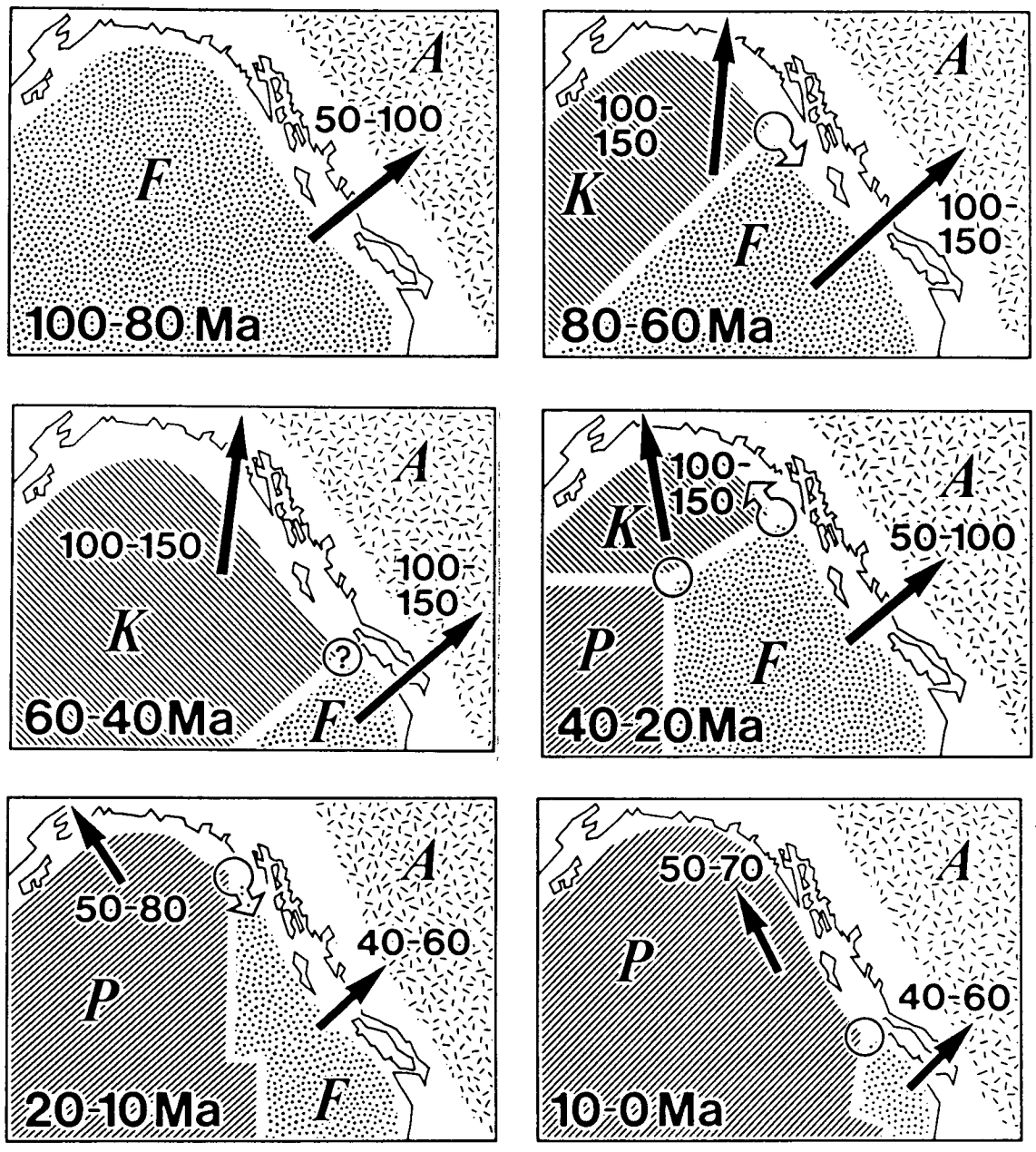


**Figure 3.** Plate interactions off western Canada during the last 100 Ma (Riddihough, 1982b). P – Pacific plate, A – America plate, K – Kula plate, and F – Farallon plate. Arrows indicate relative directions of motion; rates of motion in mm/yr are shown.

During the Miocene (20 to 10 Ma) the Juan de Fuca plate continued subducting beneath the America plate at 40 to 60 mm/a in a northeastward direction and the Pacific plate moved northwestward at 50 to 60 mm/a, producing transcurrent motion along a paleo- Queen Charlotte Fault at the America plate margin. The P-J-A triple junction migrated southeastwards along the margin during this time and may have been responsible for the initiation of rifting in Queen Charlotte Sound 17 Ma ago which eventually shifted and rotated the Queen Charlotte Islands along reactivated faults to their present position (Yorath and Chase, 1981; Horn, 1982). Alternatively, the America plate may have overridden a hot spot or mantle plume which caused the rifting and produced the Anahim volcanic belt of central British Columbia (Yorath and Cameron, 1982; Yorath and Chase, 1981).

Finally, the Pliocene and Pleistocene (10 to 0 Ma) saw the stabilization of the P-J-A triple junction off northern Vancouver Island and a decrease in the J-A convergence rate to 40 mm/a as the spreading direction at the Juan de Fuca ridge changed (Riddihough, 1977). New spreading ridges were formed at Dellwood Knolls 1 Ma ago and Tuzo Wilson Knolls 0.5 Ma ago and joined to the stable triple junction by transform faults (Riddihough et al., 1980). Spreading at the Tuzo Wilson Knolls caused the Queen Charlotte Fault to jump landwards to its present location where it is currently active (Hyndman and Ellis, 1981).

## 1.2 Present Tectonic Regime

### 1.2.1 Geologic setting

The Queen Charlotte Islands were divided by Sutherland Brown (1968) into three physiographic units: the Queen Charlotte Ranges, Skidegate Plateau, and the Queen

Charlotte Lowlands (figure 4). The regions differ not only in physiographic features but also in geologic composition, as the 1100 m high Ranges are underlain by granitic and Tertiary volcanic rocks, the 600 m high Plateau by slightly-tilted Jurassic volcanic, Cretaceous sedimentary, and Early Tertiary basaltic rocks, and the 150 m high Lowland by complex sequences of rocks from Jurassic to Pleistocene age (Sutherland Brown, 1968).

The boundaries of the physiographic units generally follow two major northwest-trending fault systems, the Rennell Sound—Louscoone Inlet Fault and the Sandspit Fault (figure 2). The Rennell-Louscoone Fault strikes N25°W in the south and N50°W north of Louise Island. The fault zone is composed of several associated strands that dip between 75° northeastward and 90° vertical. Total fault displacement since Late Jurassic is estimated as 600 to 3000 m downwards and 19 to 93 km southward for the east block relative to the west block (Sutherland Brown, 1968).

The Sandspit Fault strikes uniformly N37°W and dips at 65° northeastward. The fault zone separates older rocks in the west block from younger formations in the east and cuts through plutons of Cretaceous age. Total fault displacement is estimated as thousands of metres downward for the east block relative to the west and unknown but presumably considerable horizontal offset (Sutherland Brown, 1968).

The major faults on the islands are colinear with the Queen Charlotte Fault located at the foot of the continental shelf just offshore. The continental shelf is generally less than 5 km wide west of the Queen Charlotte Islands and is little more than a notch in the wide, steep continental slope.

The slope is composed of three parts: a steep upper scarp, a middle terrace plateau, and a lower scarp. The upper scarp has a gradient of up to 20° and includes the

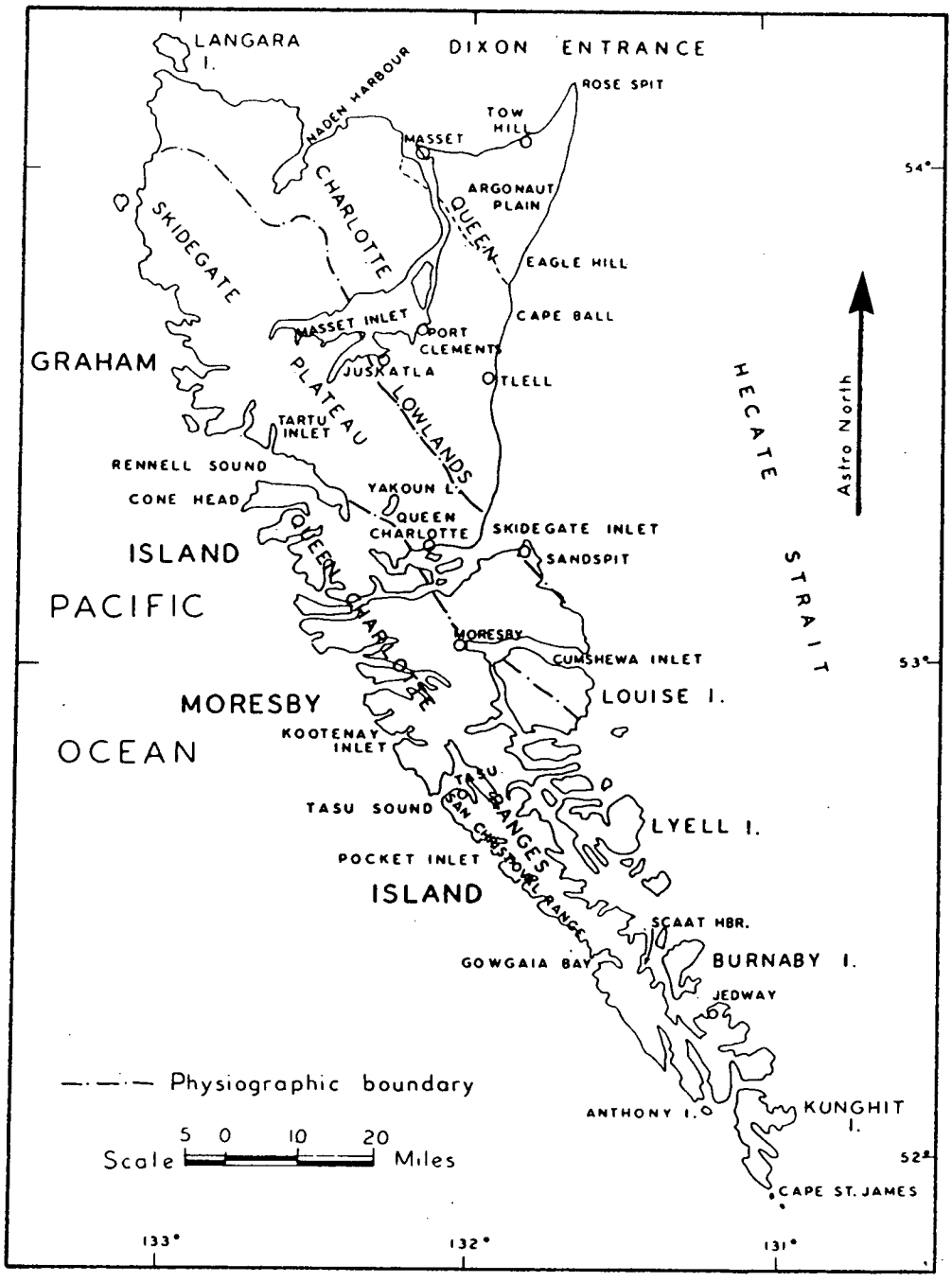


**Figure 4.** Physiographic location map of the Queen Charlotte Islands (Sutherland Brown, 1968).

truncated spurs of the Insular Mountains at the coast. The terrace is at an average depth of 2 km and has variable topography which becomes more rugged towards its termination off southern Moresby Island. The lower scarp slopes as steeply as 23° (Chase and Tiffin, 1972).

The physiography and geology of the continental slope and shelf appear to be linked to past and present interaction between the Pacific and America plates at the Queen Charlotte Fault zone.

### 1.2.2 Geophysical studies

Present motion at the Queen Charlotte Fault zone is primarily dextral strike–slip at an average rate of about 55 mm/a (eg. Atwater, 1970; Keen and Hyndman,1979; Hyndman and Weichert, 1983). The strike of the fault zone west of Moresby Island, as obtained from its morphology and seismicity, is over 10° different from the more easterly relative plate motion predicted by global plate models (Minster and Jordan, 1978). This suggests that convergence at 10 to 20 mm/a is occurring at the fault zone as subduction of the Pacific plate beneath the Queen Charlotte Islands and/or as crustal deformation of the islands and adjacent region (Hyndman and Ellis, 1981; Yorath and Hyndman, 1983).

The active fault has been located by recent microseismicity studies (Hyndman and Ellis, 1981; Bérubé, 1985) as being beneath the upper fault scarp of the continental slope. Composite P–nodal fault plane solutions for earthquake clusters indicate primarily strike–slip motion along the fault west of Graham Island and some thrusting and vertical faulting with ocean side down west of Moresby Island (Bérubé, 1985). This is consistent with studies of large earthquakes which determined strike–slip motion with a

small thrust component for the 1949 magnitude 8.1 earthquake west of Graham Island and a strike-slip mechanism with a significant thrust component along a fault plane dipping 50° eastward for the 1970 magnitude 7.0 earthquake just south of Moresby Island (Rogers, 1983).

Seismic reflection profiles across the fault zone reveal the effect of compression and strike-slip movement on the continental margin (eg. Chase and Tiffin, 1972; Chase et al., 1975; P.D. Snavely, unpublished data). The terrace region of the continental slope is underlain by grabens and synclines infilled with deformed sediments (figure 5). The steep upper scarp is the currently active Queen Charlotte Fault and the outer scarp is presumed to be the former fault location. Seismic reflections from oceanic basement end abruptly at the outer scarp, as do magnetic lineations from the oceanic crust (Currie et al., 1980). Tectonic faulting, possibly associated with trench formation, could be destroying the remnant magnetization of the crustal rocks at the edge of the terrace (Srivastava, 1973).

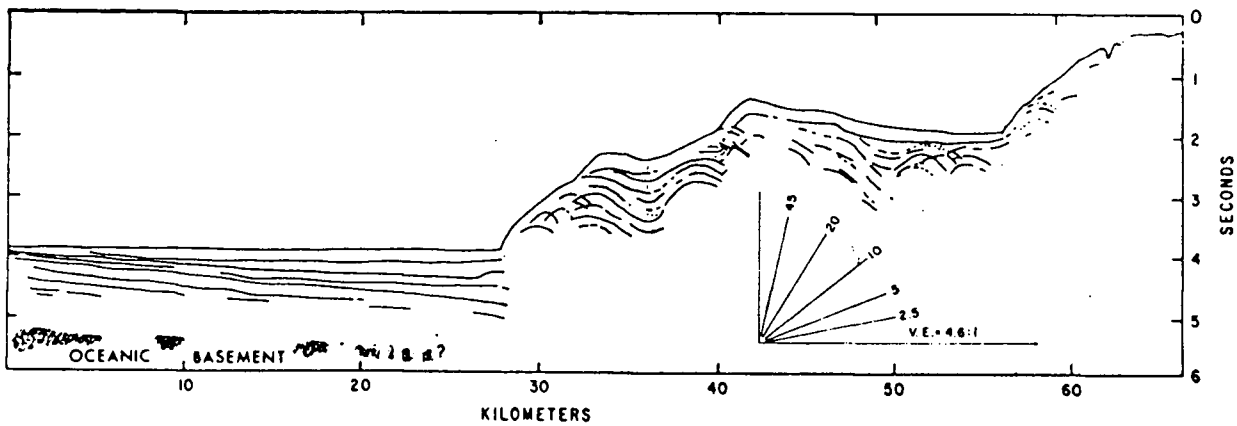


**Figure 5.** Line drawing interpretation of a CSP profile west of northern Moresby Island (Chase and Tiffin, 1972).

Heat flow and gravity profiles of the oceanic crust also show dramatic changes as they cross over the fault zones and terrace to the continent. A sharp decrease in heat flow at the seaward edge of the terrace was observed by Hyndman et al. (1982). They also noted a general decrease in heat flow by a factor of three from the axis of the Queen Charlotte Trough to 40 km inland, consistent with measurements in many subduction zones. The low terrace heat flow was attributed to tectonic thickening of sediments, possibly by accretion, and the underthrusting of cold oceanic lithosphere (Hyndman et al., 1982).

Free-air gravity data indicate a large negative anomaly at the base of the continental slope and a positive anomaly on the landward side of the continental shelf (eg. Couch, 1969; Dehlinger et al., 1970; Srivastava, 1973; Currie et al., 1980). The gravity low over the terrace may be due to a thick prism of sediments or unusually thick crust (Currie et al., 1980). The gravity profile is again characteristic of subduction zones (Keen and Hyndman, 1979).

A lithospheric flexural model for the Queen Charlotte Islands region, developed by Yorath and Hyndman (1983), agrees well with most of the geophysical and physiographic observations (figure 6). Uplift at the edge of the continental lithosphere and depression of the adjacent area inland, a flexural response to underthrusting, have been observed and described by Riddihough (1982a) in the Queen Charlotte Islands region. The corresponding flexural bulging of the oceanic lithosphere is observed on bathymetric maps as the Oshawa Rise (figure 7). The subduction process would produce a thick accretionary wedge of sediments in the vicinity of the continental slope terrace. These sediments would be faulted and deformed by the additional transform motion, as would the crust beneath them.

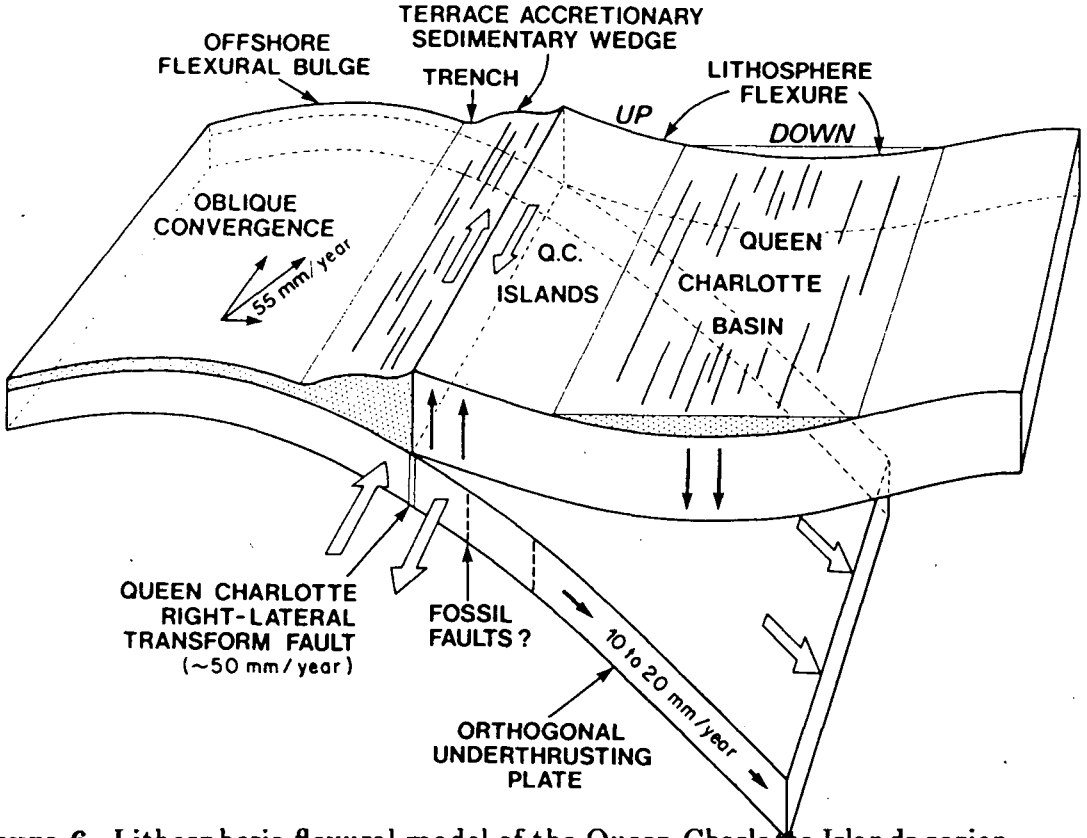


**Figure 6.** Lithospheric flexural model of the Queen Charlotte Islands region (Yorath and Hyndman, 1983).

Seismic refraction models developed for the region support underthrusting of the Pacific plate beneath the Queen Charlotte Islands as a possible convergence mechanism (Mackie, 1985; Horn et al., 1984; Horn, 1982; Bird, 1981). The model of Horn et al. (1984) indicates anomalously low velocities and high gradients in the terrace region separating the oceanic and continental blocks (figure 8); the model is consistent with an accretionary wedge of compressed sediments overlying a subducting oceanic crust. The subduction and transform motion at the continental margin and the variable geotectonic history appear to have created a unique and complex structure at the fault zone.

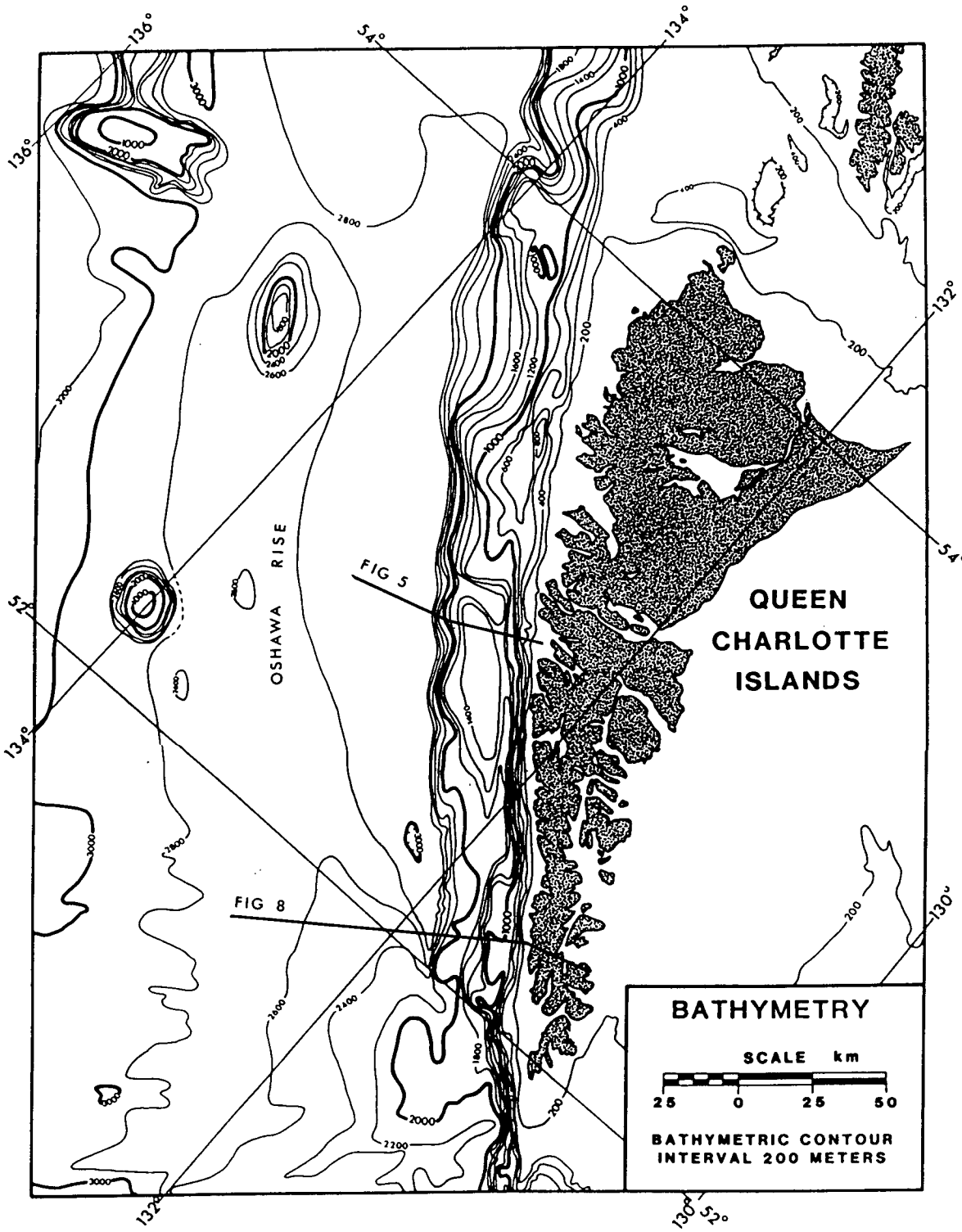


**Figure 7.** Bathymetry west of the Queen Charlotte Islands. The locations of the CSP linedrawing of figure 5 and the refraction model of figure 8 are shown.

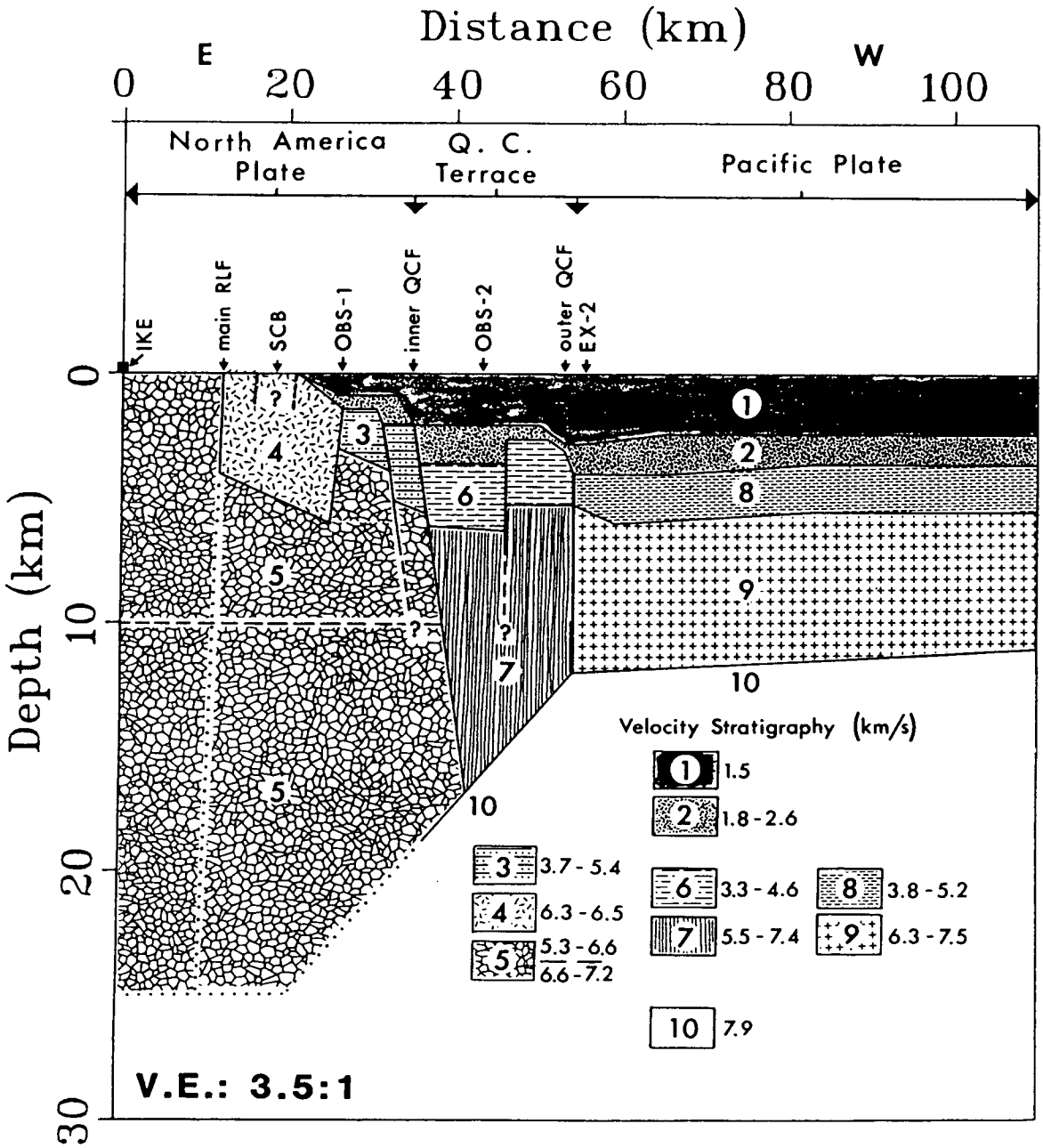


**Figure 8.** Velocity structural model of Horn et al. (1984) from a seismic profile off southern Moresby Island.

## 1.3 Experimental Objectives

As the previous discussion has indicated, the structure at the junction of the Pacific and America plates is very complex. Geophysical observations across the continental margin indicate that a thick wedge of sediments may be accreting to the margin as a result of subduction of the Pacific plate. At the same time, dextral transform motion along the active fault plane is pushing the accretion zone northwards and deforming the sediments and underlying crust.

A seismic refraction experiment was designed to study the structure of the terrace region that marks the active plate boundary west of the Queen Charlotte Islands, and to try to determine the origin and composition of the terrace. To achieve these objectives it is necessary to look at the structural transition from the oceanic crust west of the terrace to the continental crust beneath the Queen Charlotte Islands.

# CHAPTER II DATA ACQUISITION AND PROCESSING

## 2.1 The Refraction Experiment

A major marine-land seismic refraction survey was carried out in August 1983 by the University of British Columbia (UBC) in collaboration with the Earth Physics Branch, Ottawa, and the Pacific Geoscience Centre, Sidney. A 330 km profile was recorded from the deep ocean across northern Moresby Island and Hecate Strait to the mainland of British Columbia (figure 9). The experimental objectives were to determine the structure of the sediment, crust, and lithosphere (1) of the Queen Charlotte transform fault zone, (2) beneath the Queen Charlotte Islands, and (3) below Hecate Strait.

A total of seventeen seismographs were deployed: two ocean bottom seismographs (OBSs) west of the Queen Charlotte Islands, eight land-based seismographs (LBSs) on the Islands, four OBSs in Hecate Strait, and three additional LBSs on the mainland. Two types of energy source were used. The pelleted TNT explosive NITROPEL$^{\bigcirc}$ packed into drums with primacord and C.I.L. Procore Primers$^{\bigcirc}$ was detonated every 3.4 km along a 110 km line bearing southwest from northern Moresby Island. Twelve 540 kg and twenty 60 kg shots were fired, with two of the small shots following each large shot. Three additional refraction profiles, one over the western OBSs and two in Hecate Strait, were shot using a 32 litre ( 2000 $in^3$ ) airgun with a shot spacing of approximately 0.18 km.

This study of the structure of the Queen Charlotte Fault zone will focus on the airgun profile west of the Queen Charlotte Islands and the explosion profile as recorded by the ten westernmost receivers.

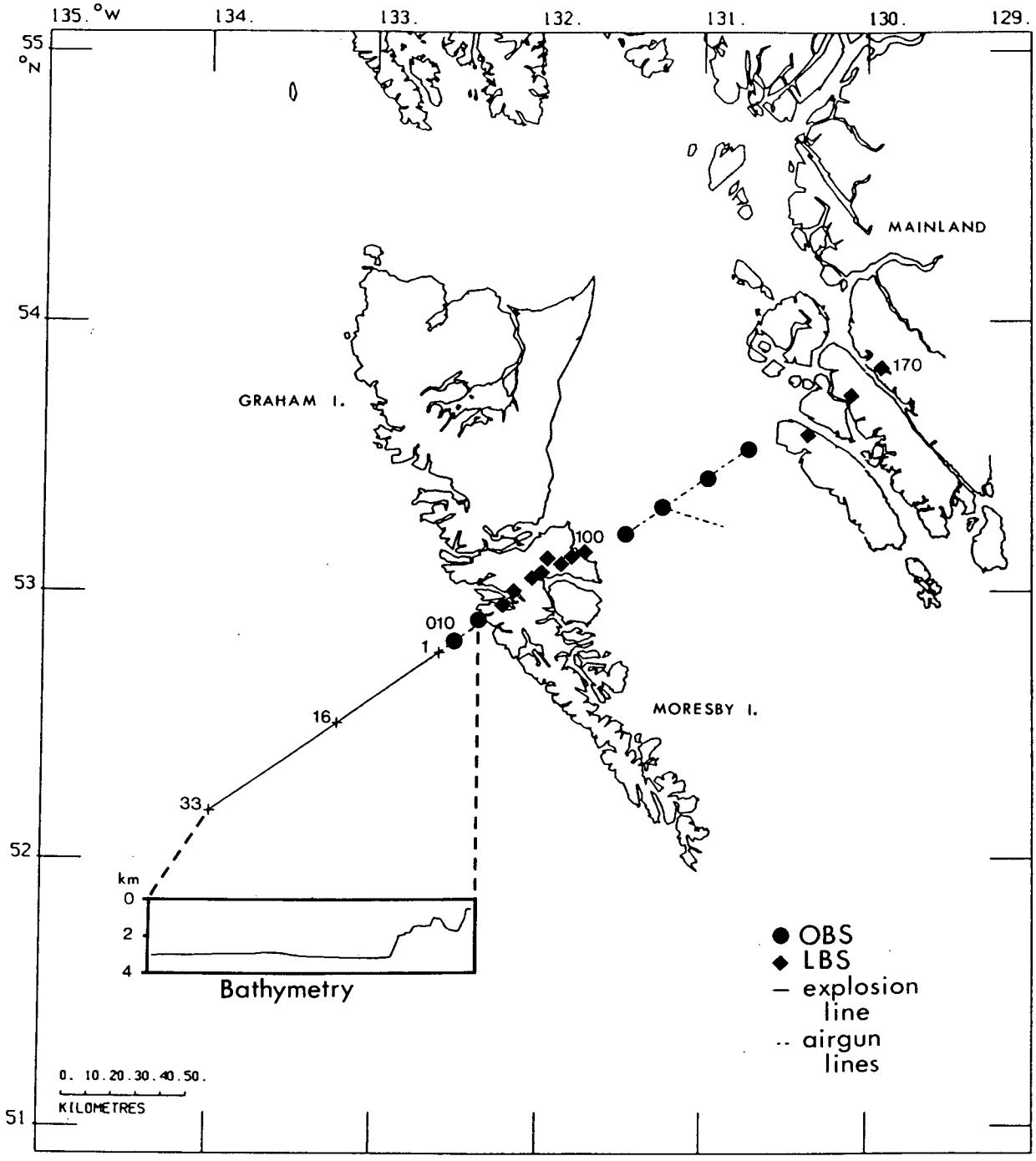


Figure 9. Location of receivers and survey lines in the 1983 refraction experiment. Three of the 540 kg explosion locations (1, 16, 33) are indicated as are receiver locations 010, 100, and 170.

## 2.2 Instrumentation

Four types of seismographs were deployed during the survey (table I). The six OBSs, UBC-modified versions of Atlantic Geoscience Centre instruments (Heffler and Barret, 1979), consist of a frame holding a flotation sphere, an instrument pressure case, a hydrophone, recovery devices, and a detachable weight to take the package to the ocean bottom. Inside the pressure case are gimbaled 4.5 Hz horizontal and vertical component geophones, primary and secondary clocks, a microprocessor, a 4-channel slow-speed direct record analog tape recorder, and the necessary power supplies. The outputs from the geophones and hydrophone were recorded together with an internally-generated 10 Hz amplitude-modulated time code directly onto cassette tapes.

Six Earth Physics Branch (EPB) Mark II digitally recording "Backpack" seismographs were deployed on Moresby Island and the mainland. The Backpacks sampled the output from a 2 Hz vertical component seismometer at 60 samples per second (sps) and recorded on digital cassettes. An internal clock provided timing for the data.

Four digitally recording UBC Microcorders were deployed on Moresby Island. The output from a 1 Hz vertical component seismometer was sampled at 60 sps and recorded on digital cassette tape. Timing was by an internal clock.

The last site on Moresby Island was occupied by a UBC FM analog recorder. It contained 1 Hz vertical and horizontal component seismometers and recorded their output at high and low gain settings together with WWVB time code on five parallel tracks of 7-track analog tape.

The seismographs successfully recorded all shots during the experiment.

| *INSTRUMENT TYPE* | *RECEIVER NUMBER* | *LOCATION* |
|---|---|---|
| *OBS* | *010* | *offshore terrace* |
| | *020* | *offshore terrace* |
| | *110* | *Hecate Strait* |
| | *120* | *Hecate Strait* |
| | *130* | *Hecate Strait* |
| | *140* | *Hecate Strait* |
| *MCR* | *050* | *Moresby Island* |
| | *070* | *Moresby Island* |
| | *080* | *Moresby Island* |
| | *100* | *Moresby Island* |
| *FMA* | *090* | *Moresby Island* |
| *EPB* | *030* | *Moresby Island* |
| | *040* | *Moresby Island* |
| | *060* | *Moresby Island* |
| | *150* | *mainland region* |
| | *160* | *mainland region* |
| | *170* | *mainland region* |

**Table I.** Receiver number and location of seismographs used in the experiment. Instrument types are: OBS - ocean bottom seismograph, MCR - microcorder, FMA - FM analog recorder, and EPB - Earth Physics Branch "Backpack" recorder.

## 2.3 Data Processing

### 2.3.1 Initial data reduction

The initial stage in the data reduction process was to standardize the data recorded by the different seismograph systems. First, the analog data from the OBSs and FM recorder were converted to digital format on 9-track magnetic tapes using a PDP 11/34 -based digitization and editing package.

Digitization of the OBS data was a two-step process involving the transfer of field data, recorded at 0.2 mm/s, to high quality 1/4 inch FM tape at 6.0 mm/s. The

resulting 30-time speed-up was necessary to overcome digitization system limitations for the slow-speed data recordings. The 4-channel FM tapes of OBS data were then digitized at 120 sps using the 10 Hz time code signal recorded on one of the tracks as a trigger to avoid timing problems associated with tape stretch and recorder speed variations. A detailed description of the OBS digitization procedure may be found in Mackie (1985).

The FM recorder analog data tapes were digitized directly at 120 sps using an external frequency generator as a sampling trigger. Timing errors associated with tape stretch and tape speed variations were negligible. Both the OBS (explosion only) and FM analog data were later reduced to 60 sps recordings for plotting compatibility with the digitally recorded data from the other seismographs.

Data from the EPB "Backpack" systems were transfered from digital cassettes to 9-track magnetic tapes by personnel at the Earth Physics Branch. A similar transfer of UBC Microcorder data was done at UBC.

Once the entire data set was in digital format on magnetic tapes, editing of shot recordings and demultiplexing was done using the PDP 11/34 system. All explosion recordings and randomly-selected airgun shots were plotted to monitor data quality before proceeding with further processing.

### 2.3.2 Shot and receiver positioning

The position of the ship was determined from Loran C navigation with a relative accuracy of ± 200 m and an absolute accuracy of ± 300 m (Hyndman et al., 1979). The accuracies were increased by updating the Loran C system with satellite fixes when available. The hyperbolic Loran C measurements were converted to geographic

coordinates and a linear interpolation between measurements was used to determine the ship's position for each airgun shot. The location of the explosive shots was determined from the ship's position at drop time. Similarly, the OBS positions were measured at the time of deployment and assumed a vertical fall of the instrument to the ocean floor. The LBS positions were directly obtained from 1:50,000 scale topographic maps with absolute accuracies of approximately 150m.

Shot–receiver distances were computed from the geographic coordinates of the various shots and receivers. A geometric factor was applied to the airgun data to correct for the offline location of OBSW1 (receiver 010) and shift the OBS position to the shooting line. This correction ranged from 2.4 km for the closest shot to 0.2 km for the shot 15 km distant. A similar correction incorporating receiver depth as well was applied to the corresponding travel times.

A positioning error was noticed on recordings of explosive shots at OBSW1. Hydrophone component plots showed that direct water wave arrivals did not pass through the origin but instead intersected the distance axis at a point 1.78 km away. When the bathymetric profile was compared to the depth profile of the overlapping airgun survey a discrepancy of approximately 2 km was observed for major physiographic features. The result was a 1.78 km correction applied to shot–receiver distances for the OBSW1 explosion data set. The error may have resulted from an incorrect log entry during data acquisition; the above correction has hopefully restored the true positions and distances.

### 2.3.3 Depth determinations

Water depth was continuously recorded through the ship's depth sounding system on an EPC line scan recorder during the survey. The depth of each OBS was determined from these recordings at the time of deployment. The elevations of the LBSs were read from the topographic maps on which their positions were located.

Two methods were used to calculate explosion shot depths. The geometrical method, described in Horn (1982), uses the ship speed, ditch time, water depth, and the time lag between the direct and bottom reflected water waves as recorded on a trailing hydrophone to compute shot depths. This method provided a good estimate of depth for the more distant shots beneath which the seafloor was relatively flat and horizontal.

The bubble pulse method relies on the relationship between explosion depth and the period of first oscillation of an expanding explosion-generated gas bubble which is forced to collapse due to hydrostatic pressure. The Rayleigh–Willis bubble formula, based on work by Lord Rayleigh (Strutt, 1917) and Willis (1941), was used to compute depths for shots over the irregular topography of the terrace. Both methods have a maximum estimated error of $\pm$ 30 m.

The airgun maintained a relatively constant depth of 17 m throughout the survey as controlled by the length of the towing cable and the ship speed, thereby obviating the need for complicated depth calculations.

### 2.3.4 Timing calculations and corrections

The WWVB time signal received aboard ship was used as absolute time throughout the survey. Readings from other clocks and instruments were converted to WWVB time during processing to standardize time measurements.

Shot origin times for explosions were calculated from the shot depth and distance previously computed, using

$$t_0 = t_d - \frac{\sqrt{d^2 - x^2}}{V_w}$$

where $d$ =shot depth, $t_d$ =arrival time of direct water wave, $x$ =ship–to–shot distance, and $V_w$ =water velocity at 1.49 km/s (Horn, 1982).

The airgun firing time was controlled by a trigger clock for which the signal was recorded with WWVB code on both a 2–channel chart recorder and a 4–channel tape recorder. A linear clock drift correction was subsequently applied to airgun shot origin times based on these recordings.

All instruments with internal clocks (OBSs and Microcorders) were rated against either WWVB (OBSs) or WWV (Microcorders) immediately before and after use. Internal clock readings in code were recorded directly on to the tapes. Recording times could thus be related to WWVB after applying any necessary corrections for the linear drift of the internal clocks. The FM analog system recorded WWVB directly onto a parallel channel thereby avoiding timing problems. Clock drift for the EPB Backpacks is unknown as no information was provided by EPB personnel.

Corrections applied to times of first sample include the geometrical offline corrections mentioned in section 2.3.2 and shot depth corrections. The explosions and airgun shots were vertically shifted to the ocean surface using the shot depths and a water velocity of 1.49 km/s.

The maximum uncertainties due to shot origin times, clock drift, shot depths and travel time picks are summarized in table II. The time errors due to uncertain travel time picks are considerably larger than other timing uncertainties in most cases.

| *CORRECTION* | *OBS (s)* | *MCR (s)* | *FMA (s)* | *EPB (s)* |
|---|---|---|---|---|
| *Origin Time (EX)* | *0.030* | *0.030* | *0.030* | *0.030* |
| *Origin Time (AG)* | *0.010* | *0.010* | *0.010* | *0.010* |
| *Clock Drift* | *0.013* | *0.006* | *0.006* | *0 ** |
| *Shot Depth* | *0.020* | *0.020* | *0.020* | *0.020* |
| *Time Picks* | *0.01-0.05* | *0.01-0.15* | *0.01-0.15* | *0.01-0.05* |

**Table II.** Timing uncertainties due to various corrections and traveltime measurements. EX - explosives, AG - airgun; * = value assumed.

### 2.3.5 Filtering

Spectral analysis of airgun and explosion data was performed for representative signal and noise recordings. Figure 10 shows periodograms for an OBS recording of an explosion. The seismic signal of the OBS extends from 0.5 to 15.0 Hz with significant noise in the 18 to 27 Hz range. Periodograms for a Backpack recording of the same explosion (figure 11) indicate the presence of noise below 2 Hz and strong signal above 2.5 Hz. The characteristics of these periodograms are typical of all LBS recordings which show low frequency signal and a clear noise-signal separation leading to relatively good signal-to-noise ratios.

An eight-pole zero-phase Butterworth bandpass filter was applied to the explosion data to reduce the noise content. A 0.5-15.0 Hz bandpass was used for the OBSs and a 2-12 Hz bandpass filter was applied to most of the LBS data. Filtering visibly enhanced the data especially on receivers 090 and 100 where noise had obscured first arrival energy (figure 12). The filtered data sections were used to approximately locate the first arrivals; more accurate time picks were then made on the unfiltered sections.

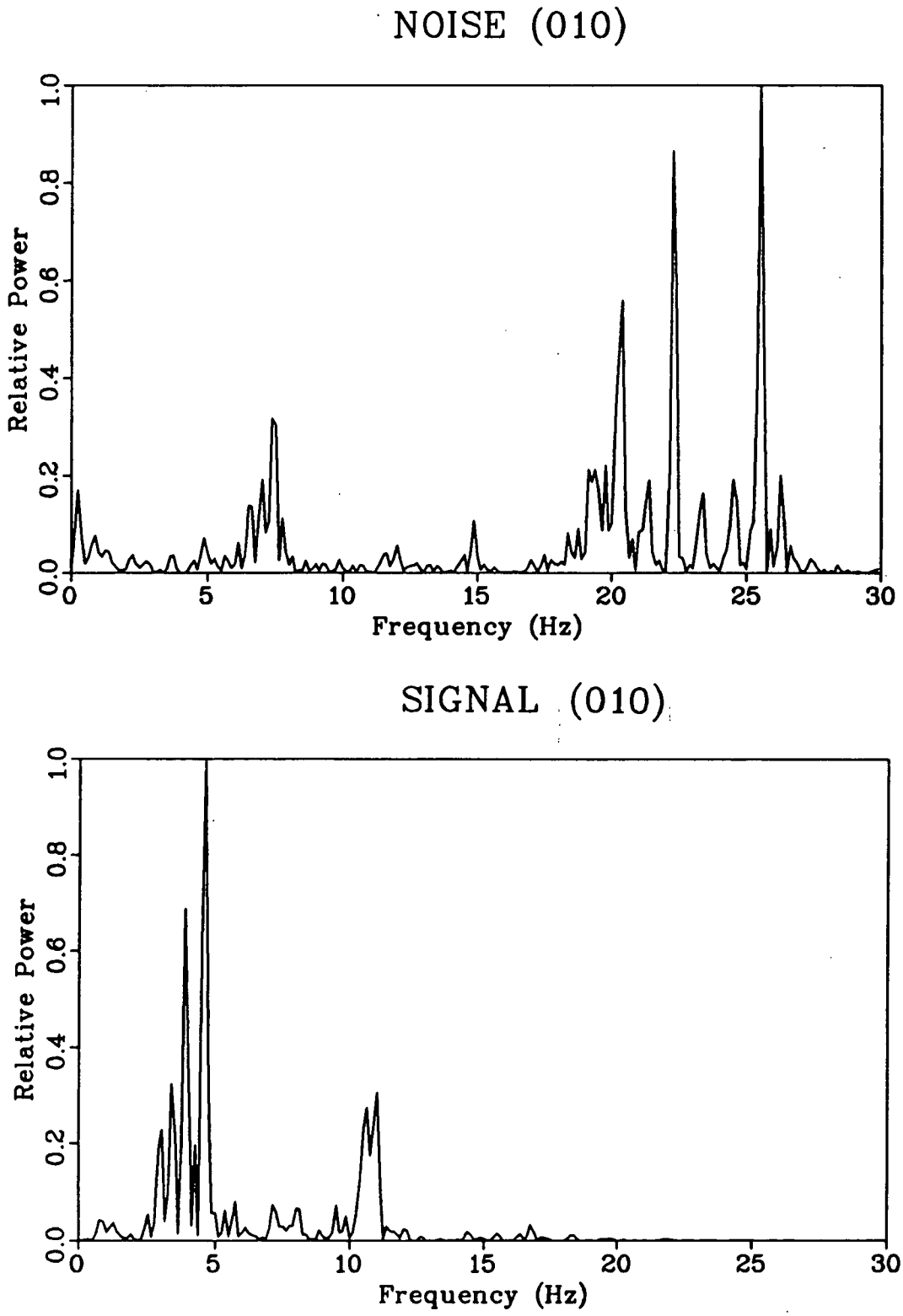


**Figure 10.** Periodograms computed for segments of noise and signal + noise recorded on the vertical geophone of receiver 010, an OBS.

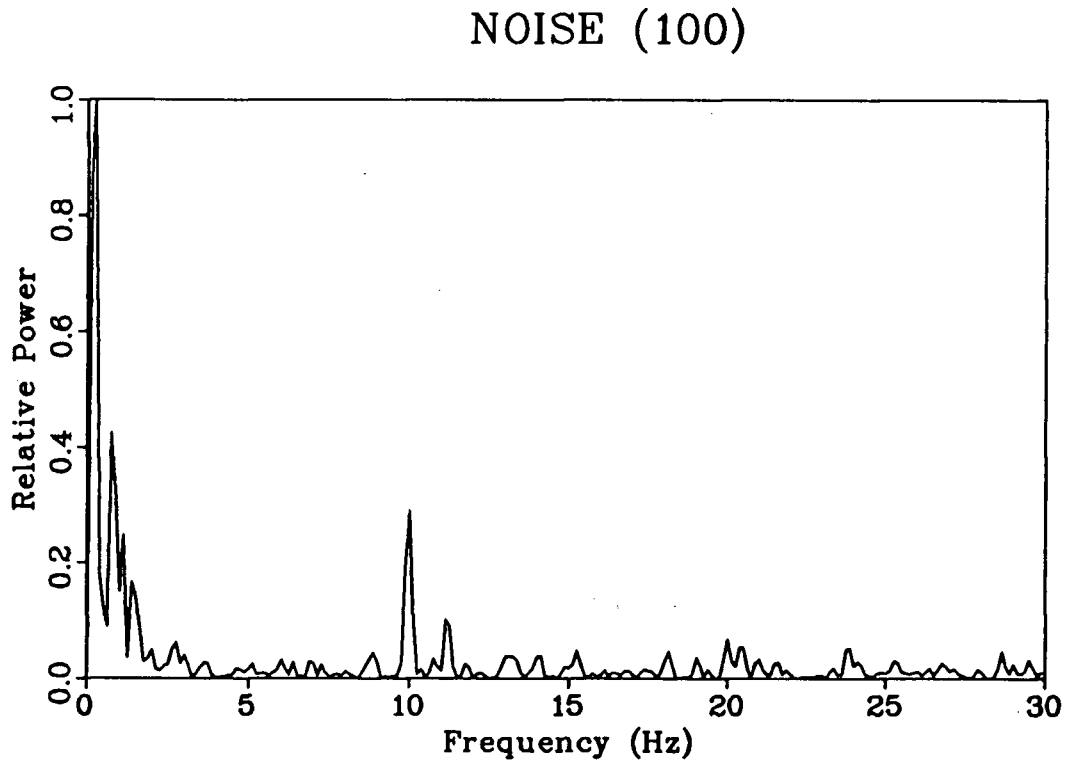


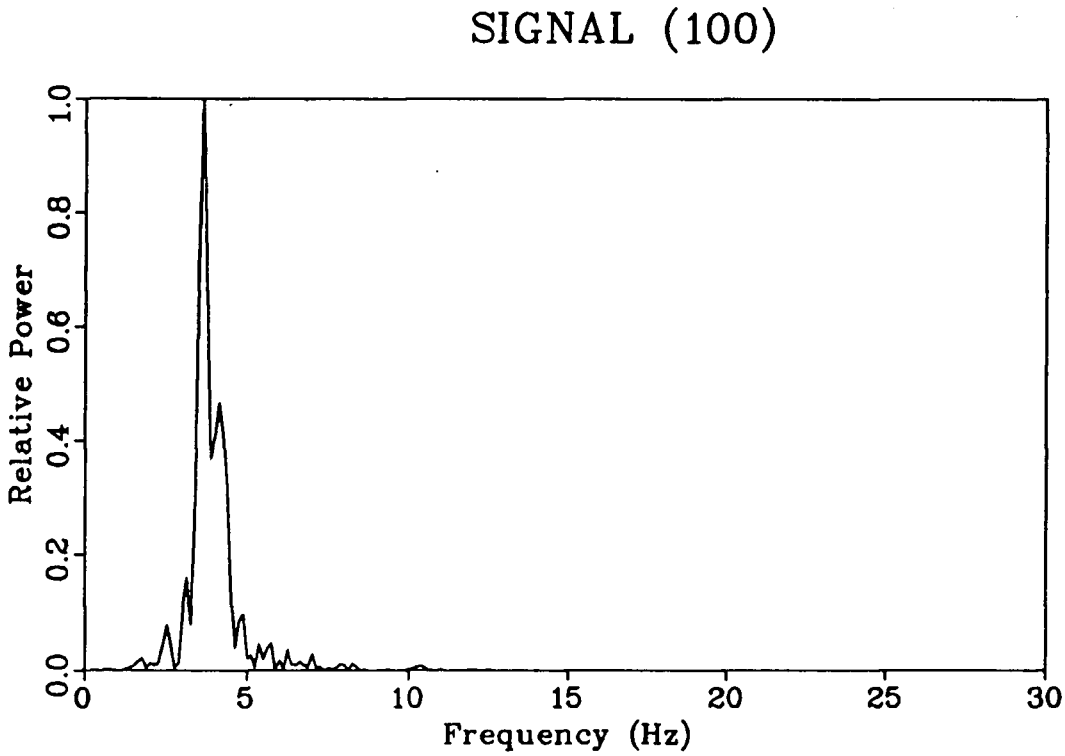


**Figure 11.** Periodograms computed for segments of noise and signal + noise recorded on receiver 100, a microcorder on Moresby Island.

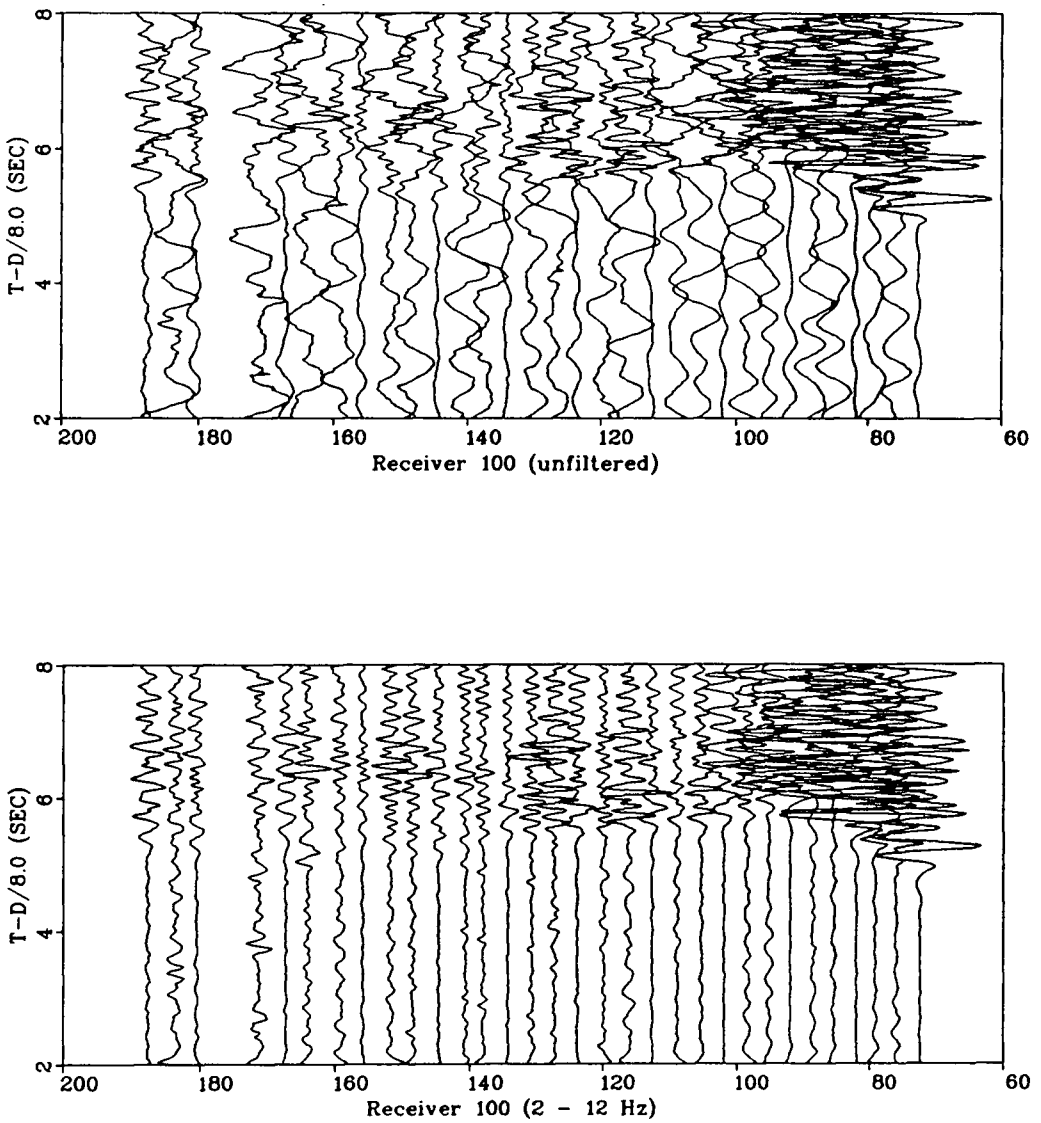


**Figure 12.** A comparison of unfiltered and filtered data sections for receiver 100 on the eastern side of Moresby Island. The horizontal axis indicates shot–receiver distance in km.

Spectral analysis of the airgun data was performed and a suitable bandpass filter was tested. No significant improvement in the signal resolution of the data was achieved, however, so the data remain unfiltered.

### 2.3.6 Amplitude corrections

Amplitude variations from trace to trace due to different charge sizes and receiver responses were expected. O'Brien (1960) determined that the amplitude of a TNT-generated wave varies as $W^{2/3}$ where $W$ is the weight of the charge in pounds. Accordingly the trace amplitudes were multiplied by $W^{-2/3}$ to account for the charge size differences. This process overcorrected large shot amplitudes for close (<30 km) shots so an additional correction was applied to make large shot amplitudes consistent with the amplitudes of adjacent small shots for near distances.

The explosion data were also corrected for spherical spreading by multiplying the trace amplitudes by $d^2$ where $d$ is the shot–receiver distance normalized to 200 km. This correction enhanced the farther arrivals with respect to the closer ones. A spreading correction of $d^1$ where $d$ is normalized to 20 km gave best results for the airgun data.

Amplitude variations due to different receiver responses were corrected by relating the velocity sensitivities for the various instruments and computing the necessary gain factors to apply to the data.

The application of the above processing methods resulted in data of generally high signal–to–noise ratio in a format ready for interpretation.

# CHAPTER III DATA ANALYSIS

## 3.1 Initial Observations and Interpretation

Common receiver gathered sections of the airgun and explosion data are shown in appendices A and B. The filters and amplitude corrections mentioned in the previous chapter have been applied as noted with each section. Further discussion of these as well as other explosion data from the experiment may be found in an open file report (Clowes, 1984).

### 3.1.1 The airgun data set

The three airgun sections shown in appendix A represent a single profile west of receiver 010 (OBSW1 WEST) and a reversed profile between receivers 010 and 020 (OBSW1 EAST and OBSW2). The data have been plotted with a reducing velocity of 4.0 km/s; hence a line parallel to the distance axis is equivalent to an apparent velocity of 4.0 km/s. The oscillatory waveforms heading diagonally away from the origin on all three sections are the direct water wave arrivals. The non-linearity of their traveltime characteristic is a result of the highly irregular topography in the region and causes them to interfere with early refraction arrivals.

At least two refraction branches can be seen on each section. An early branch which interferes with the irregular direct wave arrivals on OBSW1 WEST intersects sharply with a strong second refraction branch that continues linearly across the section to the maximum shot-receiver distance of 15 km. The transition between refraction branches is much smoother for the other two sections and the gentle curvature of OBSW2's arrivals suggests several ever steeper branches are involved. The refraction arrivals for reversed profiles OBSW2 and OBSW1 EAST undergo a severe amplitude loss just past 3 km

and 10 km model distance respectively; this corresponds to 10 km shot-receiver in both cases, suggesting a common loss mechanism. The location of arrivals after this distance is uncertain. Additionally the arrivals on OBSW1 EAST show amplitude fluctuations over their entire length suggesting structural complications.

### 3.1.2 The three–layer case

A preliminary velocity–depth interpretation of the airgun data sections was done using three–layer horizontal interface equations (Sheriff and Geldart, 1982) which have been rederived to consider a surface source and a receiver positioned at the first interface (figure 13).

Refraction along first interface:

$$
\begin{aligned}
t &= \frac{h_1}{V_1 \cos\theta_1} + \frac{x - h_1 \tan\theta_1}{V_2} \\
&= \frac{x}{V_2} + \frac{h_1}{V_1}\cos\theta_1 = \frac{x}{V_2} + t_1 \\
h_1 &= \frac{V_1 t_1}{\cos\theta_1}
\end{aligned}
$$

Refraction along second interface:

$$
\begin{aligned}
t &= \frac{h_1}{V_1 \cos\phi_1} + \frac{2h_2}{V_2 \cos\theta_2} + \frac{x - h_1 \tan\phi_1 - 2h_2 \tan\theta_2}{V_3} \\
&= \frac{x}{V_3} + \frac{h_1}{V_1}\cos\phi_1 + 2\frac{h_2}{V_2}\cos\theta_2 = \frac{x}{V_3} + t_2 \\
h_2 &= \frac{V_2}{2\cos\theta_2}\left(t_2 - \frac{h_1}{V_1}\cos\phi_1\right)
\end{aligned}
$$

where $t$ =traveltime of ray, $h_n$ =thickness of layer $n$, $V_n$ =velocity of layer $n$, $t_n$ =intercept of $n$-th refraction branch at zero offset, $x$ =horizontal component of shot–receiver distance, and $\theta_n$ =critical angle for layer $n$.

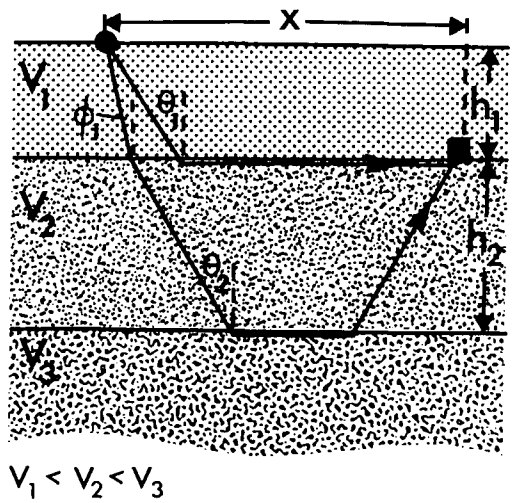


**Figure 13.** Ray paths for critically refracted waves in a three–layered medium travelling from a surface source to a receiver at the first interface.

The equations assume horizontal interfaces; this assumption is invalid for interface 1 (water—sediment) because of the known irregular topography. However, the depth estimates will provide at least a general structure which can later be refined through additional interpretation.

Layer thicknesses were computed for all three data sections by measuring the velocities and times on the sections and using $V_1$ = 1.49 km/s as water velocity. The results

| PROFILE | $V_1$ | $h_1$ | $V_2$ | $h_2$ | $V_3$ |
|---|---|---|---|---|---|
| OBSW1 WEST | 1.49 | 2.24 | 2.29 | 1.73 | 4.48 |
| OBSW1 EAST | 1.49 | 1.14 | 1.64 | 1.20 | 4.00 |
| OBSW2 | 1.49 | 0.44 | 2.05 | 1.01 | 3.34 |

**Table III.** Velocity and layer thickness estimates from three-layer interpretation of airgun data.

are summarized in table III. These values will form the preliminary model for further interpretation.

### 3.1.3 The explosion data set

The gathered sections for receivers 010 to 100 found in appendix B have been plotted with an 8.0 km/s reducing velocity. It should be noted that the high amplitudes resulting from large shots at near offsets and close shots in general have been over-compensated for in the correction routines and hence their relative amplitudes are misrepresented in these sections.

All sections show distinct primary arrivals; some also have lower velocity higher amplitude secondary arrivals. Receiver 010 recorded both sets of arrivals across the entire section. Noise obscures arrivals at receiver 020 beyond 100 km shot-receiver distance; both refraction branches are present to that point. Receivers 030 to 100 recorded low amplitude first arrivals for shot-receiver distances greater than about 85 km and much higher amplitude first and/or second arrivals for distances less than 85 km.

### 3.1.4 First break analysis

Figure 14 is a plot of first arrivals for shots 1 to 16 recorded by receivers 010 to 100. First arrival times were determined from unfiltered data sections used in conjunction with the filtered sections which more clearly showed overall phase coherency. Shot positions are fixed for all arrivals and receivers are located at various distances to the right (east) of the plot. Plotting the arrival times above fixed shot positions provides a "common factor" for easy comparison of traveltime curves. Traveltime differences resulting solely from increased receiver offset will delay first arrival times but will not alter the shape of the curve. Structural variations encountered by rays travelling to different receivers will however be reflected as changes in the shape of the curves.

Several trends between curves immediately become apparent. There is an average time delay of 0.6 s between arrivals from shots 4 and 5 at all receivers. This indicates a major lateral change in subsurface structure beneath these points which are located above the outer edge of the terrace. The first arrival curves are all approximately parallel with the exception of receiver 010 (OBSW1) which has a much lower apparent velocity. Energy travelling east of OBSW1 towards the other receivers appears to be passing through material of different composition. The remaining arrival curves successively increase in time with increasing receiver distance except for arrivals at receiver 020 (OBSW2) which are delayed by a minimum of 0.2 s. This delay suggests the existence of lower velocity material beneath OBSW2 than beneath the Queen Charlotte Island receivers.

The general information provided by these curves will be combined with available constraints to construct the preliminary velocity structural model for interpretation.

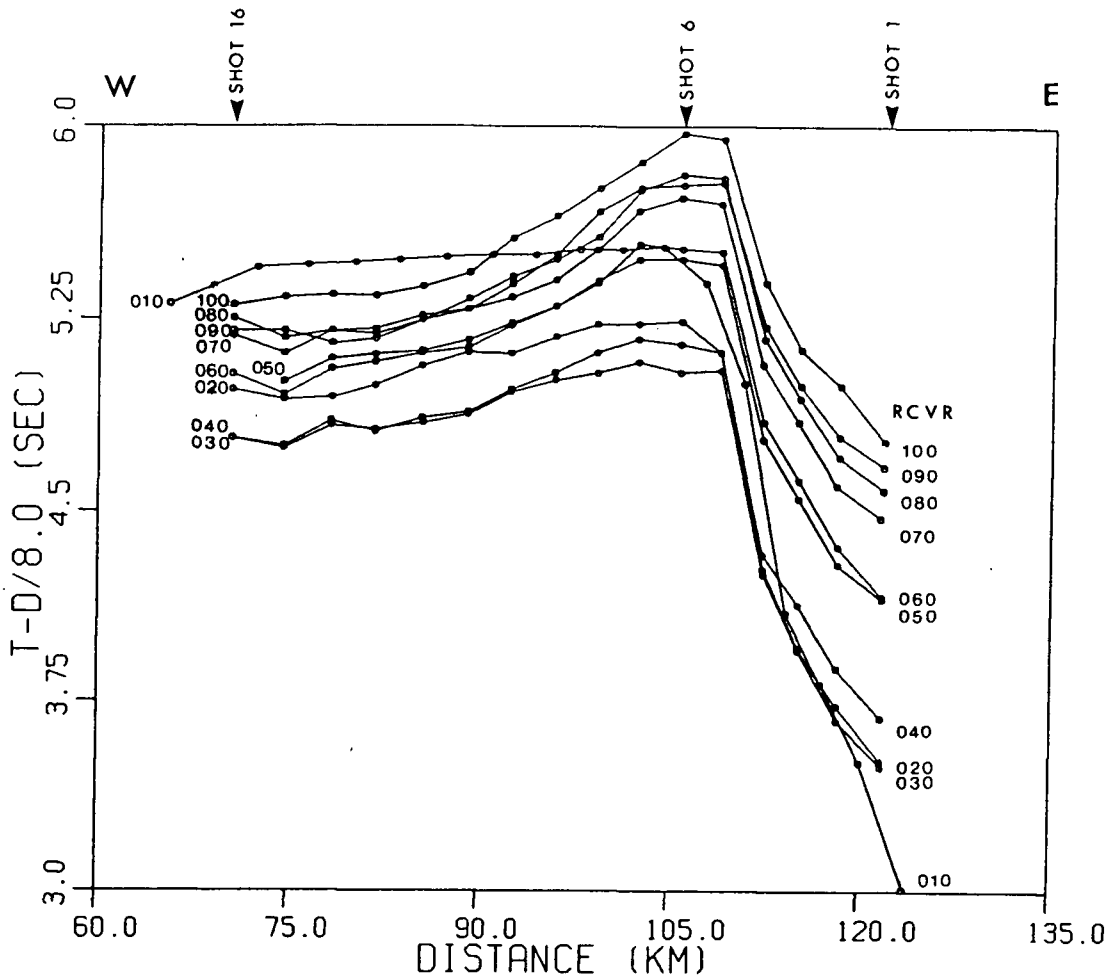


**Figure 14.** First arrivals for shots 1–16 at receivers 020 to 100 and shots 1–18 at receiver 010. Shot locations are fixed to their positions in the final model and receivers are located to the right (east) of the plot. Distance corrections have offset the shots for receiver 010 by 1.78 km. (See text for interpretation method.)

### 3.2 The Modelling Method of Interpretation

The general method of interpretation used in this study involves the comparison of vertical component observed data with theoretical seismograms. A ray tracing algorithm

is applied to a representative velocity model and synthetic seismograms are computed from the resulting traveltimes and amplitudes. The solutions determined by this forward modelling technique are non-unique so in this study every attempt was made to generate the most geologically reasonable model within the available constraints.

### 3.2.1 The modelling algorithm

An algorithm based on asymptotic ray theory (Spence, 1984; Spence et al., 1984) was used to calculate the synthetic seismograms. The ray tracing routine is an extension of the Whittall and Clowes (1979) algorithm which calculates traveltimes for refracted and postcritically reflected rays and "pseudo" head waves traced through a two-dimensional velocity model. The extension enables tracing of precritically and multiply reflected rays through the model. Amplitudes are calculated by asymptotic ray theory approaches and synthetic seismograms are generated after superimposing the displacements of all arrivals at a particular distance.

### 3.2.2 Modelling techniques

Models to be used with the ray tracing routine are constructed of polygonal blocks, each with its own velocity and linear velocity gradient. The velocity is defined on the uppermost boundary of each block and is constant along the line segment. The gradient is then oriented normal to this boundary.

Rays are traced through the model and the computed traveltimes are compared to observed times. The model is changed by repositioning boundaries and blocks or varying the defined velocity and gradient. The procedure is repeated until a suitable traveltime fit is attained. The calculated amplitudes must also agree with the observed data; a

model that fits the traveltimes may not provide a good amplitude match. The forward modelling procedure must thus be continued until satisfactory agreement with both the traveltimes and amplitudes is obtained and the model meets the initial constraints.

# CHAPTER IV INTERPRETATION OF AIRGUN DATA

## 4.1 Initial Constraints

The airgun line AG2 was shot over the two OBSs to provide information on the sediment and upper crustal structure of the terrace west of the Queen Charlotte Islands. Several continuous seismic reflection profiles (CSPs) in the region (Chase and Tiffin, 1972; Chase et al., 1975; Davis and Seemann, 1981) indicate that the terrace subsurface is composed of faulted and tightly folded sediments partially infilled with stratified sediments showing increasing deformation with depth. Analyses of terrace sediment velocities south of the present study area (Kirstiuk, 1981; Tjaden, 1981) indicate extreme lateral inhomogeneity in the shallow subsurface above 4 km depth. A structural model developed for a seismic refraction profile west of southern Moresby Island (Horn, 1982; Horn et al., 1984) provides structural and velocity information for the deeper structure of the terrace region.

The velocities and layer thicknesses estimated from the data sections (table III) and constrained by these other studies were combined with the bathymetry profiles to form initial models for use with the ray tracing routine. Continuity between receivers was provided by the Horn et al. (1982) model. The final composite velocity model was derived from analysis of data recorded at OBSW1 for shots west of the OBS location (segment I) and from reversed data recorded at OBSs W1 and W2 for shots between the two OBSs (segment II). The model is presented in figure 15 for reference during the following modelling discussions of the individual profiles.

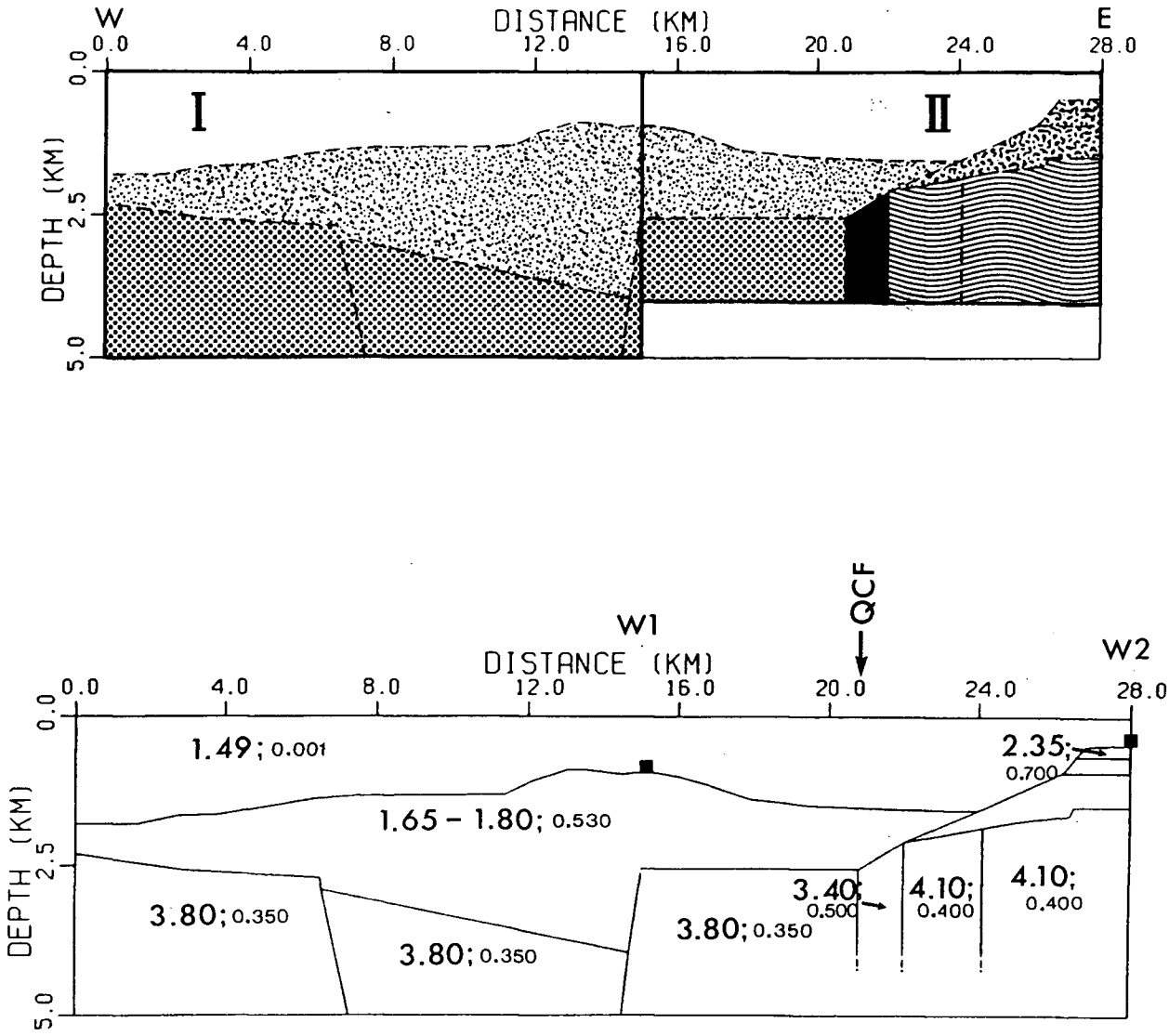


**Figure 15.** Final velocity model from ray tracing of airgun data. Velocities are in km/s, velocity gradients are in km/s/km. The upper model shows the division into individual profile models. Section I was modelled as OBSW1 WEST and section II was modelled as OBSW2 and OBSW1 EAST.

## 4.2 Profile OBSW2

Sections OBSW1 EAST and OBSW2 provide a reversed profile between OBSW1 on a mid-terrace topographic high and OBSW2 at the edge of the narrow continental shelf. The major amplitude decrease on both sections severely limits the extent of the region sampled by both data sets; good control of depth and dip in the central portion of the model is however still expected.

Figure 16 shows rays traced through the final OBSW2 model and compares the resulting traveltimes with picks from the data. The model shows a two-layer structure with low velocity sediment above a higher velocity unit. Lateral velocity variations in both layers are seen across the proposed Queen Charlotte Fault (QCF) location.

First arrival time picks indicate that the sediment beneath the continental shelf is of fairly high velocity (2.35 km/s). No clear reflections from the top of the underlying structural unit were observed on the data section, suggesting a partial loss of energy transmitted through the sediments. Several flat-lying units of increasingly higher velocity were thus used to model the sediment layer, although it should be recognized that the energy loss may be from passage through deformed and faulted sediments instead of through several reflecting interfaces. The arrivals between 27 and 23 km in figure 16b are the modelled refractions through the shelf sediments with some later reflected arrivals from the underlying unit.

A lower velocity (1.65–1.80 km/s) was required by traveltimes for the deformed sediments of the terrace itself. The complex structure observed on the CSPs was not compensated for in the model. High velocity gradients are required for the sediments in both regions.

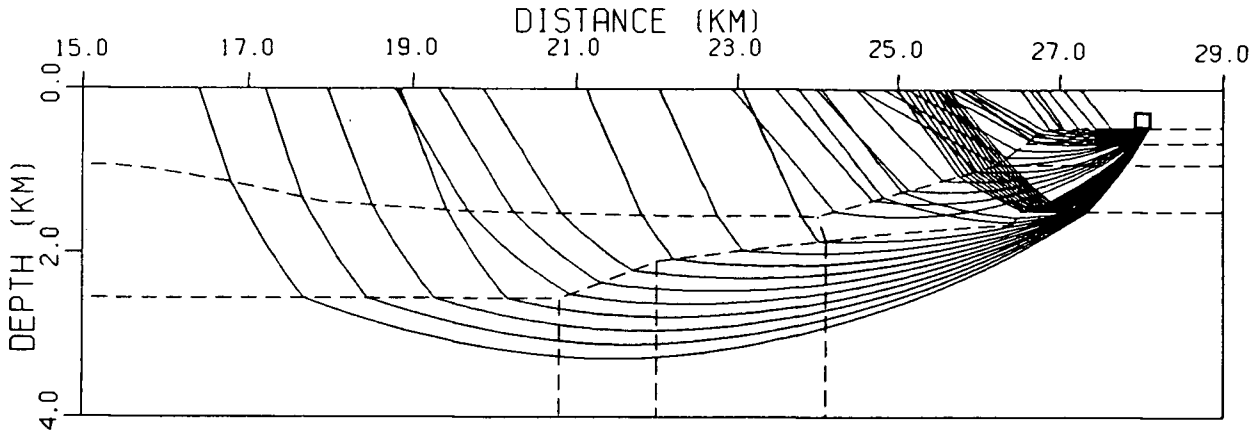


(a)

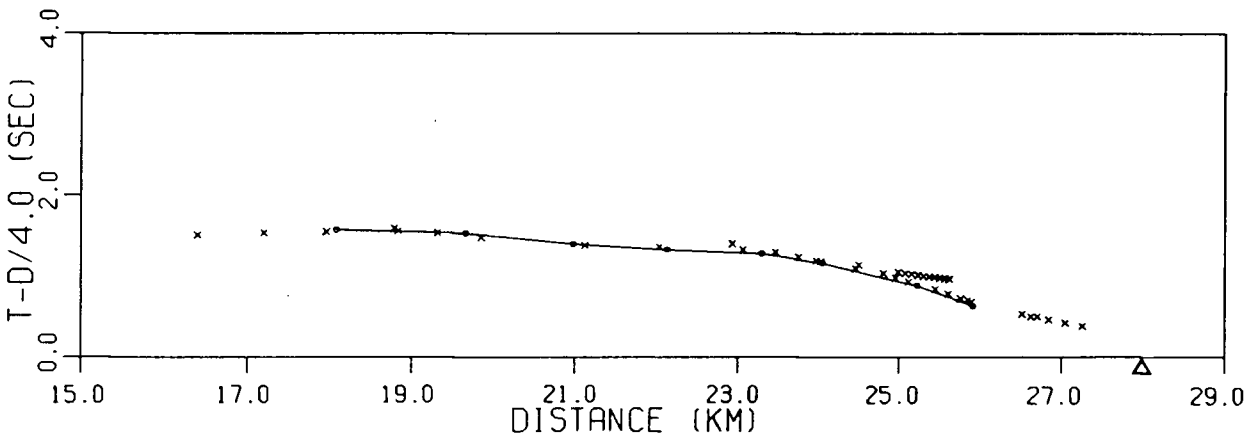


(b)

**Figure 16.** Ray tracing model (a) and traveltimes (b) for profile OBSW2. Computed traveltimes are marked as x's, observed traveltimes are connected points. The distance scale and velocity structure correspond to those given for segment II in figure 15. OBSW2 is at 28 km as indicated.

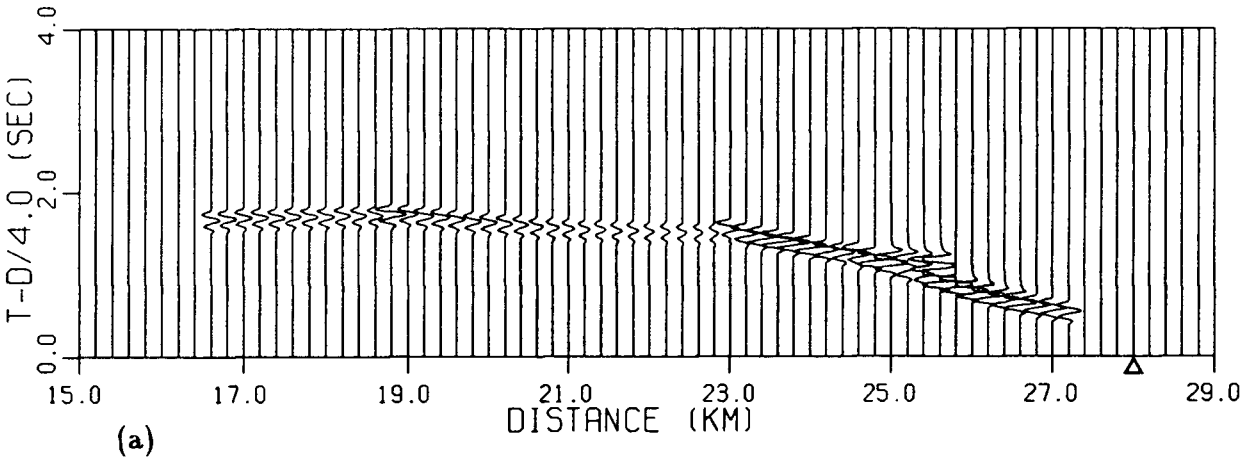


(a)

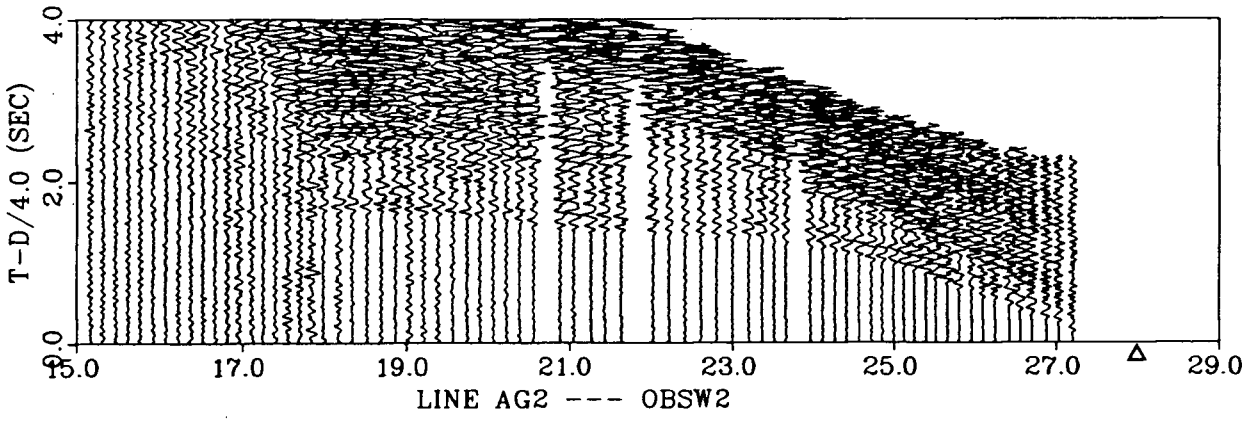


(b)

**Figure 17.** Seismograms for profile OBSW2. (a) synthetic seismograms corresponding to figure 16. (b) vertical component observed data. The source wavelet used for all airgun synthetic seismograms is from data section OBSW1 WEST. Distance scales are model distances.

Arrivals from 23 to 16 km were modelled as refractions through the lower structural unit, which is composed of several blocks with high-angle boundaries modelled as vertical faults. A good fit to the undulating observed first arrival curve (figure 16b) was achieved by varying the velocity and depth of each individual block. The faulted unit beneath the continental shelf has a velocity of 4.1 km/s and a fairly high gradient of 0.40 km/s/km. This unit is separated from the main QCF by a narrow block of much lower velocity (3.4 km/s) and higher gradient. West of the QCF lies a slightly deeper unit of 3.8 km/s velocity and moderate gradient.

Figure 17 compares the synthetic seismograms with the processed data section. The computed amplitudes for refractions between 27 and 23 km are much higher than the observed ones. This is presumably because of interference between these refractions and direct waves which have not been modelled, and attenuation due to near-surface sediments which cannot be modelled with the program used. Modelled refractions through the deeper unit are seen as a smooth line of increasingly higher amplitude arrivals to approximately 17 km model distance. The reason for the sudden loss of amplitude for corresponding first arrivals at about 18 km model distance on the data section is uncertain. The amplitude loss was successfully reproduced with a model that incorporated a low velocity zone (LVZ) east of the QCF below 3 km depth. Rays travelling upwards through the LVZ were reflected back at its upper boundary. However, the thickness of the LVZ could not be determined from the available data. This factor would have introduced a large degree of traveltime uncertainty into the explosion model for OBSW2 and created a local anomaly within the regional structure so the LVZ model was rejected. The QCF itself remains the most probable cause of the amplitude loss.

### 4.3 Profile OBSW1 EAST

The ray tracing model and traveltimes for arrivals at OBSW1 are shown in figure 18. The model shown is the same as previously discussed for OBSW2. The reversed receiver position provides additional constraints for the western and central subsurface structure.

Arrivals to 20 km model distance have been modelled as refractions through the upper sediment layer. A single unit of velocity 1.65 - 1.80 km/s and high gradient (0.53 km/s/km) was used to represent the sediment layer. The sediment deformation seen on CSP sections could not be duplicated at the scale of the model but is expected to reduce amplitudes of refractions through the sediments and reflections from the underlying unit. This may explain why the triplication branch (a to b in figure 18b) from modelled reflections is not observed on the data section. Refractions through the lower structural unit generate the remaining first arrivals east of 20 km distance.

The OBSW1 EAST data section and corresponding synthetic seismograms are shown in figure 19. Amplitudes for rays refracted through the upper sediment to 19 km distance are higher than those observed on the data as expected. Arrivals for rays refracted through the lower unit show uniformly low amplitudes on the synthetic seismogram plot. The corresponding arrivals on the data section have moderately high amplitudes to 22.3 km distance followed by a sudden decrease to the modelled amplitude level. The arrivals continue with low amplitude to 24.5 km where they appear to stop. Very weak arrivals between 25 and 27 km (figure 20) may be the attenuated continuation of these low amplitude refractions.

A band of high amplitude arrivals with concave upward characteristics is seen on the data section between 22.5 and 25.5 km (figures 19b and 20). Their nature suggests

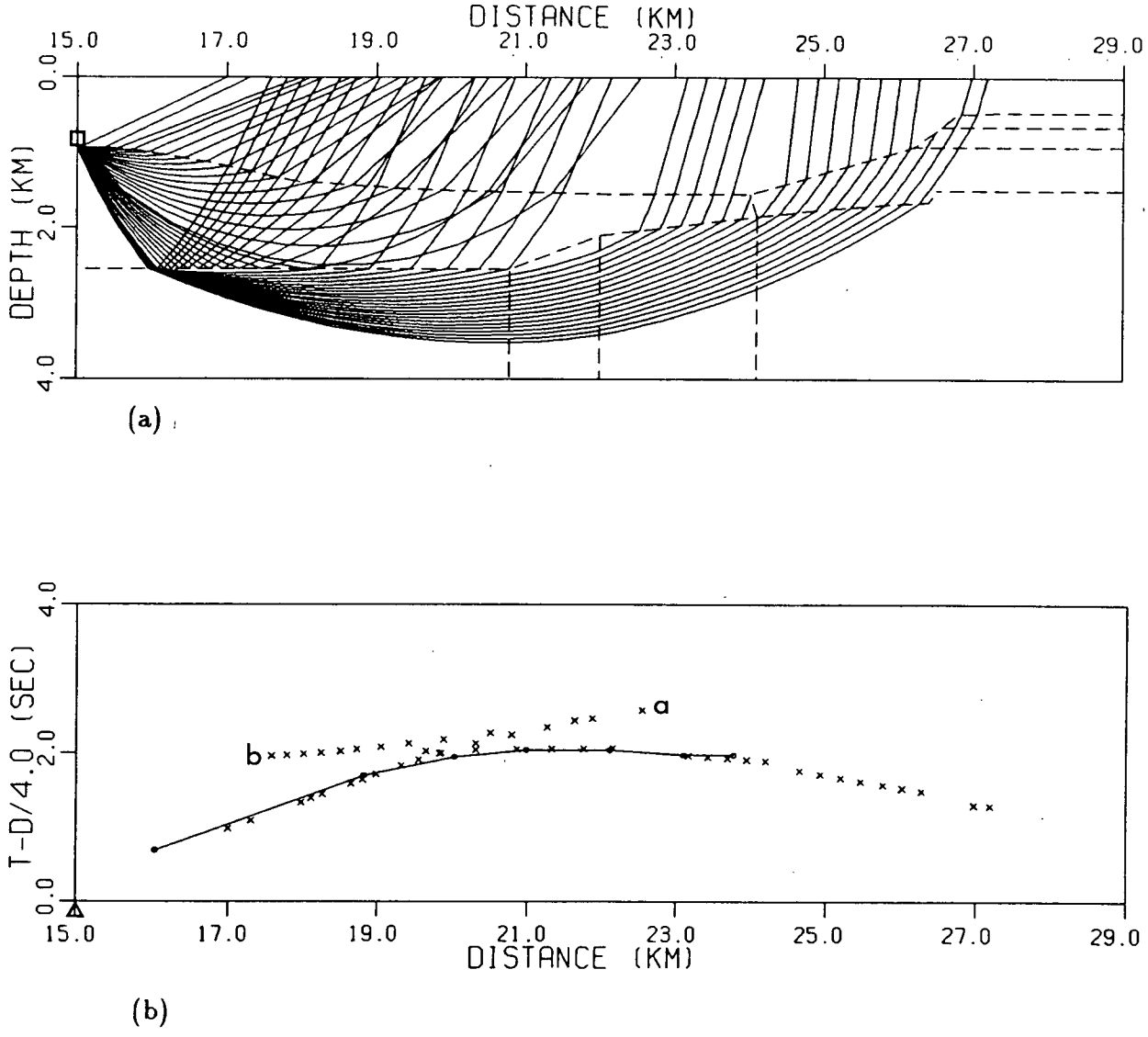


**Figure 18.** Ray tracing model (a) and traveltimes (b) for profile OBSW1 EAST. OBSW1 is at 15 km model distance as shown.

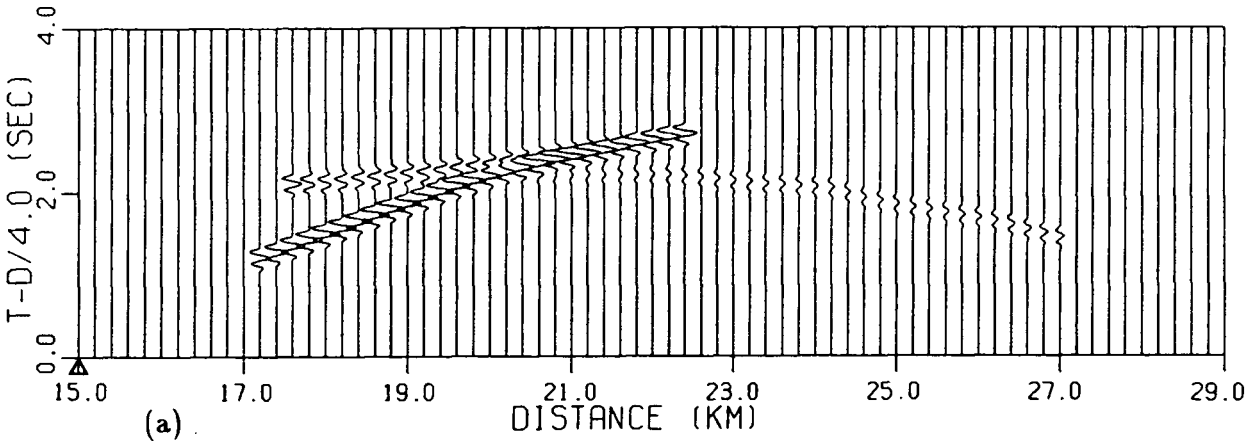


(a)

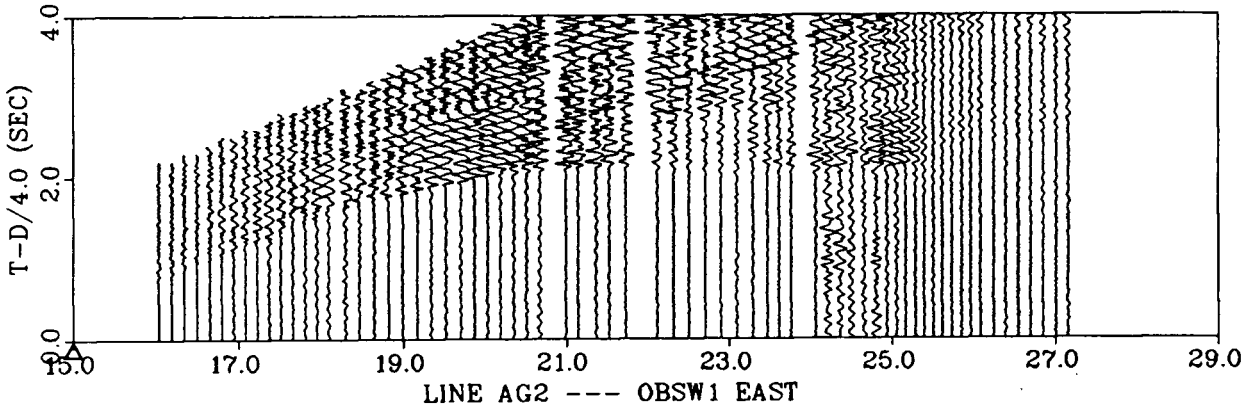


(b)

**Figure 19.** Seismograms for profile OBSW1 EAST. (a) synthetic seismograms corresponding to figure 18. (b) observed data. The receiver is located at 15 km.

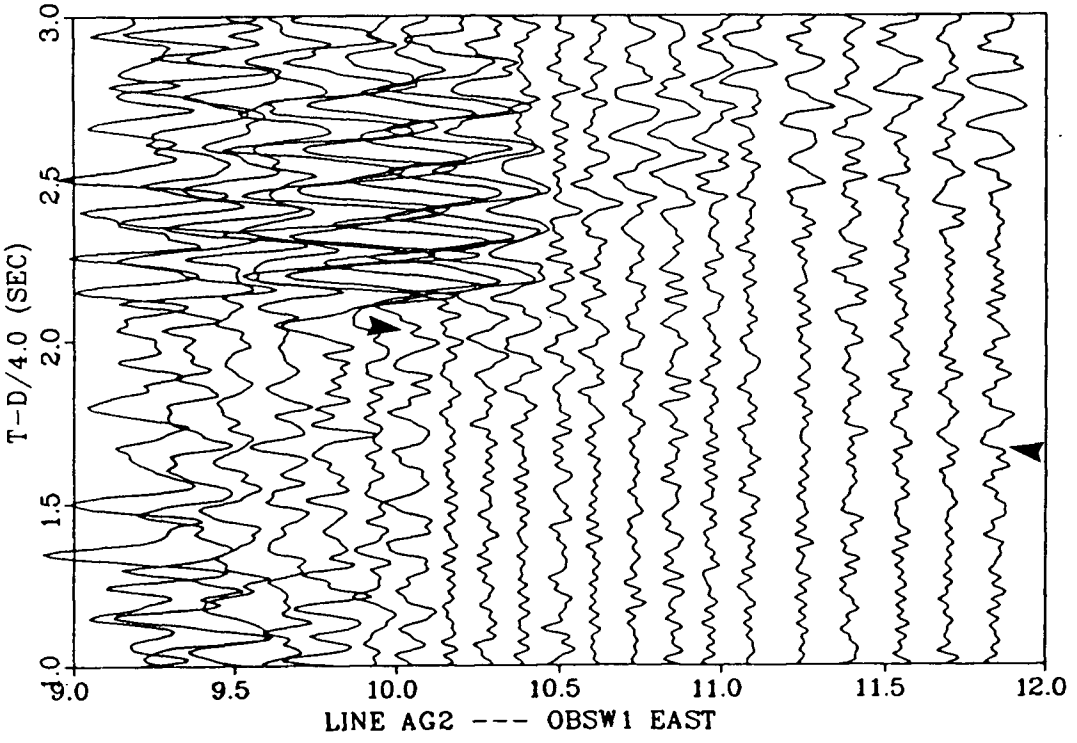


**Figure 20.** Detail from figure 19 showing low amplitude arrivals.

that they may be reflections but a suitable reflector position could not be modelled. Similarly, the inclusion of multiply-reflected rays in the model did not provide the necessary traveltime match. The arrivals have tentatively been attributed to a local focussing of rays.

## 4.4 Profile OBSW1 WEST

Profile OBSW1 WEST is a westward continuation of the previously modelled data recorded at OBSW1. The profile is unreversed, affording no dip control, but lateral continuity of segment II model features (figure 15) across the receiver location will provide velocity constraints.

A two-layer structure has again been used to reproduce the data traveltimes (figure 21). The upper layer is a continuation of the sediment unit from the OBSW1 EAST model and as before does not compensate for sediment deformation. The lower layer has the same velocity as the adjacent unit in the OBSW1 EAST model but is located an average 1 km deeper to satisfy the traveltimes. A slight eastward dip is required for this unit; a horizontal interface and higher velocity would also have reproduced the traveltimes but would have required a lateral velocity discontinuity between sections.

Ray tracing has duplicated the observed traveltimes well (figure 21b). Refractions through the upper sediment layer generated first arrivals from 12 to 8 km model distance. A narrow triplication branch from the modelled interface reflections (a to b in figure 21b) was not observed on the data section; the discrepancy results from the difficulty in representing deformed sediments in the model. The interface may also be of a more gradational nature than the sharp boundary in the model; the data did not enable such fine stratigraphic detail to be determined. A small vertical offset and change in dip of the lower unit reproduce the slight bend at 4.5 km in the smooth first arrival time curve.

The synthetic and observed seismograms for this section are shown in figure 22. Upper layer refractions again show larger amplitudes on the synthetic data than on the observed set for the same reasons mentioned earlier. As just discussed, the synthetic

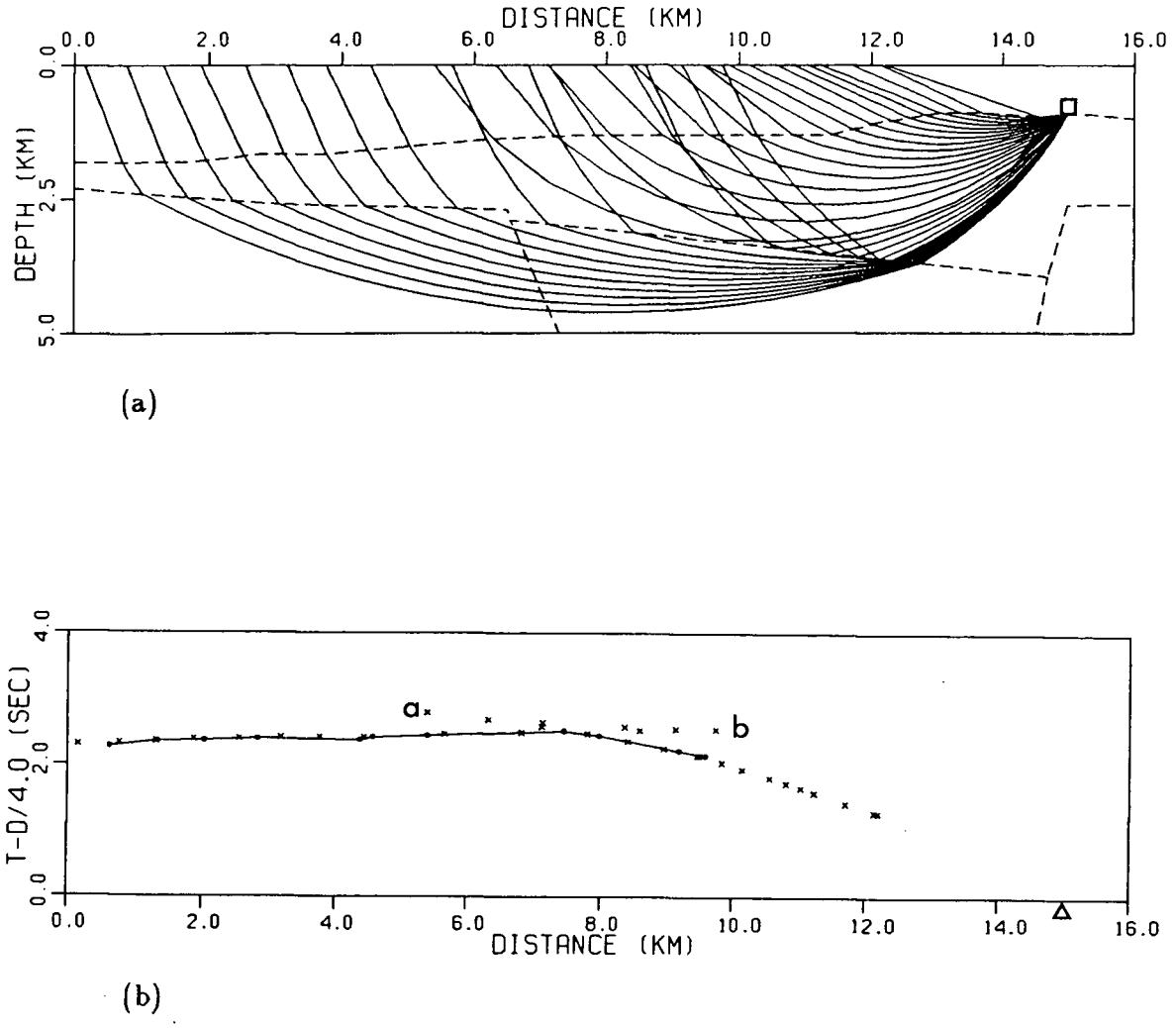


**Figure 21.** Ray tracing model (a) and traveltimes (b) for profile OBSW1 WEST. OBSW1 is at 15 km model distance. The section between 15 and 16 km overlaps the previous model (figure 18). The velocity structure and distances correspond to section I in figure 15.

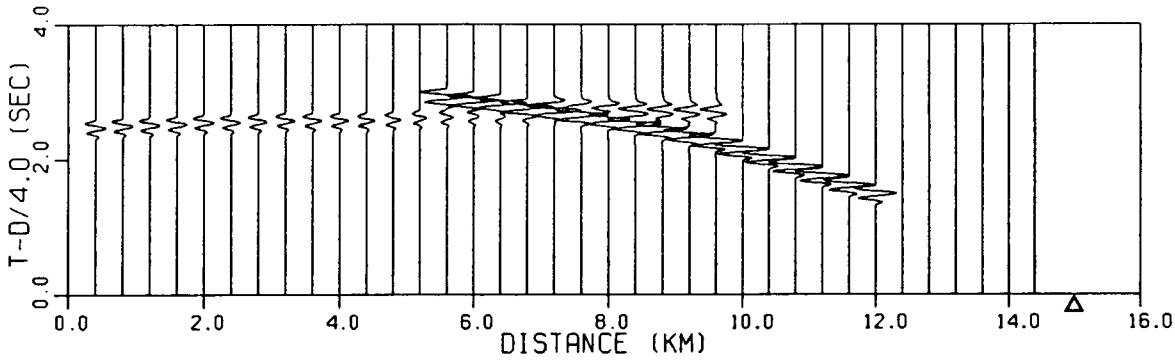


(a)

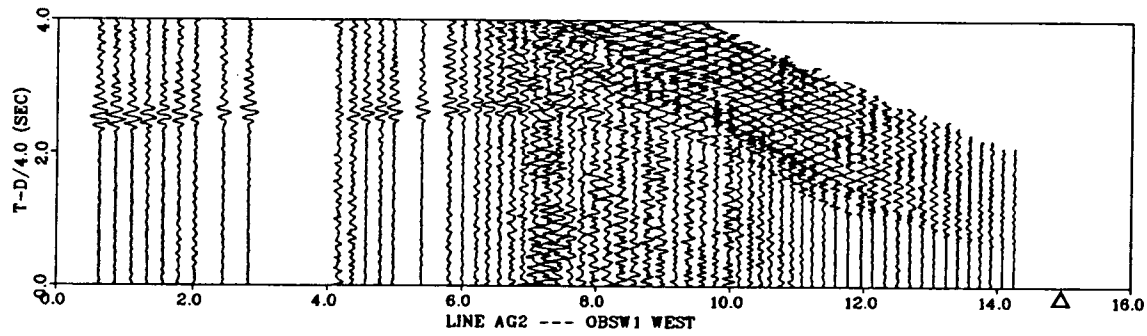


(b)

**Figure 22.** Seismograms for profile OBSW1 WEST. (a) synthetic seismograms corresponding to figure 21. (b) observed data. The receiver is at 15 km distance as indicated.

reflection branch is not seen on the data section but could not be avoided in the model. Refractions through the deeper layer are seen as a smooth set of increasingly higher amplitude arrivals extending to the end of the synthetic section and match the observed amplitudes well.

### 4.5 The Final Model

The composite model combining the results for the entire airgun data set was shown in figure 15. The two–layer structure was interpreted as a variable sediment layer overlying a complex lower unit. Sediment thicknesses range from 0.4 to 1.6 km and velocity increases rapidly with depth. The lower unit shows a graben- and horst–like feature and has different velocity structure on either side of the Queen Charlotte Fault. Amplitude loss on profiles OBSW2 and OBSW1 EAST suggest that an unmodelled, highly attenuative feature may exist in the inner terrace region. An attenuation zone located at depths greater than 3 km along the vertical fault would satisfy the requirements. Such a zone might be due to extensive shearing and deformation along the fault plane and could permit passage of energy from lower frequency explosive sources while attenuating the higher frequency airgun energy. Modelling of the explosion data set should provide a look at the deeper structure and inhomogeneities of the terrace region.

# CHAPTER V INTERPRETATION OF EXPLOSION DATA

## 5.1 Initial Constraints

The explosive shots were detonated along a 110 km profile extending into the Pacific Ocean from the western edge of the terrace. Energy generated by the 33 shots was recorded by the colinear array of seismographs after it passed through the ocean crust, terrace, and continental material beneath the Queen Charlotte Islands.

Initial constraints for a velocity model of the sampled region were obtained from numerous sources. Several CSPs (Chase and Tiffin, 1972; Chase et al., 1975; Davis and Seemann, 1981) and a nearby high density reflection seismic profile (P.D. Snavely, unpublished data) provided estimates of ocean sediment thickness and seismic basement dip. Velocities of ocean sediment and upper crust were approximated from previous studies to the north (Snavely et al., 1981) and south (Clowes and Knize, 1979) of the present study area. The model developed for the airgun data (Chapter IV) defined the shallow structure of the terrace region. Constraints for the deeper structure were based on the Horn et al. (1984) refraction model. A study by Mackie (1985) provided initial estimates of depth to the Mohorovičić discontinuity beneath the survey region.

A somewhat iterative procedure was used to develop the final model. An initial model was constructed and modified through forward modelling to fit the first common receiver data section (receiver 010). This model was then expanded and altered to fit the second data section (receiver 020) and then further modified to provide a good fit for both data sections. Modelling continued in this manner with each subsequent model having to satisfy previous data sections within reasonable limits until the final model satisfied all sections. Model reversal was then achieved by tracing rays from various shots to all receivers through the previously modelled regions and comparing

the traveltimes and amplitudes with common shot record sections that show the data recorded by all receivers for each particular shot.

The development of a single model degraded the computed traveltime and amplitude fits for each individual data section; however, the final model satisfies the total data set so its features are considered more representative of the entire region than those of the individual models.

Five common receiver gathered sections were used to develop the final model: the two OBS data sections, and three of the generally similar LBS sections recorded on Moresby Island (see appendix B). Two common shot gathered sections for large explosions were also used. The final velocity model is shown in figure 23 for reference during the following discussions of individual record section modelling. The main components of the model are: (a) an oceanic segment from 0 to 114 km; (b) the terrace region from 114 to 135.8 km; and (c) the Queen Charlotte Islands from 135.8 to 200 km distance.

### 5.2 Receiver 010

The first data modelled were the arrivals at receiver 010 (OBSW1) on the terrace. The initial model was constructed as a 130 km long segment extending from the ocean to receiver 010 and incorporated the model for airgun profile OBSW1 WEST between 115 and 130 km distance. West of the terrace a uniform oceanic structure was inserted based on the velocities and depths of Horn et al. (1984). This structure was extended beneath the terrace region to the end of the model.

Several problems with this initial model became apparent when ray tracing commenced. A much lower velocity was required for the lower terrace and an eastward dip on the adjacent oceanic segment was necessary to sufficiently delay the computed

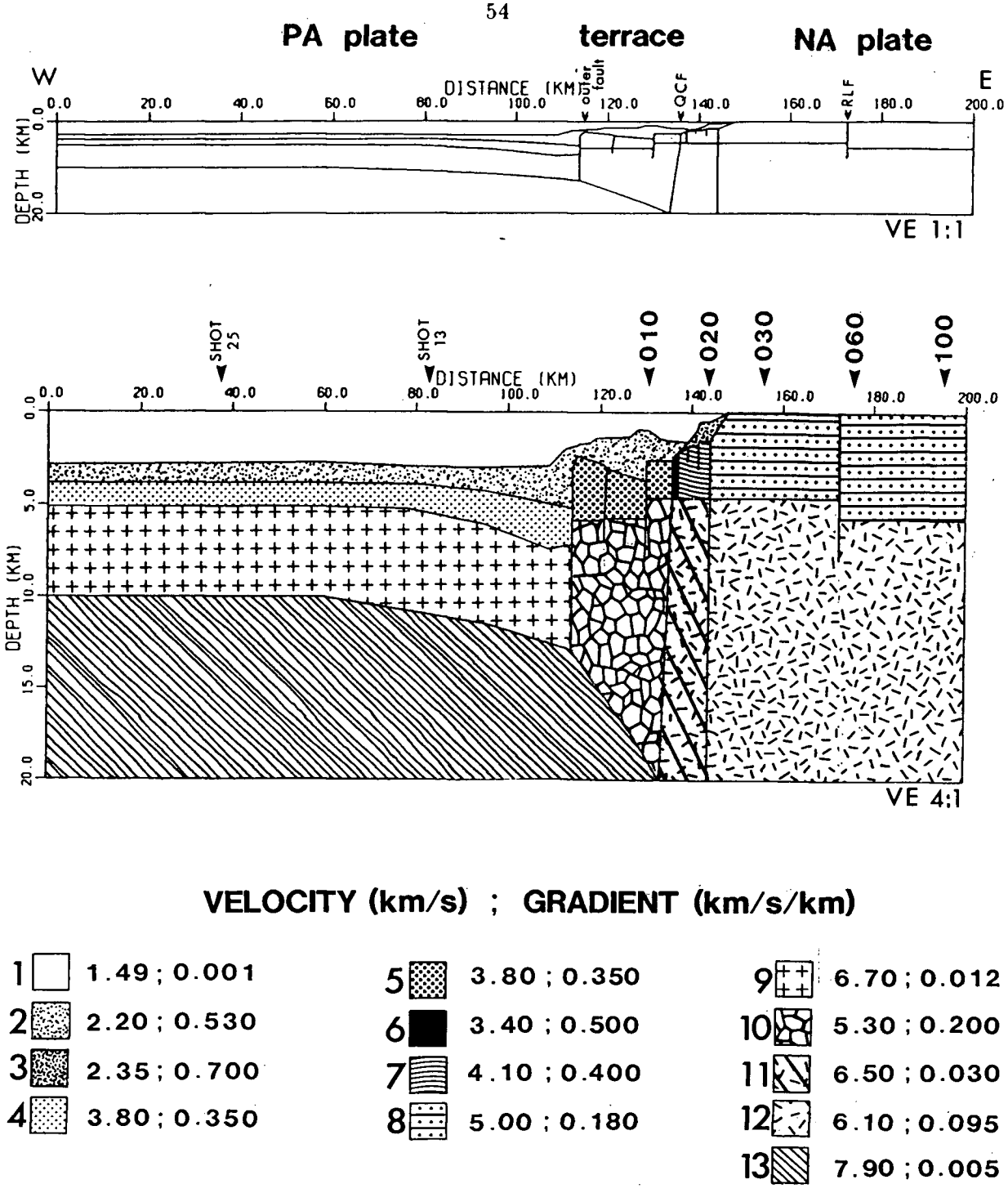


**Figure 23.** The final velocity model derived from airgun and explosion data modelling. The positions of shots and receivers used for modelling are shown. The upper 5 km between 115 and 143 km correspond to figure 15. The upper figure shows the model with no vertical exaggeration.

traveltimes to match the observed values. These and other parameters were varied until satisfactory traveltime and amplitude fits were attained and ultimately a final model was produced.

Figure 24 shows the final ray tracing model for receiver 010 and compares the computed traveltimes with the observed times. The earliest arrivals at near offsets are refractions and reflections from the sediment and upper crust of the terrace. The calculated traveltimes for these rays are slightly slower than the observed times. However, the structure was well defined by airgun modelling so alterations were not made to the model to improve the traveltime fit. The boundary between the upper and lower crustal units was positioned so as to limit the lateral extent of upper crustal refractions to the region observed on the data. The oceanic boundary (unit 4 in figure 23) is vertically downdropped 2 to 3 km with respect to the upper terrace (unit 5) to match the observed time delay of 1 s at 110 km. Traveltimes for refractions through the oceanic crust require a thickening and eastward dip of the upper crust and overlying sediment between 80 and 113 km. This approximately corresponds to the location of the Queen Charlotte Trough observed on bathymetry (figures 24a and 17). A low gradient (0.012 km/s/km) is required for the lower oceanic crust (unit 9 in figure 23) to permit refractions to travel across the entire region; the velocity was adjusted accordingly to provide the best traveltime fit. The refractions appear as secondary arrivals (a to b in figure 24b) of apparent velocity 6.8 km/s across most of the section.

Reflections from the Moho (arrivals c to d) constrained its depth between 70 and 113 km distance. A dip of 2.3° to 4.5° is required in this region. No depth or dip information is available west of 60 km so the Moho and shallower interfaces were extended horizontally to the end of the model. The effect of adding a component of eastward dip to these units, especially the Moho, would be an increase in the apparent velocity of

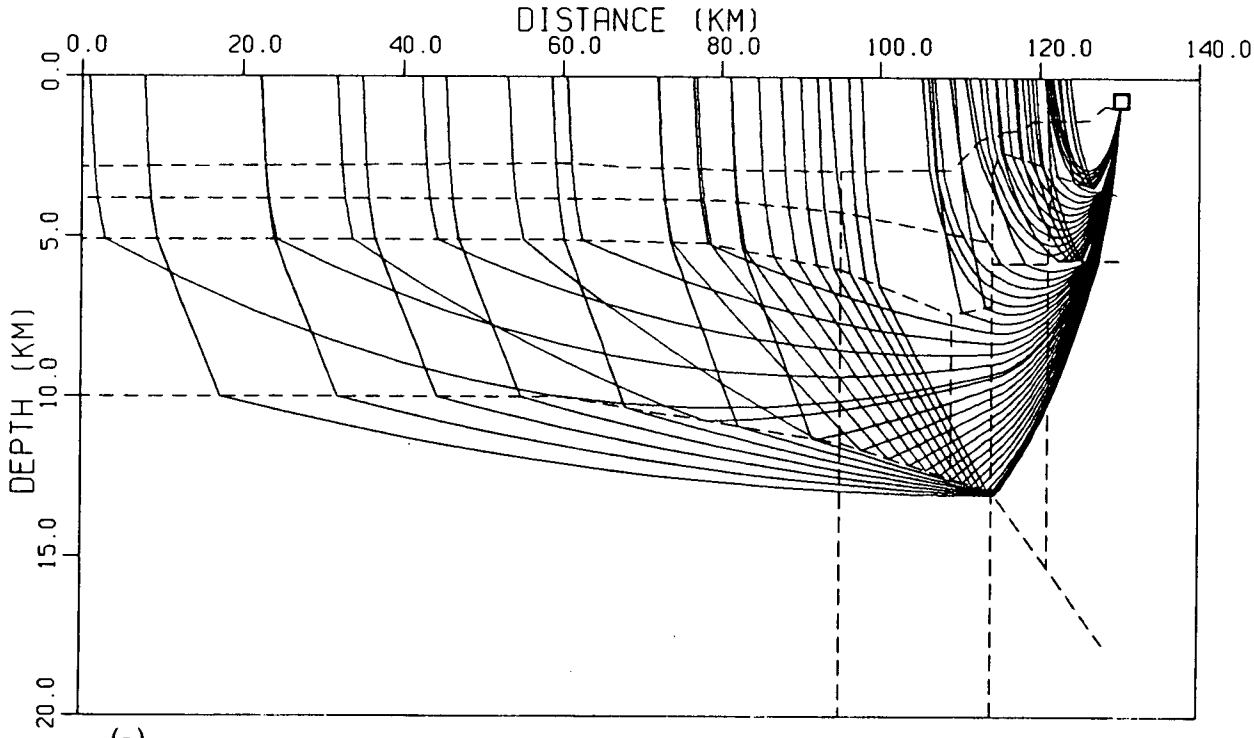


(a)

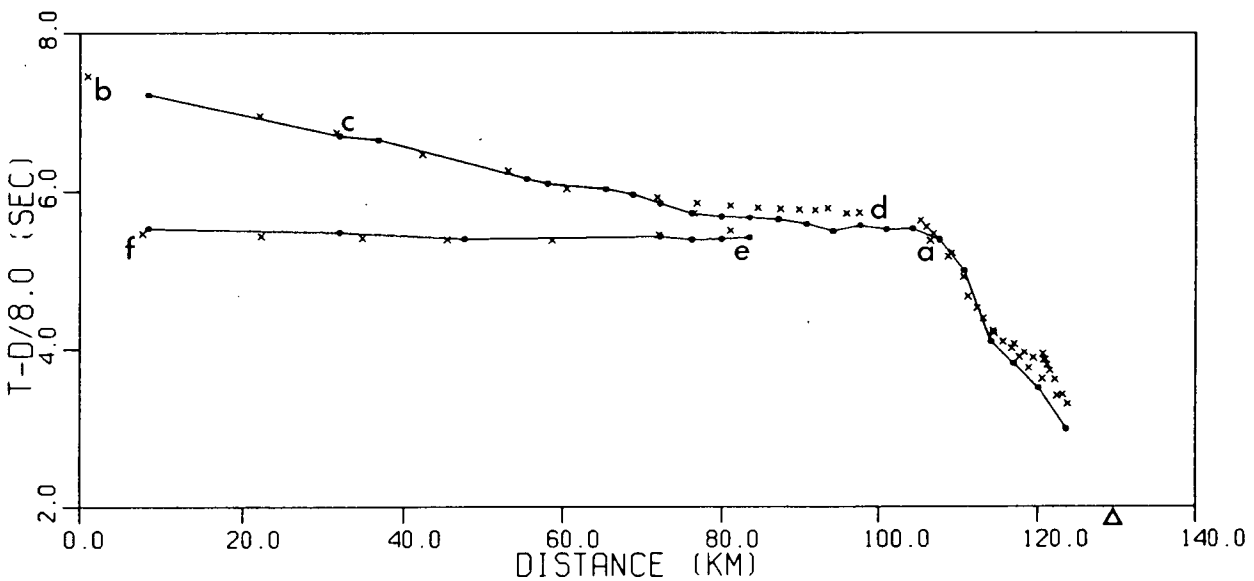


(b)

**Figure 24.** Ray tracing model (a) and traveltimes (b) for receiver 010, located at 130 km model distance.

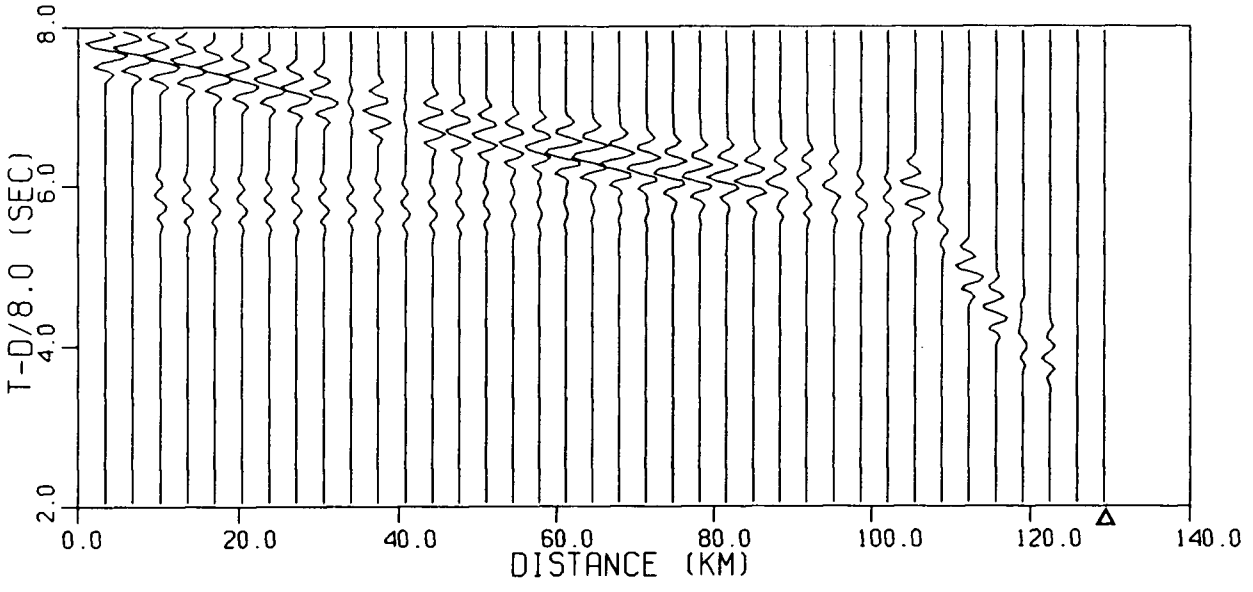


(a)

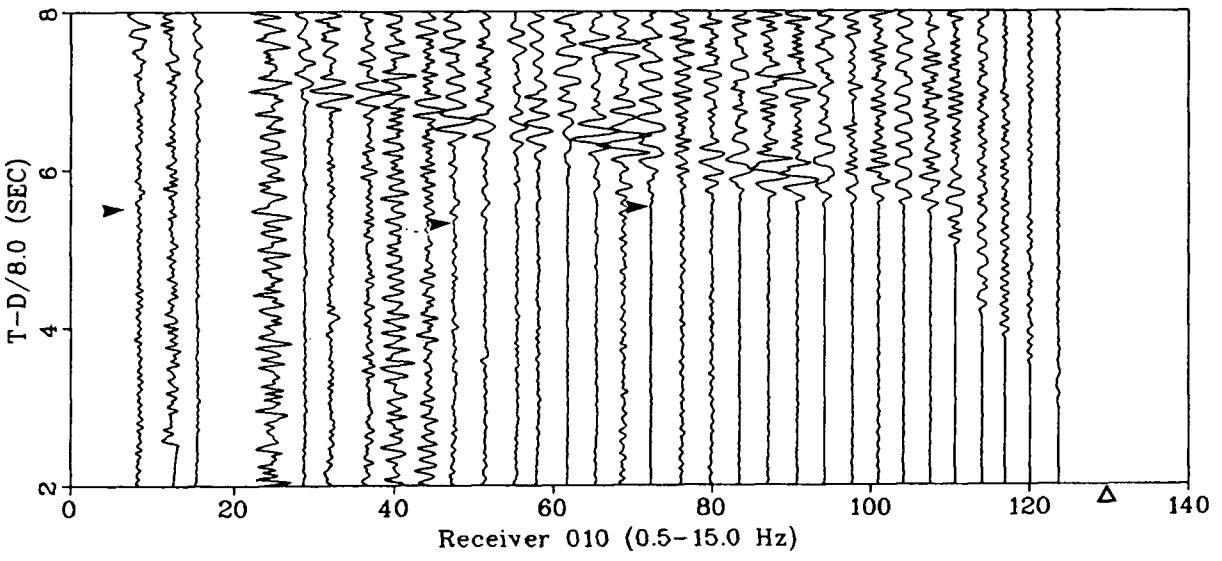


(b)

**Figure 25.** Seismograms for receiver 010. (a) synthetic seismograms corresponding to figure 24. (b) observed data. The three-cycle source wavelet used for the synthetic seismograms was taken from the data. The receiver is located at 130 km model distance. Low amplitude mantle refractions are indicated with arrows in (b).

mantle refraction arrivals. These arrivals (e to f in figure 24b) presently agree well with the observed arrivals of apparent velocity 7.9 km/s.

The synthetic seismograms and observed data for receiver 010 are shown for comparison in figure 25. Rays which travelled through the upper terrace region have generally moderate amplitudes that are slightly lower on the data section for presumably the same reaons mentioned earlier. The amplitudes of ocean crust refractions gradually increase across the section from their initially moderate level near the outer fault; amplitude fluctuations occur near 40 km as Moho reflections interfere with the crustal refractions. Mantle refractions have very weak amplitudes on the synthetic seismograms; they are barely visible on the data west of 40 km because of the noise level. The amplitudes of the arrivals on the synthetic seismograms increase slightly with increasing shot–receiver distance. This trend cannot be confirmed on the data section.

### 5.3 Receiver 020

Receiver 020 (OBSW2) was situated on the continental shelf just east of the terrace and across the Queen Charlotte Fault (QCF) from OBSW1. The initial model from receiver 010 was extended across the remaining terrace region by inserting the reversed airgun profile OBSW1 EAST — OBSW2 (segment II in figure 15) between 130 and 143 km and assuming starting velocities for the region beneath it. Crustal velocity estimates and thicknesses were later refined by modelling.

The velocities of the sediments and upper terrace crust between 130 and 144 km were determined from the airgun data (figure 15). Ray tracing through the upper terrace region determined approximate locations for upper/lower crustal boundaries. Lower crustal velocities are not well constrained as these units represent only a small portion

of the rays' travelpaths. A velocity of 5.3 km/s was chosen for the block west of the QCF (block A in figure 26) to be consistent with the adjacent terrace blocks (figure 23). This required a rather high velocity of 6.5 km/s for the block east of the QCF (block B in figure 26) to achieve a good traveltime fit. The vertical boundaries seen within this block are used only to define velocity gradients and do not represent structural features.

Three groups of rays were used to model the observed traveltimes and amplitudes. The arrivals extending from 123 to 110 km as first arrivals represent refractions through the upper terrace. Secondary arrivals of apparent velocity 7.2 km/s (a to b in figure 26b) represent crustal refractions through the lower terrace and ocean crust. The time delay at 110 km again clearly shows the transition from terrace to oceanic structure. The refractions through the ocean crust in the model end abruptly at 69 km when the rays encounter the Moho. Reflections from the Moho are focussed into a narrow group of secondary arrivals between 102 and 112 km (c to d in figure 26b). The arrivals indicate a dip of 19° for this portion of the Moho. Refractions through the mantle are the first arrivals west of 100 km and extend across the modelled section with an apparent velocity of 8.1 km/s (arrivals e to f in figure 26b).

The synthetic seismograms and observed data for receiver 020 are presented in figure 27. The large amplitudes of the crustal refractions terminate abruptly at 69 km on the synthetic seismograms. A fairly low signal-to-noise ratio makes it difficult to locate the refraction arrivals on the data section beyond 90 km but they appear to continue to perhaps 55 km. Extending the modelled refractions to this distance would require a deeper Moho or lower terrace gradient, both of which would degrade the fit of the model to other data sets.

Refractions through the mantle are of equally low amplitude on both sections. An increase in amplitude with increasing shot-receiver distance is observed for the synthetic

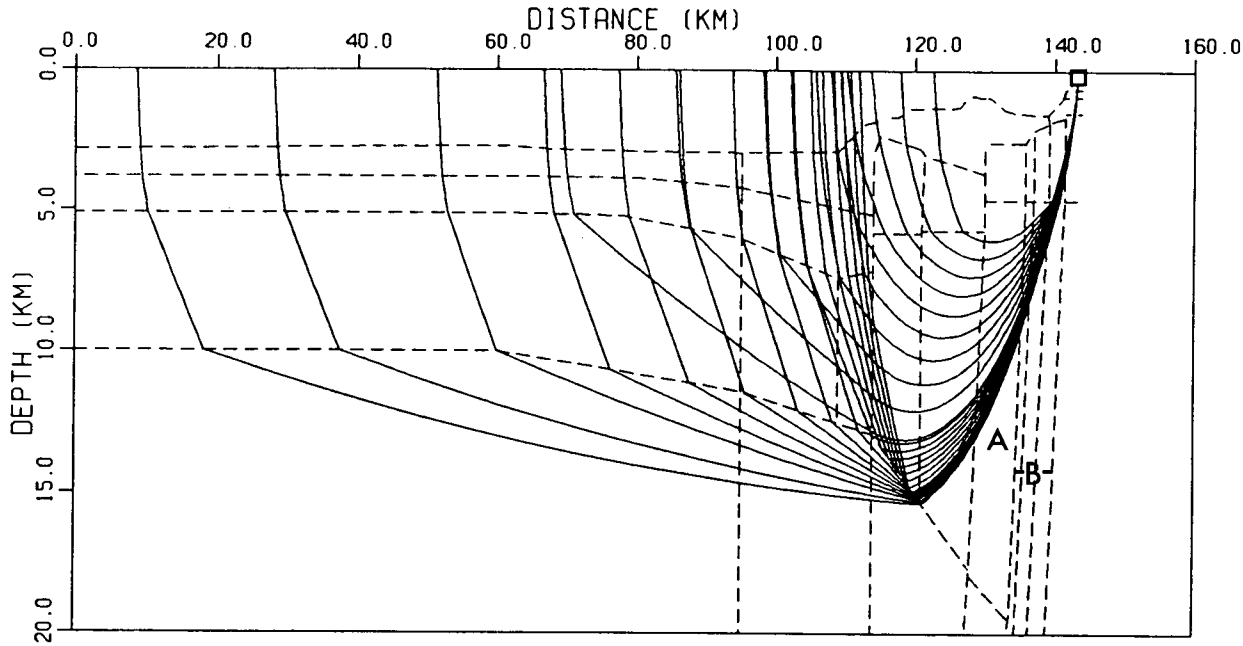


(a)

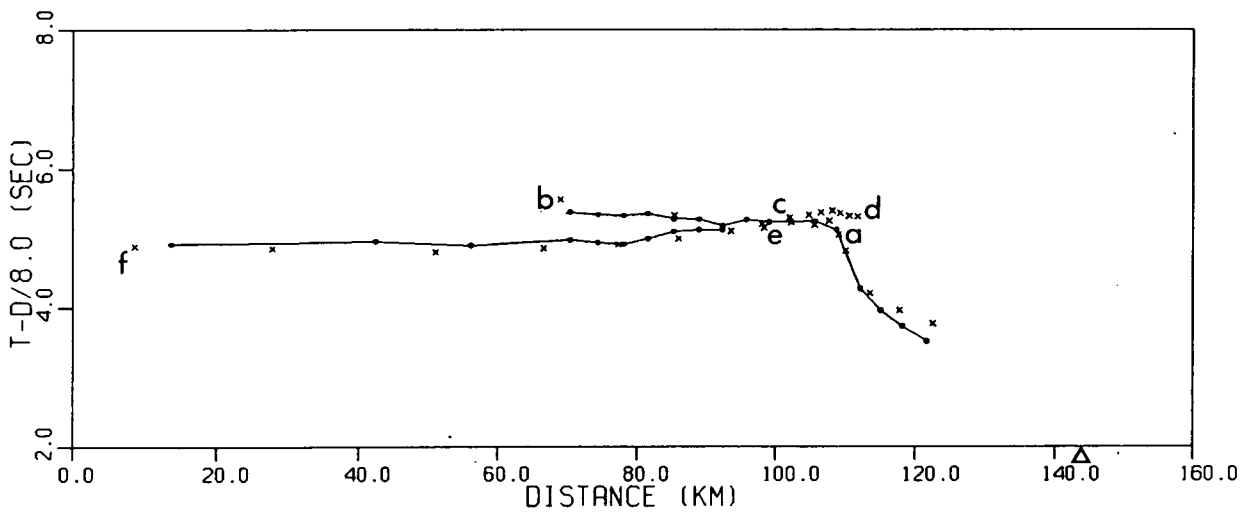


(b)

**Figure 26.** Ray tracing model (a) and traveltimes (b) for receiver 020, located at 143.1 km model distance. Numerous vertical lines in the model define velocity gradient directions and are not structural features.

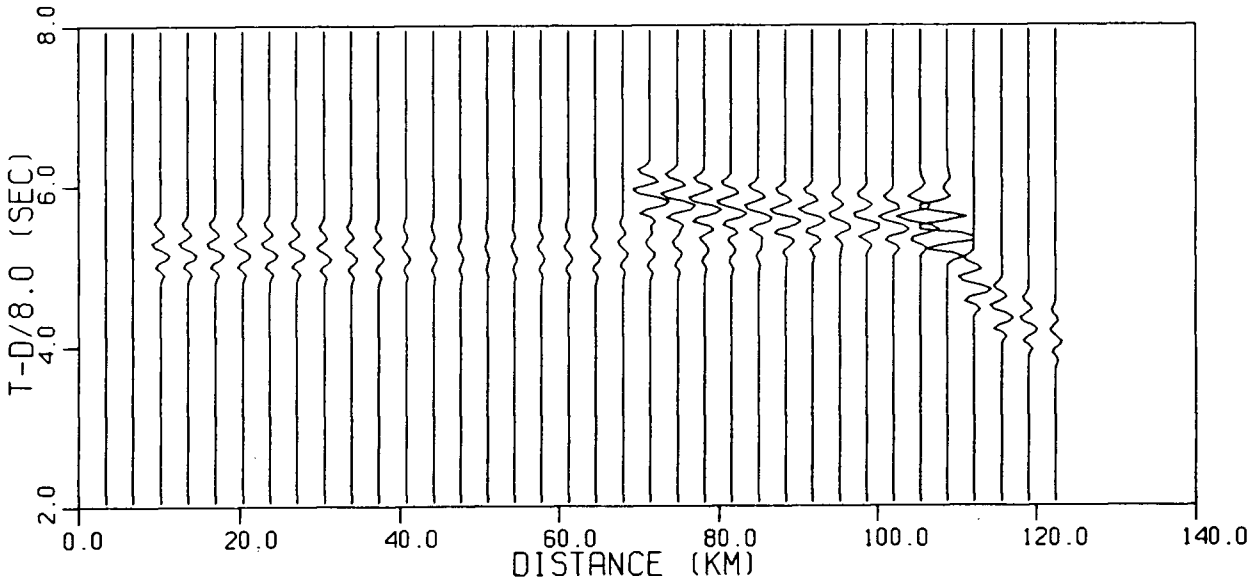


(a)

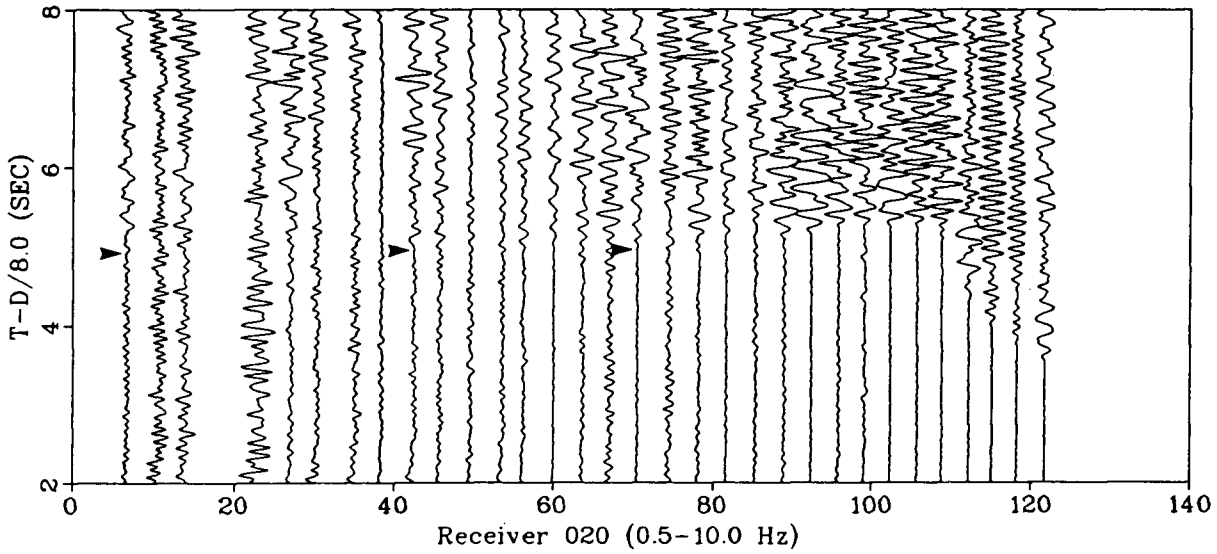


(b)

**Figure 27.** Seismograms for receiver 020. (a) synthetic seismograms corresponding to figure 26. (b) observed data. The receiver is located at 143.1 km model distance. The arrows in (b) indicate low amplitude mantle refractions.

arrivals; the noise-laden signal on the data section unfortunately limits observations of amplitude characteristics at far offsets.

### 5.4 Receiver 030

Receiver 030 is a Backpack recorder located near the western shore of Moresby Island. Rays travelling to the receiver from all shots must pass through the terrace and the continental crust beneath the island. The velocity structure of the island is poorly defined as few studies have sampled the region.

Extensive mapping of surficial geology provided the basis for a stratigraphic and structural analysis of the Queen Charlotte Islands (Sutherland Brown, 1968). Several geologic cross sections were constructed in a southwest-northeast direction across the islands and one of these is fortunately located within 3 km of the LBSs on Moresby Island. This profile (figure 28) can be divided into three major sections. West of the Louscoone Fault the subsurface is composed primarily of Triassic lavas of the Karmutsen Formation overlain in regions by Upper Triassic limestones of the Kunga Formation. Severe deformation and faulting has occurred between the Louscoone and Rennell Sound Faults. Near-surface units within the fault zone are primarily Jurassic and Cretaceous in age and generally consist of volcanics of the Yakoun Formation, calcareous siltstone of the Longarm Formation, and sandstones of the Haida and Honna Formations. East of the Rennell Sound Fault lie volcanics of the Yakoun Formation which are overlain by Haida Formation sandstones in the western half. Vertical offset across the Rennell-Louscoone Fault zone is estimated as 600 to 3000 m with the east block dropped down (Sutherland Brown, 1968). The stratigraphic interpretation of the profile was used to obtain crude estimates of upper crustal thickness and velocity for the model.

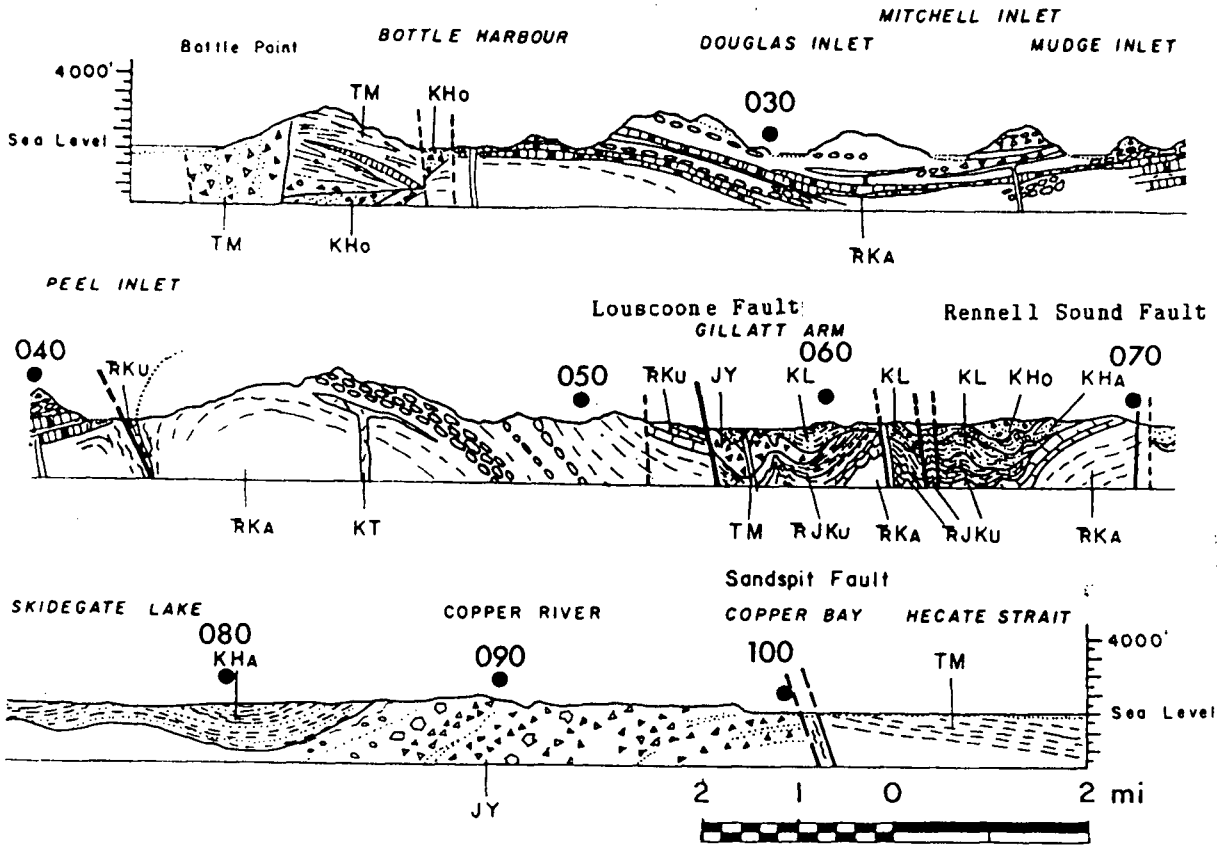


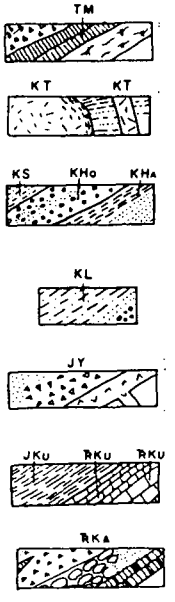


**TERTIARY**

TM Massett Fm: breccias, columnar basalts, rhyolites

**CRETACEOUS AND TERTIARY**

KT Post Tectonic Plutons: diorite, quartz, granite

**CRETACEOUS**

Queen Charlotte Group

KS Skidegate Fm: shale, siltstone, sandstone

KHo Honna Fm: conglomerate, feldspathic sandstone

$KH_A$ Haida Fm: shale, sandstone

KL Longarm Fm: calcareous siltstone, lithic sandstone

**JURASSIC**

JY Yakoun Fm: volcanic sandstone, tuff, sill

**TRIASSIC AND JURASSIC**

$JK_U$ Kunga Fm: flaggy argillite

$T_RK_U$ Kunga Fm: flaggy and massive limestone

**TRIASSIC**

$T_RK_A$ Karmutsen Fm: limestone, pillow lavas, flows

**Figure 28.** Geologic cross-section across Moresby Island near the receiver locations (after Sutherland Brown, 1968). Approximate receiver positions for this experiment are indicated.

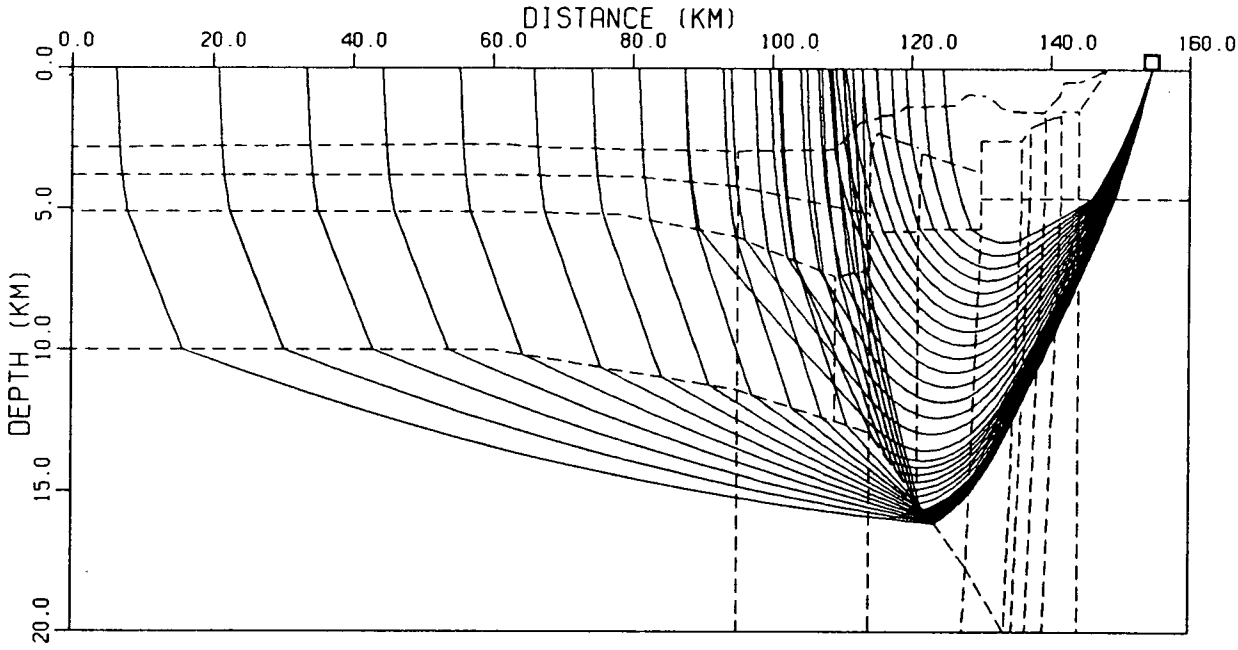


(a)

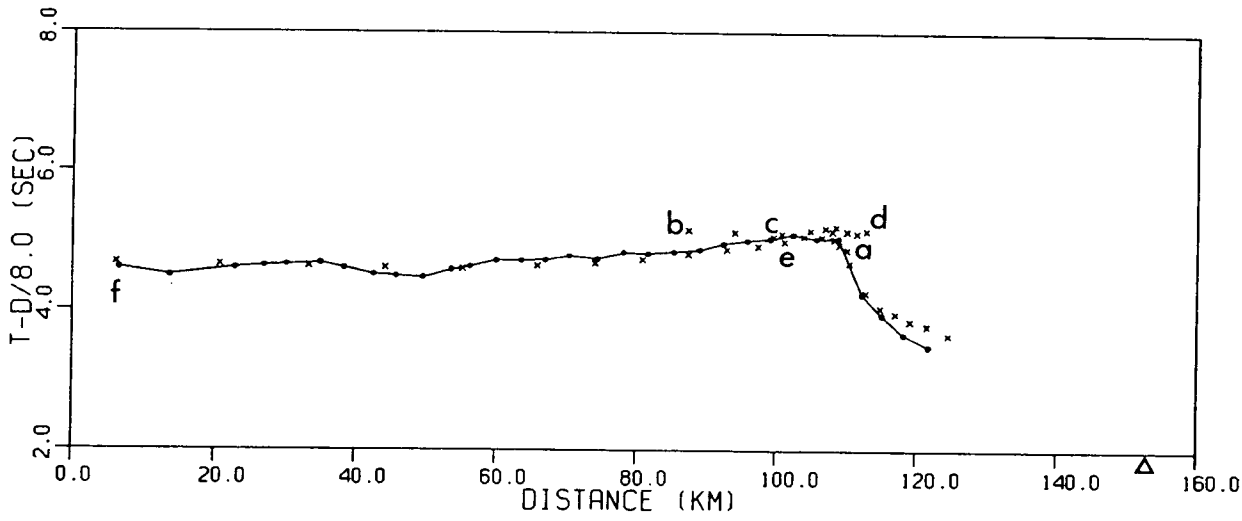


(b)

**Figure 29.** Ray tracing model (a) and traveltimes for receiver 030, located at 154.5 km model distance.

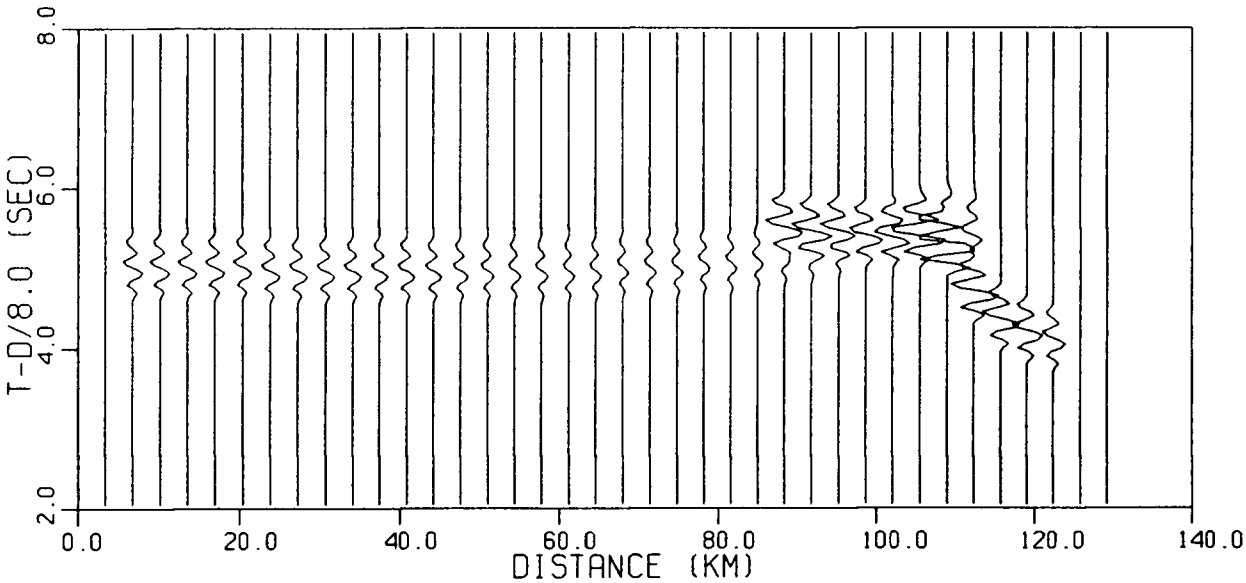


(a)

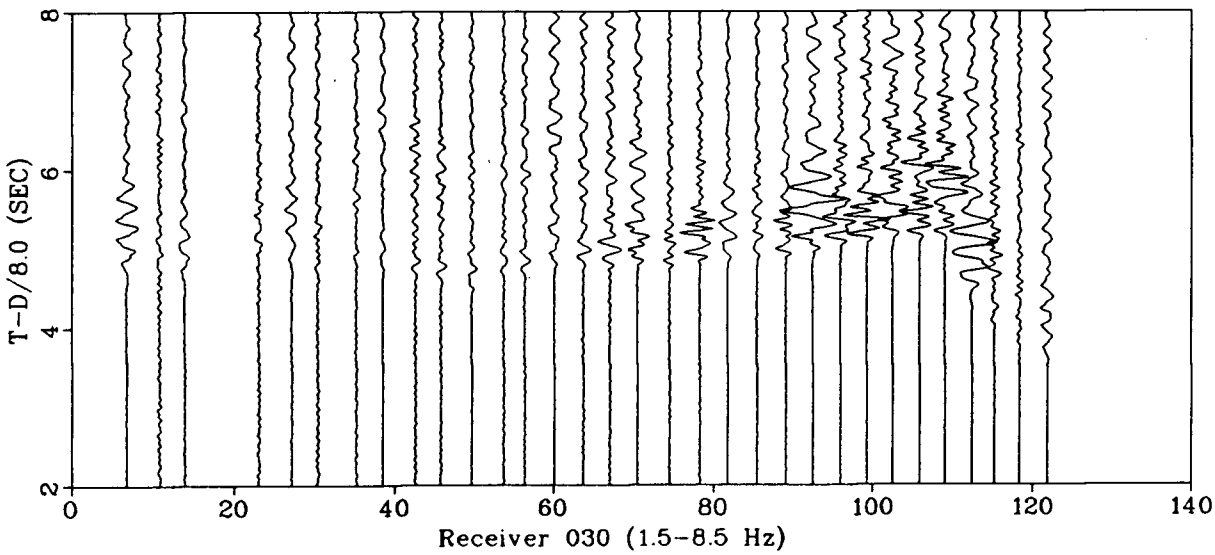


(b)

**Figure 30.** Seismograms for receiver 030. (a) synthetic seismograms corresponding to figure 29. (b) observed data. The receiver is located at 154.5 km model distance.

The ray tracing model and traveltime plots are shown in figure 29. Three groups of rays were again involved in the interpretation. Refractions through the lower crust of the terrace are seen as first arrivals from 122 km until the outer fault offset at 110 km. Arrivals from 108 to 87 km with apparent velocity 7.6 km/s (a to b in figure 29b) are from rays that continued through the fault into the lower oceanic crust until they were stopped at the Moho. Reflections from the Moho are again limited to a branch of secondary arrivals from 110 to 114 km (c to d) and confirm the previously determined Moho dip of 19°. Deeper travelling rays were refracted at the Moho and travelled through the mantle to form the 8.2 km/s apparent velocity branch (e to f) that intersects the lower crustal refractions at 103 km on the traveltime plot.

The synthetic and observed seismograms are shown in figure 30. The high amplitude arrivals seen on the data between 110 and 90 km correspond well to the modelled refractions through the lower oceanic crust. Additional energy is provided by the slightly later Moho reflections between 103 and 113 km. The much weaker mantle refractions continue across both sections from 100 km and increase slightly in amplitude with distance.

### 5.5 Receiver 060

Receiver 060 is a Backpack recorder located midway across Moresby Island in the Rennell-Louscoone Fault zone (figure 28). The surface geology indicates that vertical displacement of units adjacent to the fault zone has certainly occurred. However, rays arriving at receiver 060 are apparently not affected so there is no major velocity contrast across the fault at the depth concerned.

The ray tracing model and corresponding traveltimes are shown in figure 31. The only change from the previous model is the extension of the island structure to the receiver 060 location. The fault and vertical offset shown at 172 km have no effect on ray paths or traveltimes and were included in the final model to satisfy the receiver 100 data discussed in the next section.

The results of the ray tracing are very similar to those for receiver 030. Crustal refractions, Moho reflections, and mantle refractions are again the predominant ray groups involved. The high terrace gradient and Moho depth have further restricted the range to which crustal refractions can occur and all arrivals modelled west of 100 km are mantle refractions. The eastward dip of the Moho between 60 and 110 km is clearly evident in these refraction arrivals as they show an unrealistically high apparent velocity (8.8 km/s) in this region before assuming the more reasonable 7.9 km/s for the horizontal region.

The seismograms (figure 32) show the concentration of high amplitude crustal refraction arrivals east of 98 km and the continuous low amplitude mantle refractions extending westward across the section. Arrivals on the data section are very clear to large shot–receiver distances, especially for the big shots, and show well an amplitude increase with distance of the theoretical mantle refractions.

### 5.6 Receiver 100

The last common receiver gather modelled was for receiver 100, a microcorder located near the eastern shore of Moresby Island. Rays travelling to the receiver from the shots will be passing through lower crustal material east of the Rennell–Louscoone Fault zone and will be sensitive to the thickness of the crustal blocks. Combining the

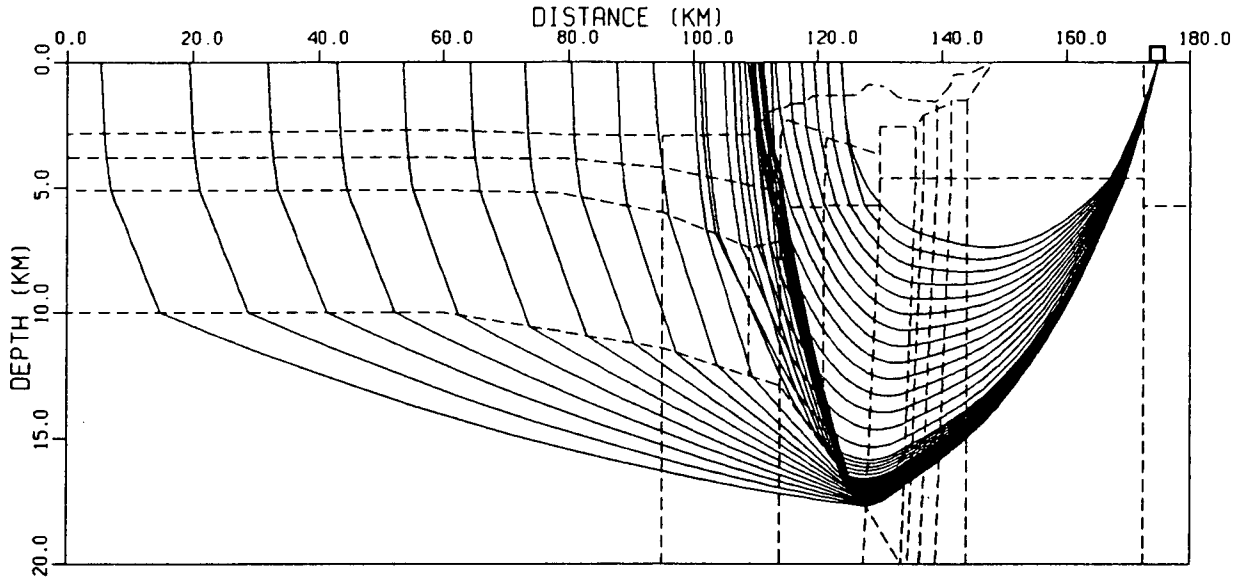


(a)

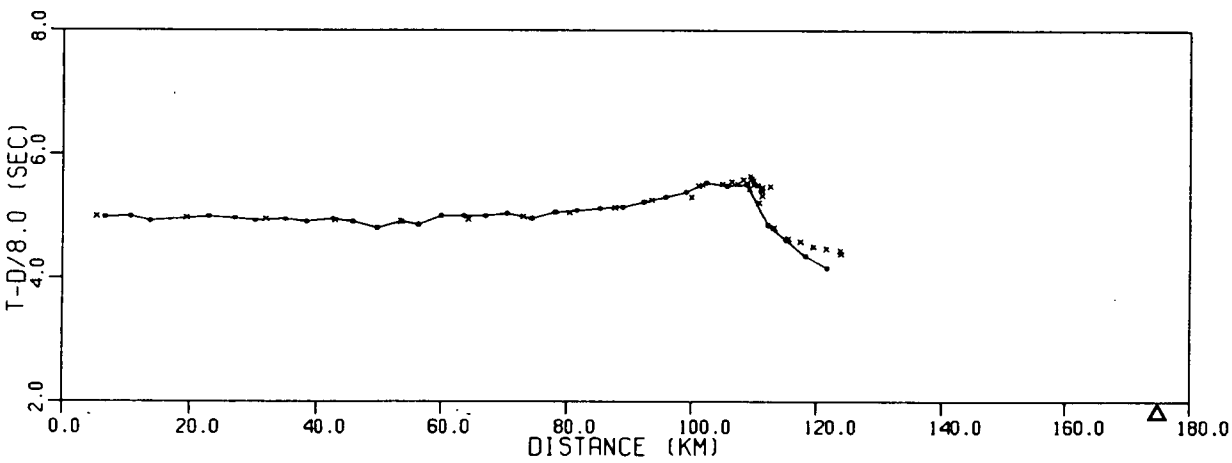


(b)

**Figure 31.** Ray tracing model (a) and traveltimes (b) for receiver 060, located at 174.8 km model distance.

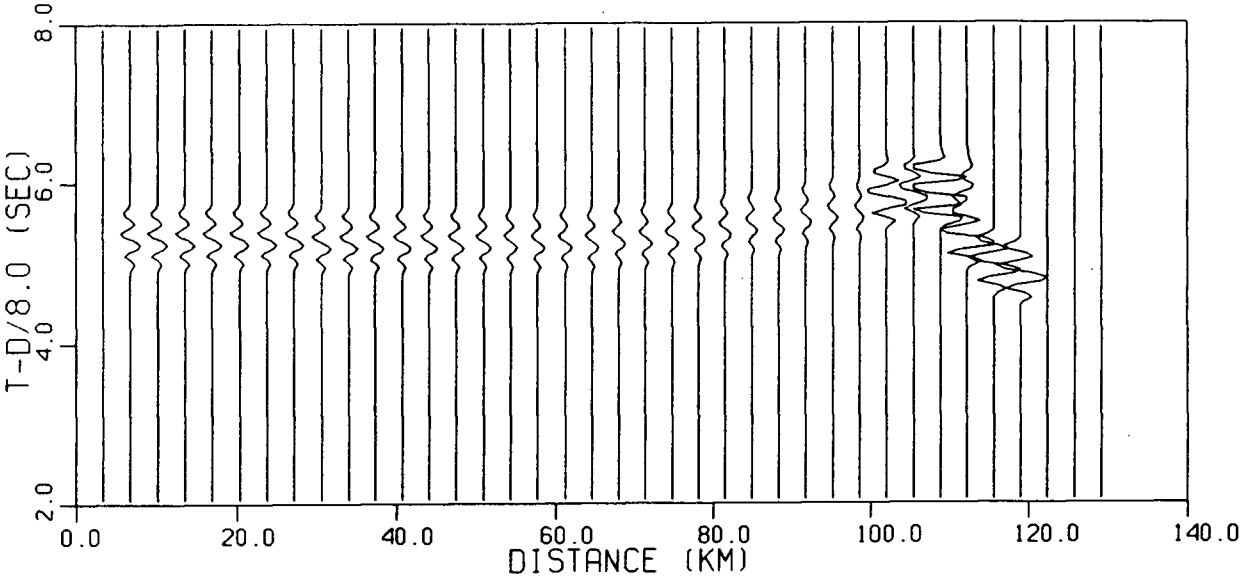


(a)

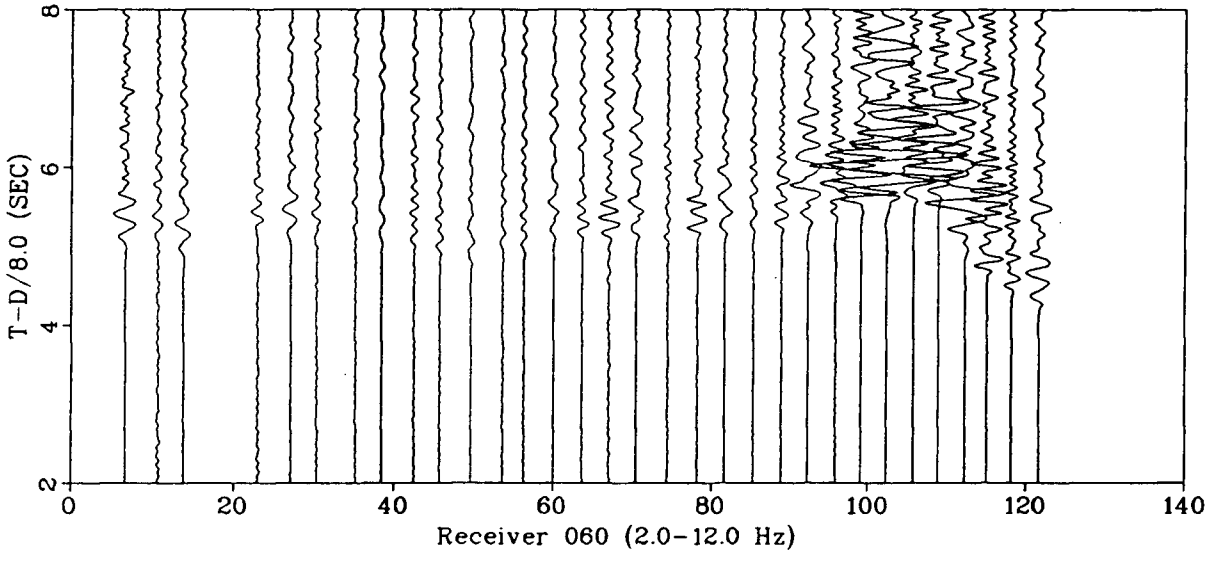


(b)

**Figure 32.** Seismograms for receiver 060. (a) synthetic seismograms corresponding to figure 31. (b) observed data. The receiver is located at 174.8 km model distance.

constraints of this model with those of receiver 060 should provide an estimate of vertical displacement at depth across the RLF zone.

The island structure of the receiver 060 model was extended uniformly to receiver 100; the upper crustal structure east of the RLF was then varied in subsequent modelling. The model that provides the best overall fit is shown with corresponding traveltimes in figure 33.

Traveltimes for crustal refractions, seen on the time plot between 115 and 104 km, are satisfied by downdropping the easternmost crustal block 0.4 to 2.0 km. The best fit for all arrivals was achieved with a vertical displacement of 1.1 km. The remaining arrivals are attributed to mantle refractions and a narrow band of Moho reflections between 105 and 116 km (c to d in figure 33b). The refraction arrivals (e to f) have an apparent velocity of 11.1 km/s for the dipping Moho region and 8.06 km/s through the horizontal boundaries to the west.

The amplitudes of the synthetic seismograms (figure 34) match the observed seismograms well. The crustal refractions yield high amplitudes which are augmented by the Moho reflections. Low amplitude mantle refractions lead away from the the high amplitude arrivals starting at 105 km and continue westward across the section with slightly increasing amplitudes.

### 5.7 Shot 13

Shot 13 was a 540 kg explosion detonated approximately 48 km west of OBSW1 at 81.7 km model distance. The ray tracing model and traveltimes are presented in figure 35. Rays were traced from the shot position to the surface through the previously

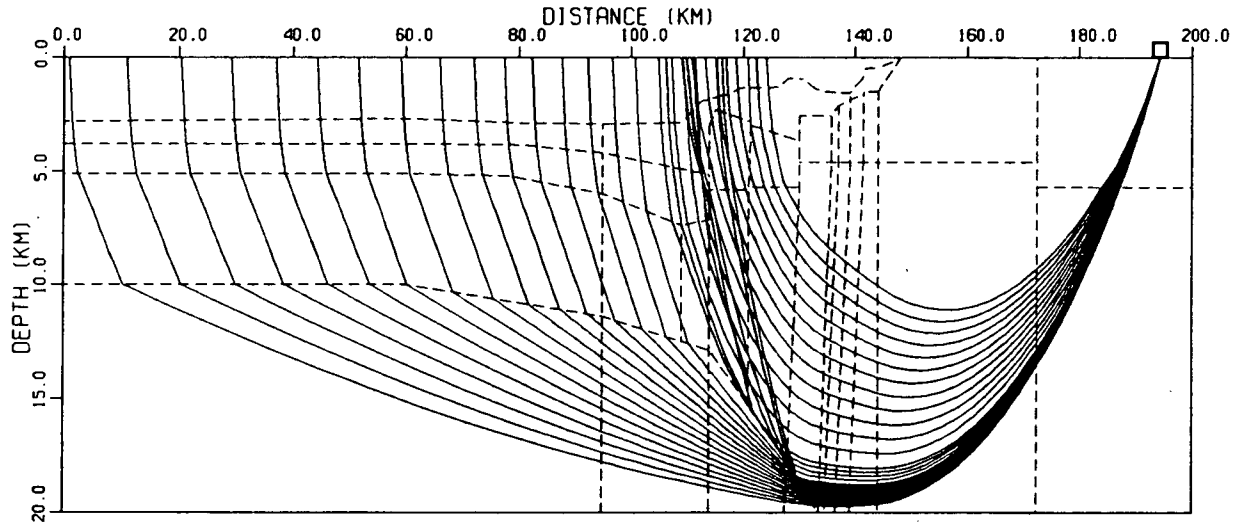


(a)

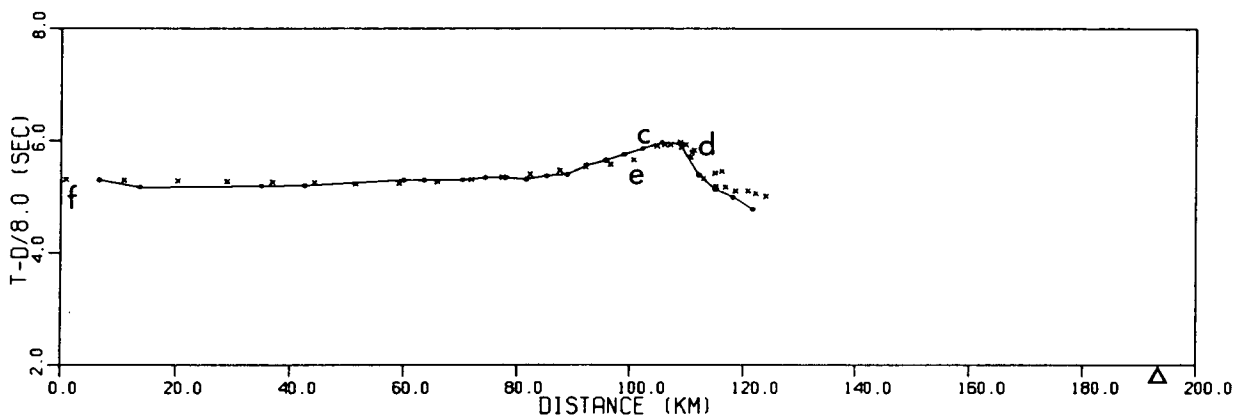


(b)

**Figure 33.** Ray tracing model (a) and traveltimes (b) for receiver 100, located at 194.3 km model distance.

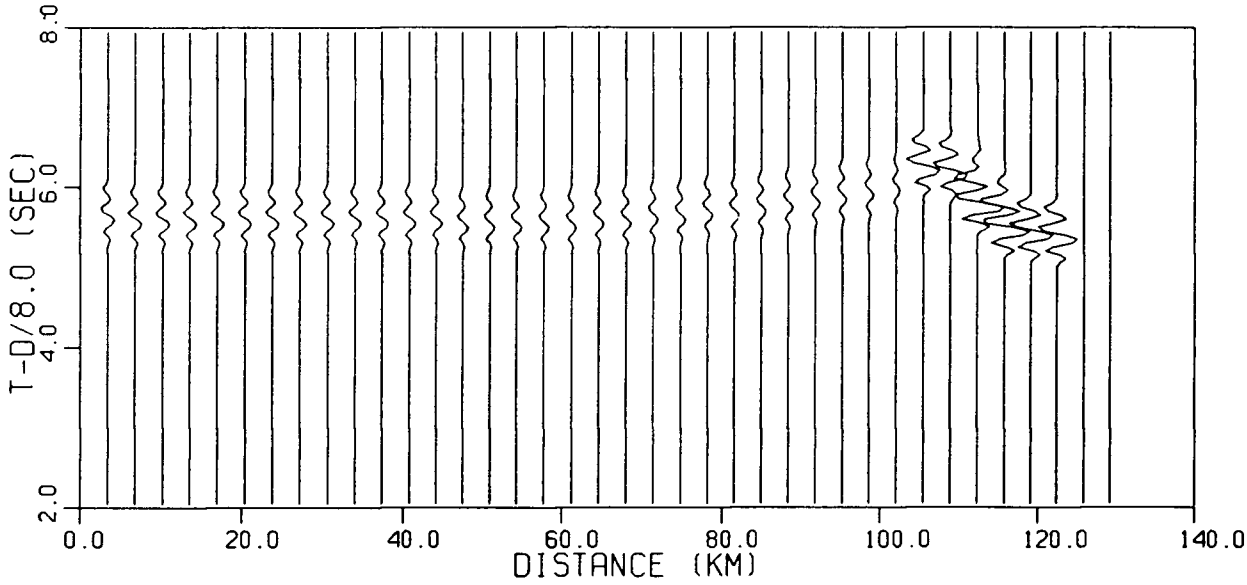


(a)

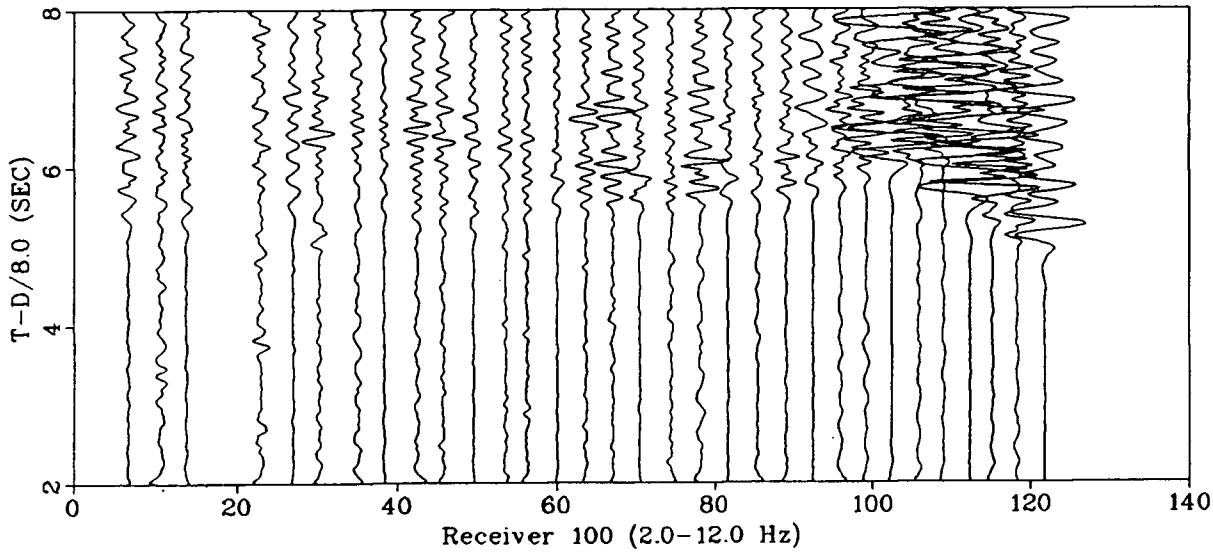


(b)

**Figure 34.** Seismograms for receiver 100. (a) synthetic seismograms corresponding to figure 33. (b) observed data. The receiver is located at 194.3 km model distance.

derived model. OBS positions were time-corrected to the surface for easy comparison of observed and computed traveltimes.

The terrace region was well sampled at all depths by the various ray groups, which consist of refractions through the oceanic crust and terrace, reflections from the oceanic Moho, and refractions through the mantle that surface through the terrace and island crust. The time plot shows good agreement between the theoretical and observed traveltimes. The computed first arrivals at all receivers are from rays refracted through the mantle. The secondary arrivals picked for receivers 010 and 020 (the OBSs) correspond to Moho reflections and crustal refractions respectively. The most distant reflection from the Moho surfaced at approximately 138 km so OBSW1 is the only receiver in this model that could record Moho reflections from this shot.

Figure 36b shows the observed data recorded by the ten receivers. Amplitude corrections were made for the different types of seismographs (Chapter II) but did not consider the siting of the instruments. While the LBSs were carefully sited on bedrock, the OBSs were presumably dropped into soft ocean bottom sediments. The resulting poor coupling would reduce the amplitudes of the recorded signals and make theoretical amplitude comparisons difficult.

The synthetic seismograms are presented in figure 36a. The high amplitude arrivals between 120 and 135 km are from Moho reflections. No corresponding high amplitudes were observed on the data recorded at receiver 010 (OBSW1). Similarly, the moderate amplitude crustal arrivals seen on the synthetic seismograms between 140 and 150 km were not observed on the OBSW2 data. Presumably the generally low amplitudes of these two observed seismograms are a result of their location on the soft ocean bottom. The mantle refractions observed across the remainder of the section generally match the arrivals recorded by the LBSs.

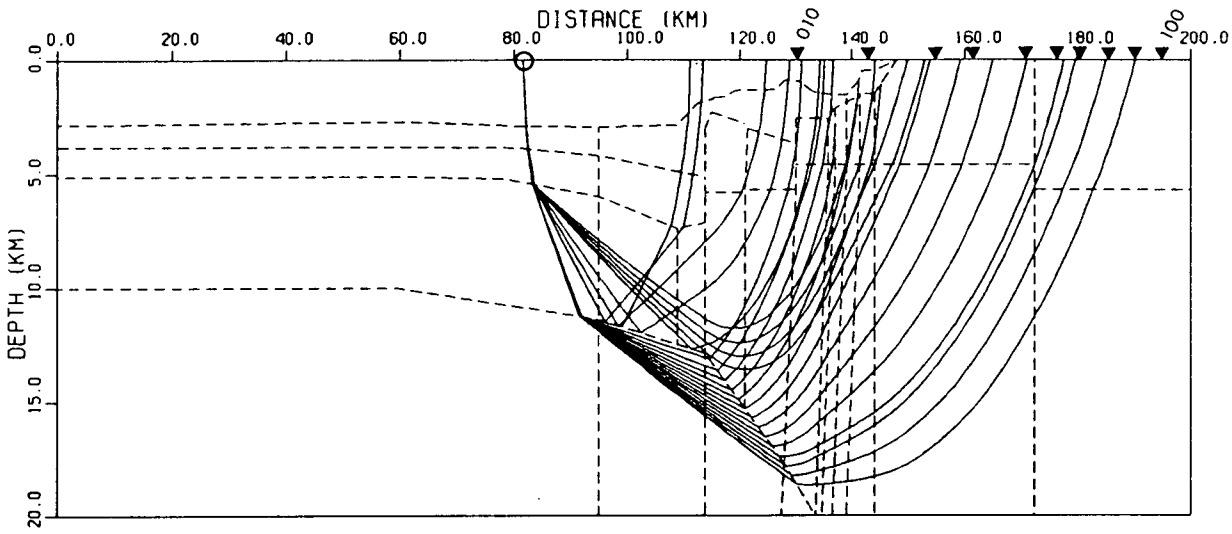


(a)

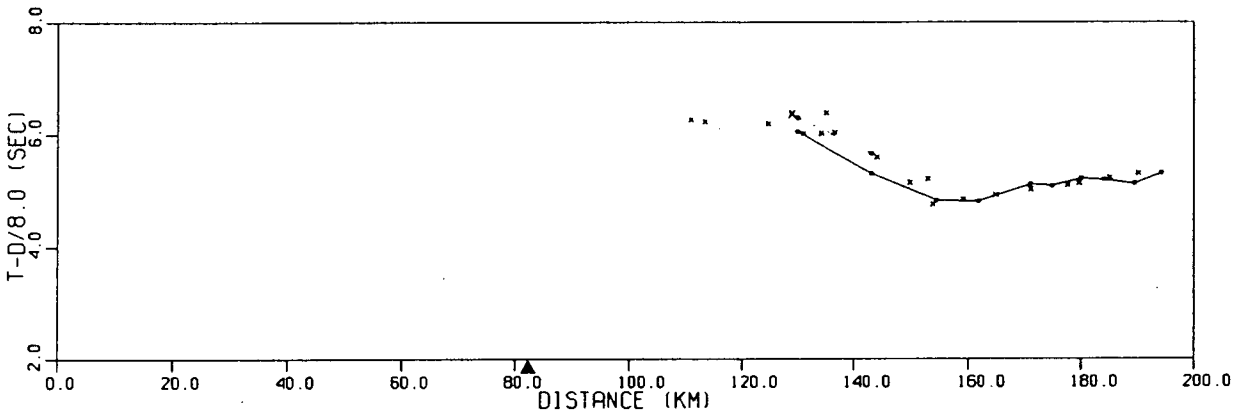


(b)

**Figure 35.** Ray tracing model (a) and traveltimes (b) for shot 13, located at 81.7 km model distance. Receiver locations are indicated.

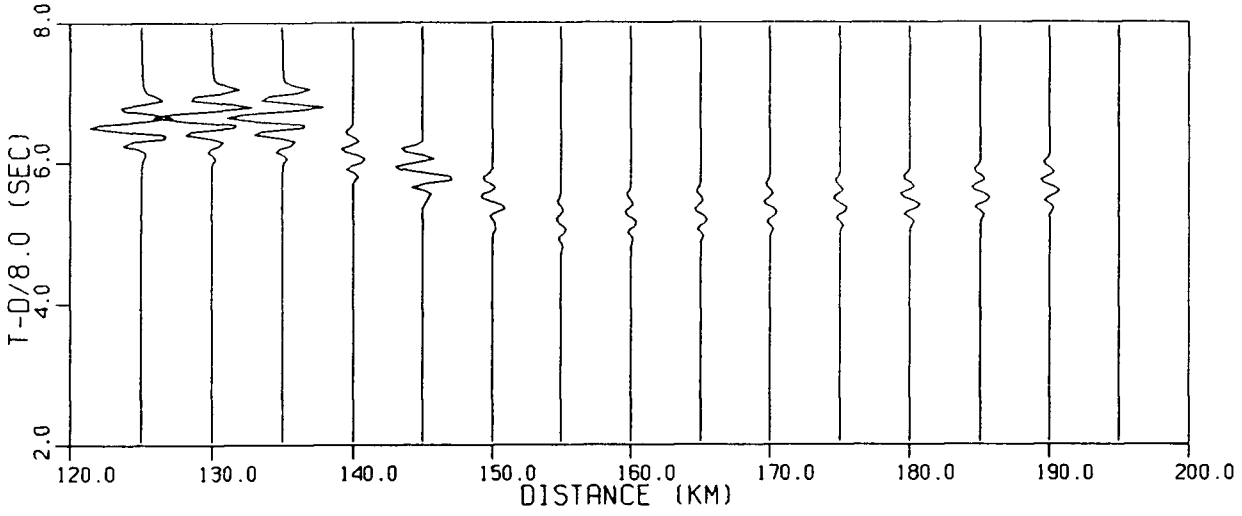


(a)

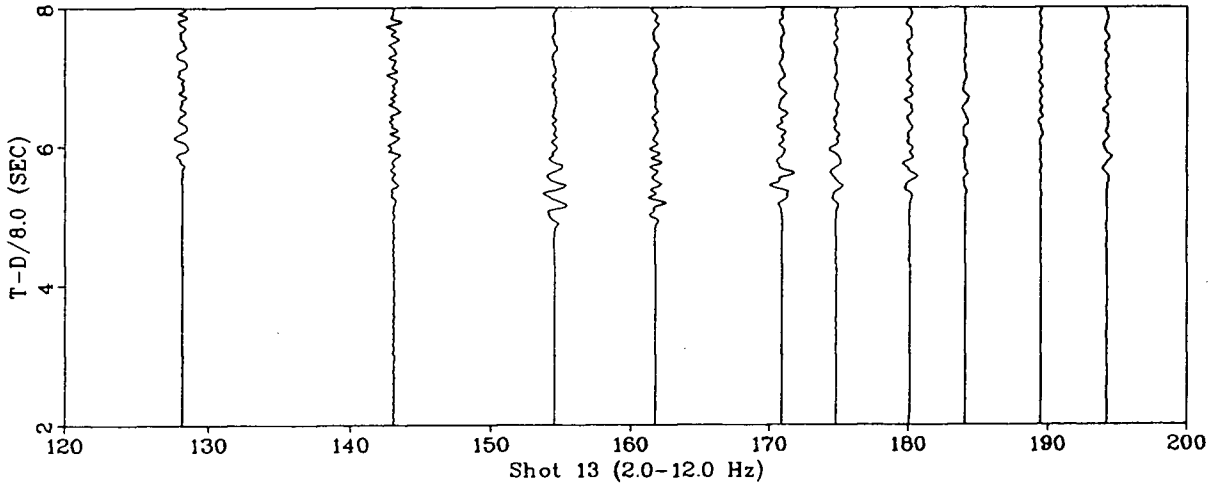


(b)

**Figure 36.** Seismograms for shot 13. (a) synthetic seismograms corresponding to figure 35. (b) observed data, from receiver 010 at left to receiver 100 at right. The shot is located at 81.6 km model distance.

## 5.8 Shot 25

Shot 25 was a more distant 540 kg explosion detonated approximately 91 km west of OBSW1 at 38.4 km model distance. Rays traced from this shot to the surface near the 10 receivers sampled the ocean crust west of the terrace, the terrace itself, and the upper mantle and island crust.

The model and traveltime plot are shown in figure 37. Three groups of rays were again used to reproduce the observed traveltimes. The first group was refracted through the oceanic crust and travelled near-horizontally before being refracted sharply upwards to the surface by the high velocity gradient within the terrace. These rays are seen as secondary arrivals between 124 and 138 km on the traveltime plot (a to b in figure 37b). The second ray group was reflected from the shallowly dipping Moho west of the terrace and travelled upwards through the oceanic and terrace regions. The corresponding traveltime arrivals begin at 80 km and become successively later to join the crustal refraction arrivals at 133 km (c to d). The final group represents rays that were refracted into the mantle at the oceanic Moho and were subsequently refracted back to the surface through the various crustal structures at the dipping Moho beneath the terrace. These rays are the first time arrivals between 100 and 200 km (e to f) and fit the observed traveltimes well. The "V" shape of the arrivals is due to the dip of the Moho and the velocity structural contrast between the terrace and the island.

The synthetic and observed seismograms are shown in figure 38. The low overall amplitudes and the noise on the receiver 010 and 020 traces makes amplitude comparison difficult but there appears to be good general correlation between the sections. Crustal refractions and Moho reflections are the source of the high amplitude secondary arrivals between 120 and 135 km. The reduced amplitude on the synthetic trace at 130

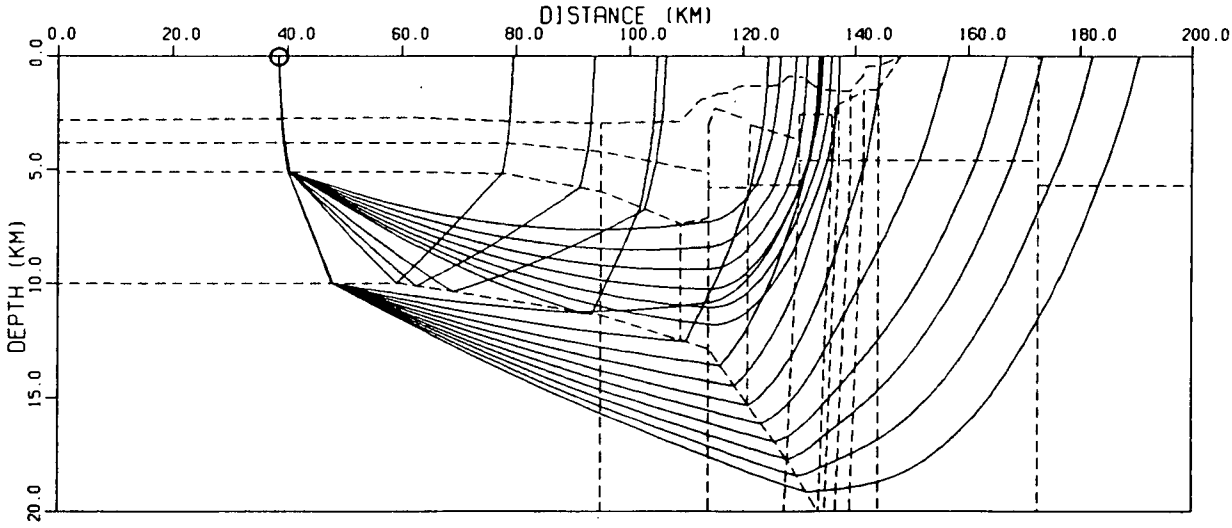


(a)

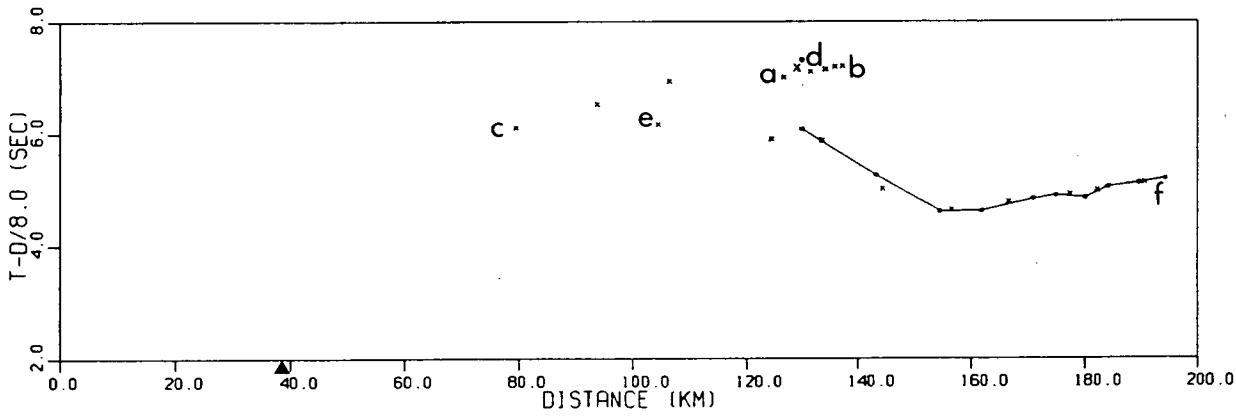


(b)

**Figure 37.** Ray tracing model (a) and traveltimes (b) for shot 25, located at 38.4 km model distance.

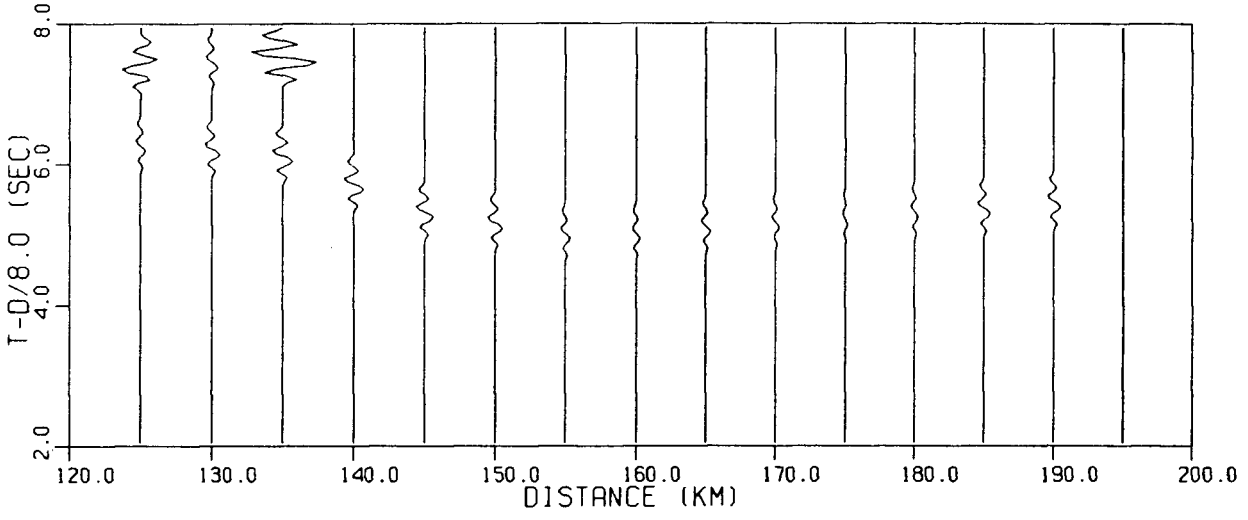


(a)

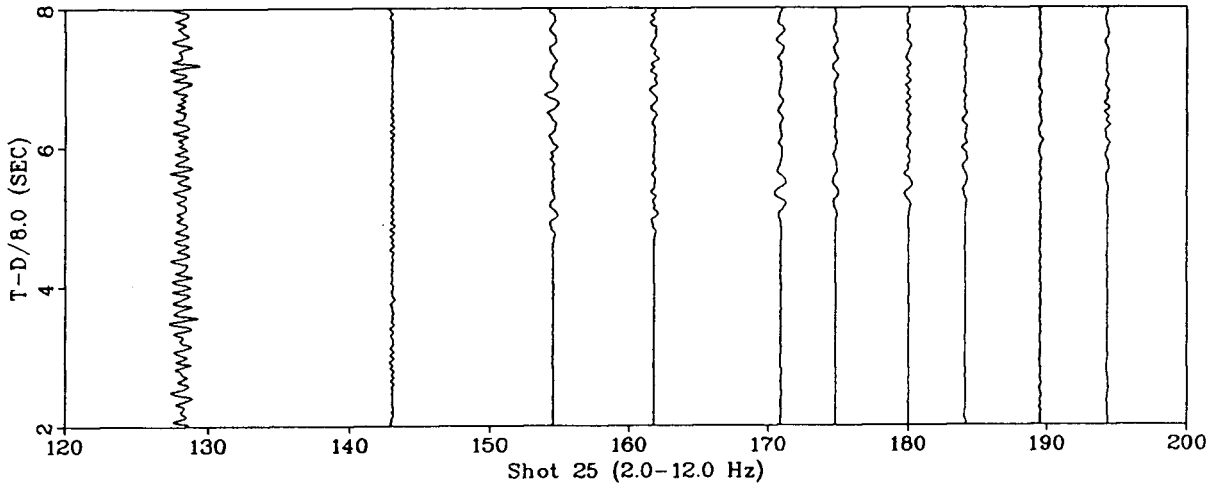


(b)

**Figure 38.** Seismograms for shot 25. (a) synthetic seismograms corresponding to figure 37. (b) observed data, receivers 010 to 100. The shot is located at 38.4 km model distance.

km is the result of destructive interference between the two types of arrivals. Low amplitude mantle refractions can be followed across the section and reproduce the observed amplitudes quite well.

### 5.9 The Final Velocity Model

The final model based on the complete ray tracing interpretation was presented in figure 23. The model can be divided into three major structural components (ocean, terrace, and island) which will be discussed individually.

The region extending from the beginning of the model to the edge of the terrace at 114 km comprises the oceanic segment. An average 1 km of sediments (unit 2) overlie a 6.2 km thick oceanic crust which has been subdivided into a lower velocity 1.3 km thick upper unit (unit 4) and a higher velocity lower unit (unit 9). A low velocity gradient (0.012 km/s/km) is required for unit 9 to enable crustal refractions from the distant shots to reach all the receivers.

Beneath the crust lies the oceanic mantle (unit 13) with a velocity of 7.9 km/s. West of 60 km a horizontal Moho at 10 km depth satisfied the available data. East of 60 km the Moho begins to dip towards the mainland, first at a gentle 2.3° and then at 4.5° to the edge of the terrace. The depth of the Moho in this region is well constrained by reflections and the cessation of crustal refractions.

The terrace region extends from 114 km to the QCF at 135.8 km. Although it too is composed of three major units, it is structurally much more complicated than the oceanic region. The uppermost layer consists of low velocity deformed sediments of irregular surface topography and variable thickness. The upper crustal unit has been separated into three blocks (unit 5) by vertical faults to satisfy the airgun data, although

a more complicated structure may be present. The vertical extent of the faults into the adjacent units could not be determined; surface topography however suggests that the fault at 130 km extends to the ocean floor.

The lower crustal unit (unit 10) has an anomalously low velocity and fairly high gradient as required by the crustal refractions. It has been modelled as a homogeneous unit although faults may complicate the structure. The Moho dips beneath the terrace at 19° as determined from mantle refractions and a few unreversed Moho reflections. The Moho dip and mantle depth are dependent on the velocity structure of the terrace and would vary if it were altered. Good agreement is found, however, with the 20° dip determined by Horn et al. (1984) off southern Moresby Island, although their model was more poorly constrained at this level than that of the present study. Mackie (1985), in a seismic refraction study of the Queen Charlotte Islands/Hecate Strait region, determined a Moho dip of 5° extending from the outer edge of the terrace to the mainland of British Columbia and a 2° dip beneath the oceanic crust to the west. The simplified velocity structure that he used for the terrace and QC Islands will permit small variations in these values, but the study nonetheless indicates a shallower regional Moho dip than the 19° value obtained in this study for the limited region beneath the terrace. This suggests that the steeper dip beneath the terrace may be local and the dip may decrease beneath the QC Islands.

The island region east of the QCF to 200 km represents the edge of the continental structure of North America. Sampling density decreases towards the end of the model and the structure can only be roughly approximated. The region adjacent to the QCF appears distinct from the other island structure at all model depths. A 1 km thick unit of stratified, 2.35 km/s sediments (unit 3) overlies the crustal units. The upper crust again appears to be faulted and is divided into two distinct velocity units at 137 km.

The division has been modelled as a vertical fault but is not so constrained. The upper crust (unit 7) has been modelled with a slightly higher velocity (4.1 km/s) than the oceanic crust (3.8 km/s) with the exception of the 1.2 km wide sliver next to the QCF (unit 6) which has a lower velocity (3.4 km/s). A higher velocity and lower gradient were determined for the lower crust here (unit 11) than for the adjacent lower continental crust (unit 12). However, these values are not well constrained and the two units may be much more similar.

The remaining island structure has been roughly divided into two units based on stratigraphic information. The upper unit (unit 8) has a velocity of 5.0 km/s at the surface and moderately high gradient. There is little velocity difference at the 5 km deep boundary between units but the gradient has been significantly reduced for the lower unit (unit 12). A modelled offset on the Rennell-Louscoone Fault has displaced the eastern half of the upper unit 1.1 km downwards with respect to the adjacent part. The fault dip cannot be resolved to better than $\pm$ 30° nor the vertical displacement to $\pm$ 0.8 km. The mantle was not sampled beneath the island and total crustal thickness is therefore unknown.

A geologic interpretation of the velocity structure is necessary to fit the derived model into the tectonic framework for the region. The next chapter will attempt to do this and answer some of the questions raised at the beginning of the study.

# CHAPTER VI DISCUSSION AND CONCLUSIONS

The application of two-dimensional ray tracing techniques has produced a velocity structural model for the region of the Queen Charlotte Fault zone. The fault—bounded terrace does not appear to be related to either of the adjacent crustal units but seems structurally distinct. A geologic interpretation of the velocity model will help to clarify the relationship between the observed structure and the present tectonic regime.

## 6.1 Stratigraphic Interpretation

The stratigraphic interpretation of the velocity units is summarized in table IV. Unit 2 is the sedimentary layer covering the terrace and ocean crust. Ocean bottom sediments west of Dixon Strait were interpreted as Late Miocene to Quaternary deposits (Snavely et al., 1981). Chase and Tiffin (1972) identified trench infill as Late Tertiary pelagic sediments overlain by well stratified Plio-Pleistocene turbidites and recent turbidity current deposits. Unit 3 is a higher velocity sedimentary unit underlying the narrow continental shelf east of the active fault and may be of terrigenous origin.

Units 4 and 9 represent upper and lower oceanic crust respectively. Ophiolite studies indicate that crustal layer 2 (unit 4) consists of an extrusive sequence of pillow lavas and basaltic sheet flows that grades down to dense dike swarms (Christensen and Smewing, 1981). An associated high velocity gradient is related to the increase of metamorphic grade with depth. Layer 2 velocities range from 3.7 to 6.5 km/s and average 5.5 km/s (Christensen and Salisbury, 1975). The difference between ophiolite sequence velocities of 5.0 to 6.0 km/s measured in the laboratory and the unit 4 model velocities of 3.8 to 4.3 km/s suggests the presence of large fractures within the uppermost crustal section which would significantly lower observed velocities (Christensen and Smewing, 1981).

| VELOCITY UNIT | VELOCITY (km/s) | GRADIENT (km/s/km) | STRATIGRAPHIC INTERPRETATION |
|---|---|---|---|
| 1 | 1.49 | 0.001 | water layer |
| 2 | 2.20 | 0.530 | pelagic and turbiditic sediments |
| 3 | 2.35 | 0.700 | shelf sediments |
| 4 | 3.80 | 0.350 | basaltic pillow lavas and sheet flows grading to dike swarms |
| 5 | 3.80 | 0.350 | deformed upper ocean crustal basalts or compressed sediments |
| 6 | 3.40 | 0.500 | sheared sediments or basalts |
| 7 | 4.10 | 0.400 | sheared sediments |
| 8 | 5.00 | 0.180 | tholeiitic basalts, granite, and limestone |
| 9 | 6.70 | 0.012 | interlayered gabbros and peridotites |
| 10 | 5.30 | 0.200 | sheared gabbros and peridotites ?? |
| 11 | 6.50 | 0.030 | continental silicic crust |
| 12 | 6.10 | 0.095 | continental silicic crust |
| 13 | 7.90 | 0.005 | harzburgite and dunite (mantle) |

**Table IV.** Stratigraphic interpretation of the velocity units of figure 23.

Oceanic crustal layer 3 consists of interlayered gabbros and peridotites of amphibolite facies metamorphism. Velocities in the Oman Ophiolite range from 6.7 km/s at the top of the layer to 7.3 km/s at its base (Christensen and Smewing, 1981). The lower crustal velocity determined by modelling (6.7 km/s for unit 9) agrees well with these laboratoy measurements.

Unit 13 represents the upper mantle which is composed primarily of tectonized harzburgite and dunite (Christensen and Smewing, 1981). The modelled mantle velocity (7.9 km/s) for the 8 Ma old oceanic lithosphere is lower than average mantle velocity measurements (8.15 km/s) but is in agreement with other observations of young oceanic lithosphere (Christensen and Salisbury, 1975).

Velocity unit 8 represents the upper crustal rocks of the Wrangellia terrane. The Karmutsen Formation, which outcrops at the surface between 190 and 212 km model distance, consists primarily of Late Triassic tholeiitic pillow basalts (Sutherland Brown, 1968). Estimates of ocean basalt velocities range from 3.7 to 6.5 km/s and a velocity of 5.04 km/s has been measured for basalts at the top of oceanic layer 2 (Christensen and Salisbury, 1975). An average velocity of 5.0 km/s is thus representative of the volcanics of the Karmutsen Formation and the younger rocks of the Yakoun Formation that outcrop to the east.

Unit 12, the lower continental crust, is poorly constrained in the model. Its upper boundary is not a velocity discontinuity but instead marks a reduction in gradient from the upper crust. The reduced velocity gradient required by the ray trace modelling may signify a change in metamorphic facies or composition.

The stratigraphic equivalents of the terrace velocity units are not readily apparent. The velocity of unit 5 suggests that it may be upper oceanic crust (unit 4) although de-

formation by thickening and faulting has clearly occurred. Alternatively, it may contain highly compressed sediments of oceanic or continental origin. Hyperbolae and disruptions, seismic signatures of irregular surface features, make it impossible to distinguish any subsurface structure on the available CDP data. Unit 7 may similarly be composed of sediment derived from the upper continental crust. The low velocity and position of the narrow unit 6 suggests that it has been extensively sheared and fractured by motion along the fault and may belong to either of the above mentioned crustal units.

Lower crustal unit 11 east of the fault is again not well defined and is probably related to the lower continental crust, unit 12. Unit 10 , however, has a low velocity and high gradient inconsistent with the other lower crustal units. The most acceptable hypothesis is that extensive deformation by compression and shearing has altered normal lower crustal material beyond easy recognition and masked the boundary between upper and lower crustal material.

### 6.2 Tectonic Implications

The fault structure of the velocity model is consistent with a compressional tectonic regime. The graben- and horst-like appearance of the upper terrace may in fact represent high angle reverse faults and low frequency compressive sediment folds as the fault angles are only constrained to $\pm$ 10°. The downward vertical displacement of the oceanic crust at the outer fault (114 km distance) agrees with the previously mentioned vertical fault plane solution (Chapter I) of Bérubé (1985). Hypocentral locations of microearthquakes (Hyndman and Ellis, 1981) require a westward dip of 80° on the inner fault, consistent with the velocity model. The remaining major fault is the Rennell-Louscoone Fault at 172 km model distance on Moresby Island. Sutherland

Brown (1968) observed dips ranging from 75° northeastwards to vertical on the associated fault strands. This suggests a tensional mechanism. The rotation and shifting of the Queen Charlotte Islands along this fault zone during the initiation of spreading in Queen Charlotte Sound (Chapter I) would have produced the necessary tensional regime. The ongoing vertical uplift of the western edge of the islands by lithospheric flexure (Riddihough, 1982a) may produce additional vertical offset on this fault in future.

Two tectonic mechanisms will be examined to explain the observed terrace structure: accretion associated with active subduction, and structural compression associated with convergence at a transform fault. The sharp increase in model Moho dip from 2.3° west of the terrace to 19° beneath the terrace is supportive of subduction of the Pacific plate beneath the Queen Charlotte Islands. Similar values were obtained from refraction studies for southern Moresby Island (a poorly constrained 20° - Horn et al., 1984) and for the Juan de Fuca Plate beneath Vancouver Island (14–16° - Spence et al., 1985). A lower value of 5° (Mackie, 1985) for the Queen Charlotte Islands region implies that Moho dip decreases beneath the islands but is still consistent with subduction processes (see also discussion in section 5.9).

The slow rate of convergence across the plate margin (10 to 20 mm/a) may cause weak coupling between the subducting Pacific plate and the America plate. The expected tectonic processes for such a case are: (1) accretion by deposition of sediment and subsequent tectonic incorporation into an accretionary complex; (2) sediment subduction of material ponded in a trench axis; and (3) erosion by failure of the margin front through mass wasting and subsequent incorporation into subducting sediment (von Huene, 1984).

Trench sediments seen in CSP profiles (eg. Chase and Tiffin, 1972; Chase et al., 1975) are relatively undisturbed except for minor faulting so it is unlikely that process (2) is occurring on a large scale. However, tectonic erosion of the margin has almost certainly occurred. Strike–slip faulting, an important erosion process in zones of oblique compressional stress (von Huene, 1984), appears to have removed some continental material as evidenced by the truncated spurs and triangular seaward–facing facets of the coastal mountains on the Queen Charlotte Islands (Keen and Hyndman, 1979).

Sedimentary accretion of material from the subducting ocean crust to the front of the margin could have produced the complex structure of the upper terrace. Seismic records across the landward slope of the eastern Aleutian Trench (von Huene, 1984) reveal the presence of 3 km thick blocks of sediment, separated by steep high angle thrust faults, beneath younger sediments at the continental margin (figure 39). The lower sediments may be subducting with the oceanic crust. Accreted sediments and possibly imbricated oceanic crust were imaged beneath southern Vancouver Island by high density seismic reflection profiling. Similar structures may compose the upper Queen Charlotte terrace.

The interpretation of the upper terrace as an accretionary sediment wedge would of course require the presence of subducting oceanic crust beneath it. No internal reflections from within the lower terrace were detected, providing no support for a structural division. It is quite possible, however, that the top of the subducting crust is extremely irregular as a result of strike–slip faulting and convergence in the terrace region. Strong reflections would not be generated in such a case and any energy would be severely attenuated by the deformed overlying sediments. The velocity structure of the ocean crust could then have been amalgamated with the overlying terrace structure to produce the single "averaged" velocity unit of the model.

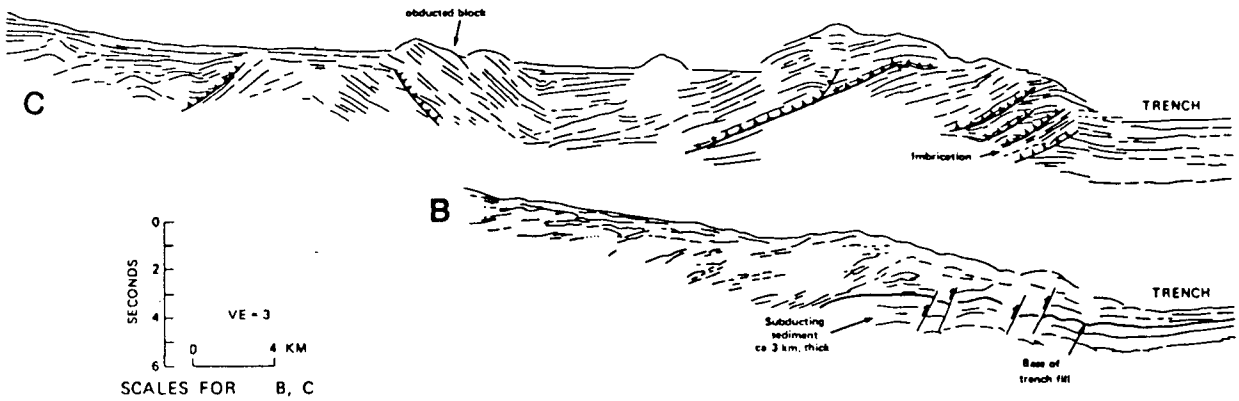


**Figure 39.** Seismic profiles across the Aleutian Trench, illustrating the structures that result from obduction, imbrication, accretion, and subduction of sediments at a convergent margin (after von Huene, 1984).

Alternatively, the complex structure of the terrace may result from compression associated with oblique convergence at the fault zone. Hyndman and Ellis (1981) proposed a model in which faulting occurs on the Queen Charlotte strike-slip fault with the shallow portion of the thrust zone locked. Convergence is taken up either by periodically unlocking the upper portion of the thrust or by compressively deforming and shortening the whole oceanic lithosphere beneath the terrace. Hyndman et al. (1982) extended the transcurrent fault into the underlying oceanic lithosphere to be consistent with the microseismicity observed primarily between 10 and 25 km depth. They suggested that the faulting must jump seaward at intervals to remain beneath the edge of the continental crust — terrace sediment contact (figure 40). Both models require a sharp downward bend of the oceanic lithosphere beneath the margin, possibly with associated normal faulting at the outer edge of the terrace.

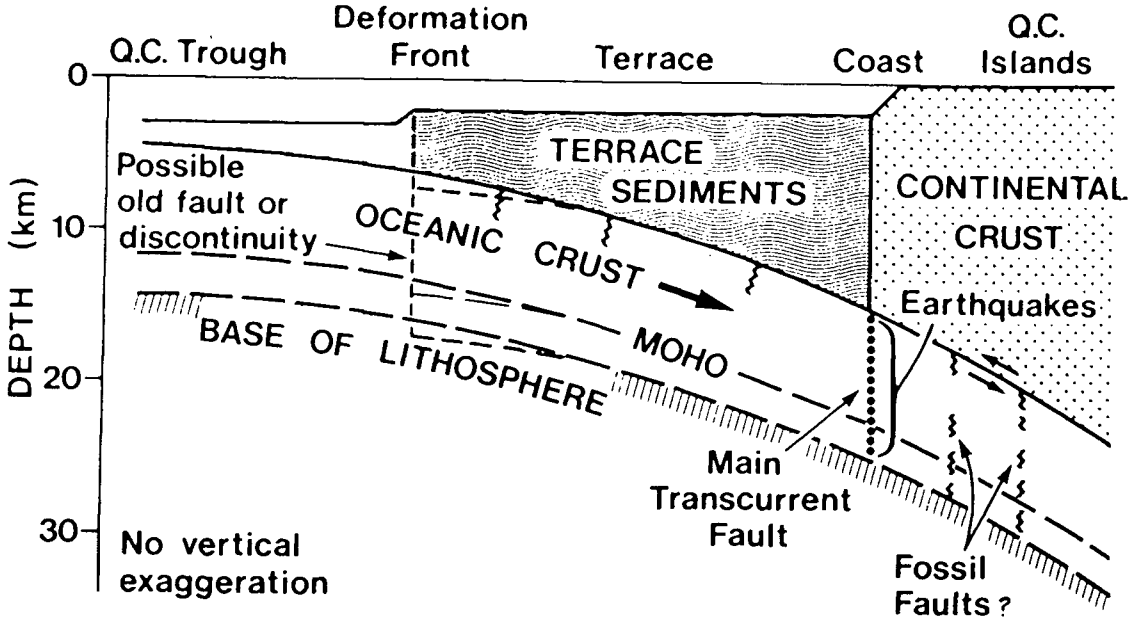


**Figure 40.** A possible tectonic model of the Queen Charlotte Fault zone. Oblique convergence is resolved into strike-slip motion on the fault parallel to the margin and a small component of underthrusting perpendicular to the margin (Hyndman et al., 1982).

Numerous earthquakes recorded in the recent microseismicity study of Bérubé (1985) were located in the Queen Charlotte fault zone along Moresby Island; a few were located on the terrace and outer fault scarp. The focal depths of the events extend to 25 km although most of the activity was well constrained to depths of less than 15 km. Thus, seismic activity at depths greater than 13 km would be located within oceanic crust if subducted crust is assumed to underlie the terrace in the velocity structural model of figure 24. The Queen Charlotte fault would thus have to extend into the oceanic crust, as Hyndman et al. (1982) suggested, and essentially "slice" it as transform motion occurs. The slicing would have to be discontinuous, perhaps by alternating transform

motion and subduction, to allow the continued movement of the oceanic material across the fault zone and beneath the continental lithosphere.

Lowell (1972) modelled strike-slip movement with a small component of convergence across the fault zone using a clay cake on moving sheets of tin. The relative motion vector of the model was oriented at 15° to the fault trace, similar to the Queen Charlotte region. The material at the fault zone moved upwards to produce a welt with downward tapering wedges and upthrust margins (figure 41). The steep faults modelled for the terrace region may be upthrust faults formed in a similar manner as opposed to underthrusts formed by accretion.

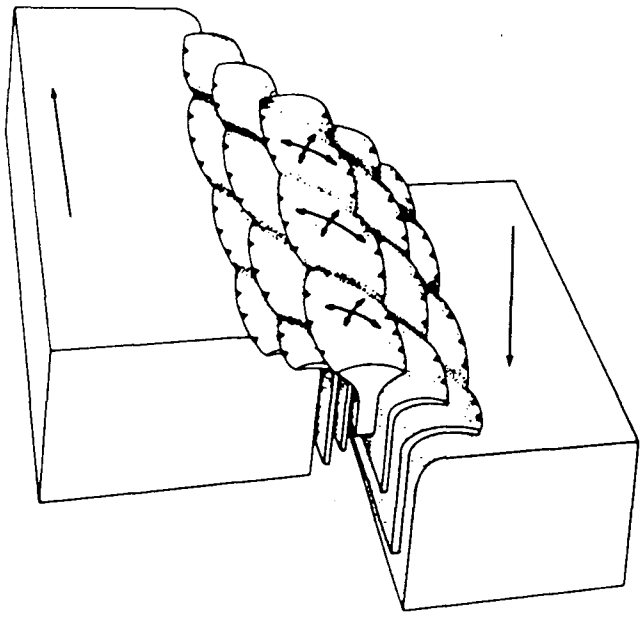

**Figure 41.** Conceptual diagram of an upthrust-bounded welt created by convergent strike-slip or transform motion. The welt has downward-tapering wedges and upthrust margins (Lowell, 1972).

Thrust mechanisms and near-vertical faulting were computed by Bérubé (1985) for two earthquake clusters at 12 and 9 km depth respectively on the Queen Charlotte Fault zone near the present refraction study area. The shallow focal depths and the clay cake models suggest that thrusting of terrace material above any subducting oceanic crust is occurring as a result of compression in the fault zone.

The structure of the terrace can thus be attributed to two different tectonic processes which may occur concurrently or alternate as necessary as shown in figure 42a. Convergent motion may be accommodated by slow, shallow subduction of the oceanic lithosphere beneath the Queen Charlotte Islands. Sediment overlying the oceanic crust would be accreted to the seaward edge of the terrace and/or subducted beneath the terrace. Transform motion is occurring as dextral strike-slip on the Queen Charlotte fault and possibly on associated faults on the Queen Charlotte Islands and beneath Hecate Strait. Sedimentary and upper crustal material may be thrusting upwards in the terrace (figure 42b) as subduction is halted at the fault and compression needs to be accommodated. The compressive stress in the lower oceanic lithosphere would continue to build during this phase and may force the resumption of subduction and the subsequent migration of faulting in the downgoing crust.

The refraction model developed in this study supports recent subduction but suggests that compression and upthrusting of terrace material presently account for a major part of the component of convergence at the active Queen Charlotte fault zone.

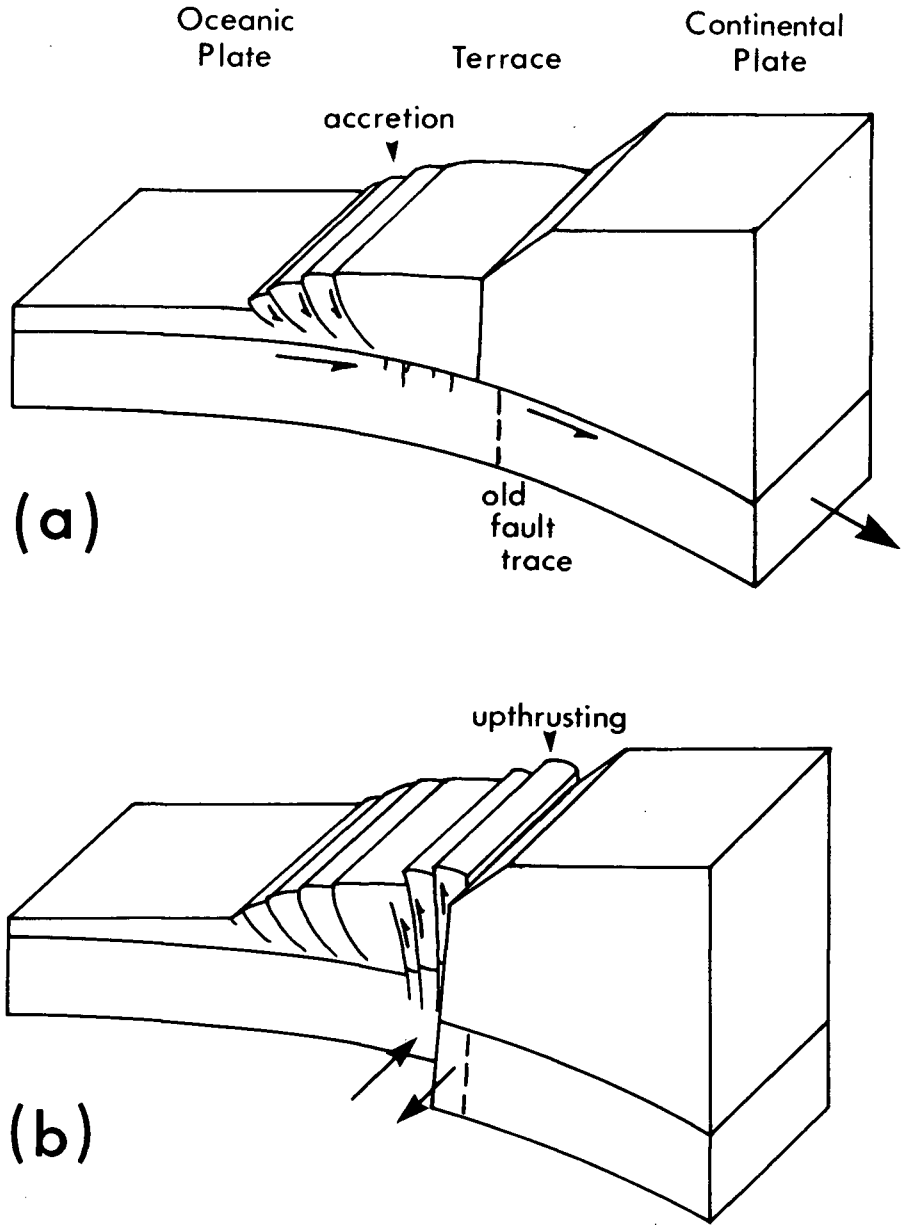


**Figure 42.** Proposed tectonic processes in the Queen Charlotte Fault region. (a) subduction - sediments and upper crust deform by accretion and compression as subduction occurs. (b) transform motion - compression in sediments and crust relieved by upthrusting along the fault zone.

## 6.3 Conclusions

The structural model developed for the Queen Charlotte Fault zone confirms an anomalous low velocity terrace region separating oceanic crust to the west and continental crust to the east. The terrace crustal structure consists of a 3 km thick upper unit with velocity 3.8 km/s at the top and fairly high (0.35 km/s/km) gradient, and a lower unit with an average thickness of 10 km, velocity 5.3 km/s, and gradient 0.20 km/s/km. The terrace is bounded on the west by an old fault zone and on the east by the currently active near-vertical Queen Charlotte Fault; steep faulting also extends through at least the upper crustal unit of the terrace. Moho dip steepens considerably beneath the terrace from 5° to 19°.

The structural complexity of the terrace may result from a combination of accretion and deformation by underthrusting associated with subduction, and compression and upthrusting related to oblique convergence at the transform fault. Additional study is necessary to provide the structural resolution required to distinguish between the two. High resolution multichannel seismic reflection profiling over the terrace would better define the velocities and fault orientations and possibly locate the top of subducted oceanic lithosphere.

Similarly, further sampling is necessary to constrain the vertical offset of 1.1 km modelled on the Rennell-Louscoone Fault. Reversed refraction profiles across and along the islands would provide information presently lacking about regional crustal structure and would better constrain Moho depth and dip.

The addition of such future observations to the existing geophysical and geological information will further the understanding of the complicated tectonics and complex structure of the Queen Charlotte Fault zone region.

## BIBLIOGRAPHY


Atwater, T., 1970, Implications of plate tectonics for the Cenozoic tectonic evolution of western North America: Geol. Soc. Am. Bull., **81**, 3513–3536.

Bérubé, J., 1985, A seismicity study of the Queen Charlotte Islands/Hecate Strait region: M.Sc. thesis, Univ. of British Columbia, Vancouver, 100 pp.

Bird, D.N., 1981, Time–term analysis using linear programming and its application to refraction data from the Queen Charlotte Islands: M.Sc. thesis, Univ. of British Columbia, Vancouver, 79 pp.

Chase, R.L. and Tiffin, D.L., 1972, Queen Charlotte Fault–Zone, British Columbia: Proc. Int. Geol. Congr. 24th, section 8, 17–27.

Chase, R.L., Tiffin, D.L. and Murray, J.W., 1975, The western Canadian continental margin, *in* Yorath, C.J., Parker, E.R. and Glass, D.J., Eds, Canada's continental margins and offshore petroleum exploration: Can. Soc. Petr. Geol., Memoir 4, 701–721.

Christensen, N.I. and Salisbury, M.H., 1975, Structure and constitution of the lower oceanic crust: Rev. Geophys. Space Phys., **13**, 57–86.

Christensen, N.I. and Smewing, J.D., 1981, Geology and seismic structure of the northern section of the Oman ophiolite: J. Geophys. Res., **86**, B4, 2545–2555.

Clowes, R.M., 1984, Acquisition of a crustal refraction profile across the Queen Charlotte Islands and Hecate Strait: Earth Physics Branch Open File Report 84–22, Ottawa, 55 pp.

Clowes, R.M., Brandon, M.T., Green, A.G., Yorath, C.J., Sutherland Brown, A., Kanasewich, E.R. and Spencer, C., 1986, Lithoprobe – southern Vancouver Island: Cenozoic subduction complex imaged by deep seismic reflections: Can. J. Earth Sci. *in press.*

Clowes, R.M. and Knize, S., 1979, Crustal structure from a marine seismic survey off the west coast of Canada: Can. J. Earth Sci., **16**, 1265–1280.

Coney, P.J., 1970, The geotectonic cycle and the new global tectonics: Geol. Soc. Am. Bull., **81**, 739–748.

Coney, P.J., Jones, D.L. and Monger, J.W.H., 1980, Cordilleran suspect terranes: Nature, 288, 329–333.

Couch, R.W., 1969, Gravity and structures of the crust and subcrust in the southeast Pacific Ocean west of Washington and British Columbia: Ph.D. thesis, Oregon State Univ., Corvallis.

Currie, R.G., Stevens, L.E., Tiffin, D.L. and Riddihough, R.P., 1980, Marine geophysical survey of the Queen Charlotte Islands (abstr.): Trans. Am. Geophys. Union (EOS), **61**, 71.

Davis, E.E. and Seemann, D.A., 1981, Compilation of seismic reflection profiles across the continental margin of western Canada: Geol. Surv. Canada Open File Report 751.

Dehlinger, P., Couch, R.W., McManus, D.A. and Gemperle, M., 1970, Northeast Pacific structure *in* Maxwell, A.E., Ed., The sea, vol. IV, part II: Wiley-Interscience Publ., New York, 133–190.

Heffler, D.E. and Barret, D.L., 1979, OBS development at Bedford Institute of Oceanography: Mar. Geophys. Res., **4**, 227–245.

Hilde, T.W.C., Uyeda, S. and Kroenke, L., 1977, Evolution of the western Pacific and its margin: Tectonophysics, **38**, 145–165.

Horn J.R., 1982, A snapshot of the Queen Charlotte Fault zone obtained from P-wave refraction data: M.Sc. thesis, Univ. of British Columbia, Vancouver, 79pp.

Horn J.R., Clowes, R.M., Ellis, R.M. and Bird, D.N., 1984, The seismic structure across an active oceanic/continental transform fault zone: J. Geophys. Res., **89**, B5, 3107–3120.

Hyndman, R.D. and Ellis, R.M., 1981, Queen Charlotte fault zone: microearthquakes from a temporary array of land stations and ocean bottom seismographs: Can. J. Earth Sci., **18**, 776–788.

Hyndman, R.D., Lewis, T.J., Wright, J.A., Burgess, M., Chapman, D.S. and Yamano, M., 1982, Queen Charlotte fault zone: heat flow measurements: Can. J. Earth Sci., **19**, 1657–1669.

Hyndman, R.D., Riddihough, R.P. and Herzer, R., 1979, The Nootka fault zone – a new plate boundary off western Canada: Geophys. J. Roy. Astr. Soc., **58**, 667–683.

Hyndman, R.D. and Weichert, D.H., 1983, Seismicity and rates of relative motion on the plate boundaries of western North America: Geophys. J. Roy. Astr. Soc., **72**, 59–82.

Irving, E., 1979, Paleopoles and paleolatitudes of North America and speculations about displaced terrains: Can. J. Earth Sci., **16**, 669–694.

Keen, C.E. and Hyndman, R.D., 1979, Geophysical review of the continental margins of eastern and western Canada: Can. J. Earth Sci., **16**, 712–747.

Kirstiuk, S., 1981, A preliminary investigation into the structure of the upper crust in the terrace region of the Queen Charlotte fault zone: B.Sc. thesis, Univ. of British Columbia, Vancouver, 77 pp.

Lowell, J.D., 1972, Spitsbergen Tertiary orogenic belt and the Spitsbergen fracture zone: Geol. Soc. Am. Bull., **83**, 3091–3102.

Mackie, D., 1985, Subduction beneath the Queen Charlotte Islands? Results of a seismic refraction survey: M.Sc. thesis, Univ. of British Columbia, Vancouver, 130 pp.

Minster, J.B. and Jordan, T.H., 1978, Present day plate motions: J. Geophys. Res., **83**, 5331–5354.

O'Brien, P.N.S., 1960, Seismic energy from explosions: Geophys. J., **3**, 29–44.

Riddihough, R.P., 1977, A model for recent plate interactions off Canada's west coast: Can. J. Earth Sci., **14**, 384–396.

Riddihough, R.P., 1982a, Contemporary movements and tectonics on Canada's west coast: a discussion: Tectonophysics, **86**, 319–341.

Riddihough, R.P., 1982b, One hundred years of plate tectonics in Western Canada: Geoscience Canada, **9**, 28–34.

Riddihough, R.P., Currie, R.G., and Hyndman, R.D., 1980, The Dellwood knolls and their role in triple junction tectonics off northern Vancouver Island: Can. J. Earth Sci., **17**, 577–593.

Rogers, G.C., 1983, Seismotectonics of British Columbia: Ph.D. thesis, Univ. of British Columbia, Vancouver, 247 pp.

Sheriff, R.E. and Geldart, L.P., 1982, Exploration seismology, vol. I: Cambridge Univ. Press, Cambridge, 253 pp.

Snavely, P.D., Wagner, H.C., Tompkins, D.H. and Tiffin, D.L., 1981, Preliminary geologic interpretation of a seismic reflection profile across the Queen Charlotte Island fault system off Dixon Entrance, Canada - United States: U.S. Geol. Surv. Open File Report 81–299.

Spence, G.D., 1984, Seismic structure across the active subduction zone of western Canada: Ph.D. thesis, Univ. of British Columbia, Vancouver, 191 pp.

Spence, G.D., Clowes, R.M. and Ellis, R.M., 1985, Seismic structure across the active subduction zone of western Canada: J. Geophys. Res., **90**, B8, 6754–6772.

Spence, G.D., Whittall, K.P. and Clowes, R.M., 1984, Practical synthetic seismograms for laterally varying media calculated by asymptotic ray theory: Bull. Seism. Soc. Am., **74**, no. 4, 1209–1223.

Srivastava, S.P., 1973, Interpretation of gravity and magnetic measurements across the continental margin of British Columbia, Canada: Can. J. Earth Sci., **10**, 1664–1667.

Stone, D.B., 1977, Plate tectonics, paleomagnetism, and the tectonic history of the N.E. Pacific: Geophysical Surveys, **3**, 3–37.

Strutt, J.W., 1917, On the pressure developed in a liquid during the collapse of a spherical cavity: Philosophical Mag., **34**, 94–98.

Sutherland Brown, A., 1968, Geology of the Queen Charlotte Islands: Brit. Col. Dept. of Mines and Petr. Res., Bulletin 54, 226 pp.

Tjaden, G., 1981, Seismic modelling of refraction data from the shelf off the Queen Charlotte Islands: B.Sc. thesis, Univ. of British Columbia, Vancouver, 50pp.

van der Voo, R., Jones, M., Gromme, C.S., Iberlein, G.D. and Chuckin, M., 1980, Paleozoic paleomagnetism and northward drift of the Alexander terrane, southeastern Alaska: J. Geophys. Res., **85**, 5281–5296.

von Huene, R., 1984, Tectonic processes along the front of modern convergent margins — Research of the past decade: Ann. Rev. Earth Planet. Sci., **12**, 359–381.

Whittall, K.P. and Clowes, R.M., 1979, A simple simple, efficient method for the calculation of traveltimes and ray paths in laterally inhomogeneous media: J. Can. Soc. Explor. Geophys., **15**, 21–29.

Willis, H.F., 1941, Underwater explosions, time interval between successive explosions: British Report WA-47-21.

Yorath, C.J. and Cameron, B.E.B., 1982, Oil on the West Coast?: GEOS, **11**, 13–15.

Yorath, C.J. and Chase, R.L., 1981, Tectonic history of the Queen Charlotte Islands and adjacent areas - a model: Can. J. Earth Sci., **18**, 1717–1739.

Yorath, C.J. and Hyndman, R.D., 1983, Subsidence and thermal history of Queen Charlotte Basin: Can. J. Earth Sci., **20**, 135–159.

Young, I.F., 1981, Geological development of the western margin of the Queen Charlotte basin: M.Sc. thesis, Univ. of British Columbia, Vancouver, 380 pp.

# APPENDIX A

Airgun data.

Vertical component data sections for airgun line AG2. Distance scales match the distances used in the modelling; shot-receiver distances are also indicated. Spreading corrections have been applied to the data; relative trace amplitudes are otherwise preserved (refer to chapter II).

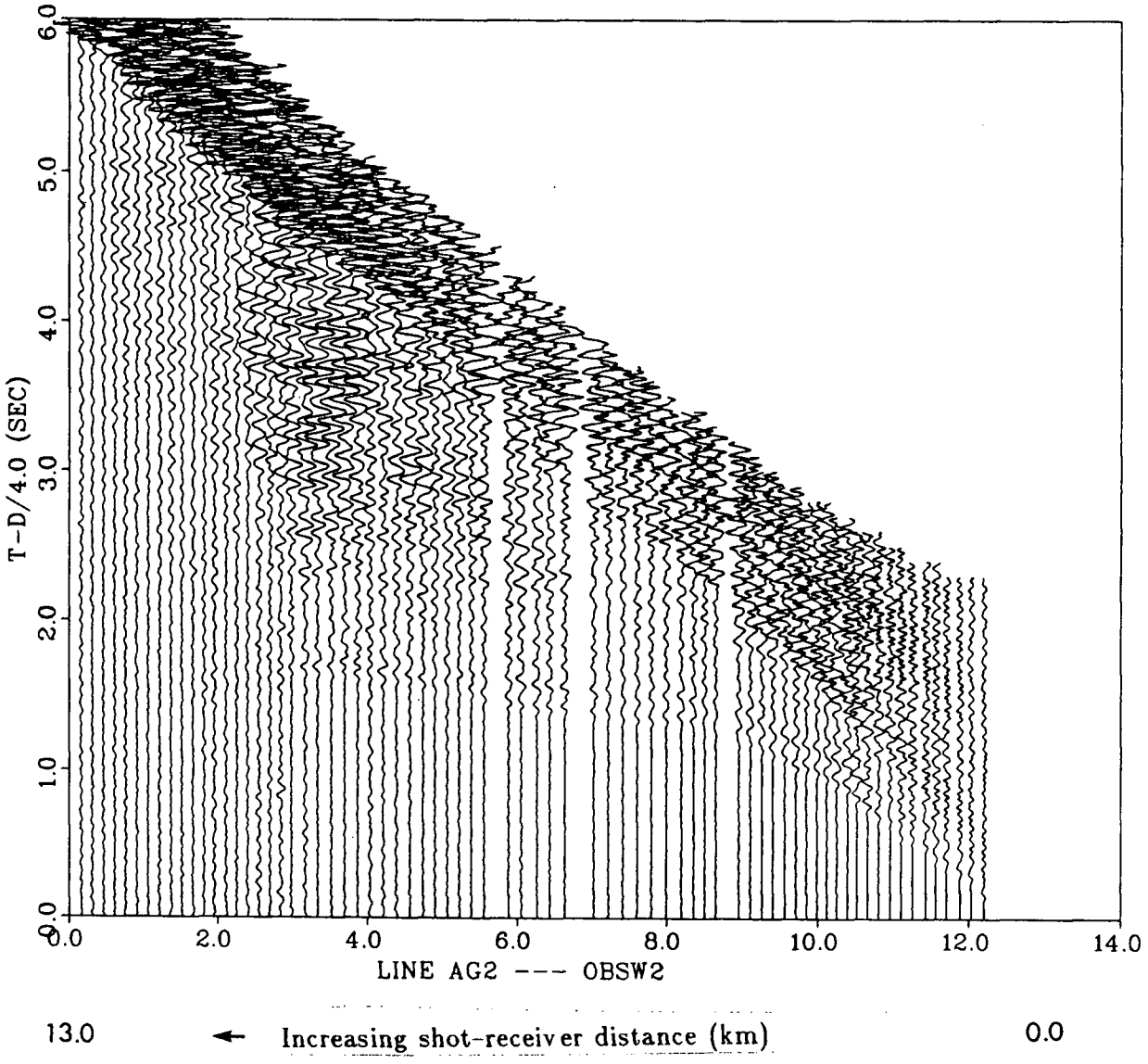
T-D/4.0 (SEC)
0.0
1.0
2.0
3.0
4.0
5.0
6.0
0.0
2.0
4.0
6.0
8.0
10.0
12.0
14.0
LINE AG2 --- OBSW2
13.0
Increasing shot-receiver distance (km)
0.0

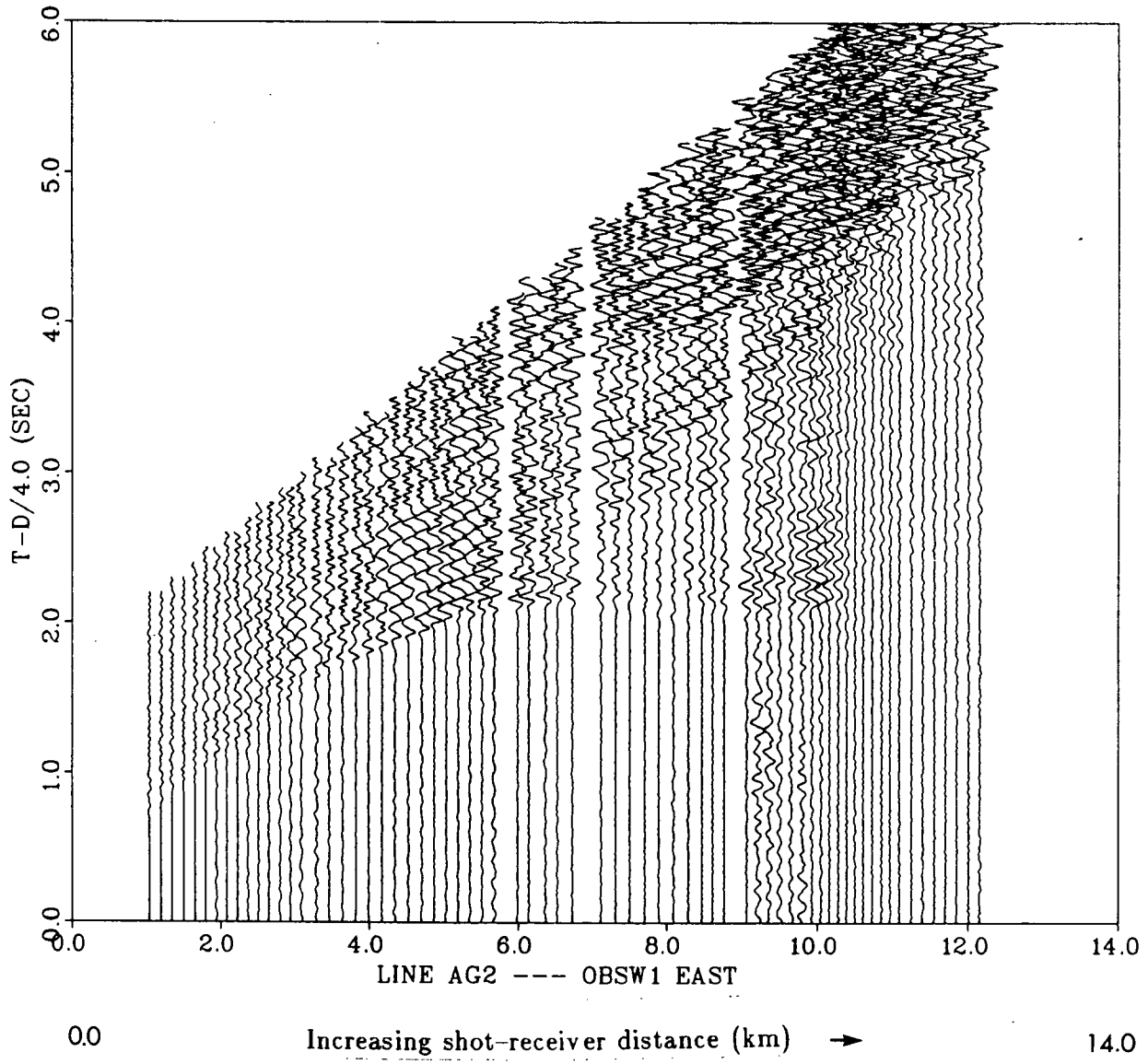
T-D/4.0 (SEC)
0.0
1.0
2.0
3.0
4.0
5.0
6.0
0.0
2.0
4.0
6.0
8.0
10.0
12.0
14.0
LINE AG2 --- OBSW1 EAST
0.0
Increasing shot-receiver distance (km) →
14.0

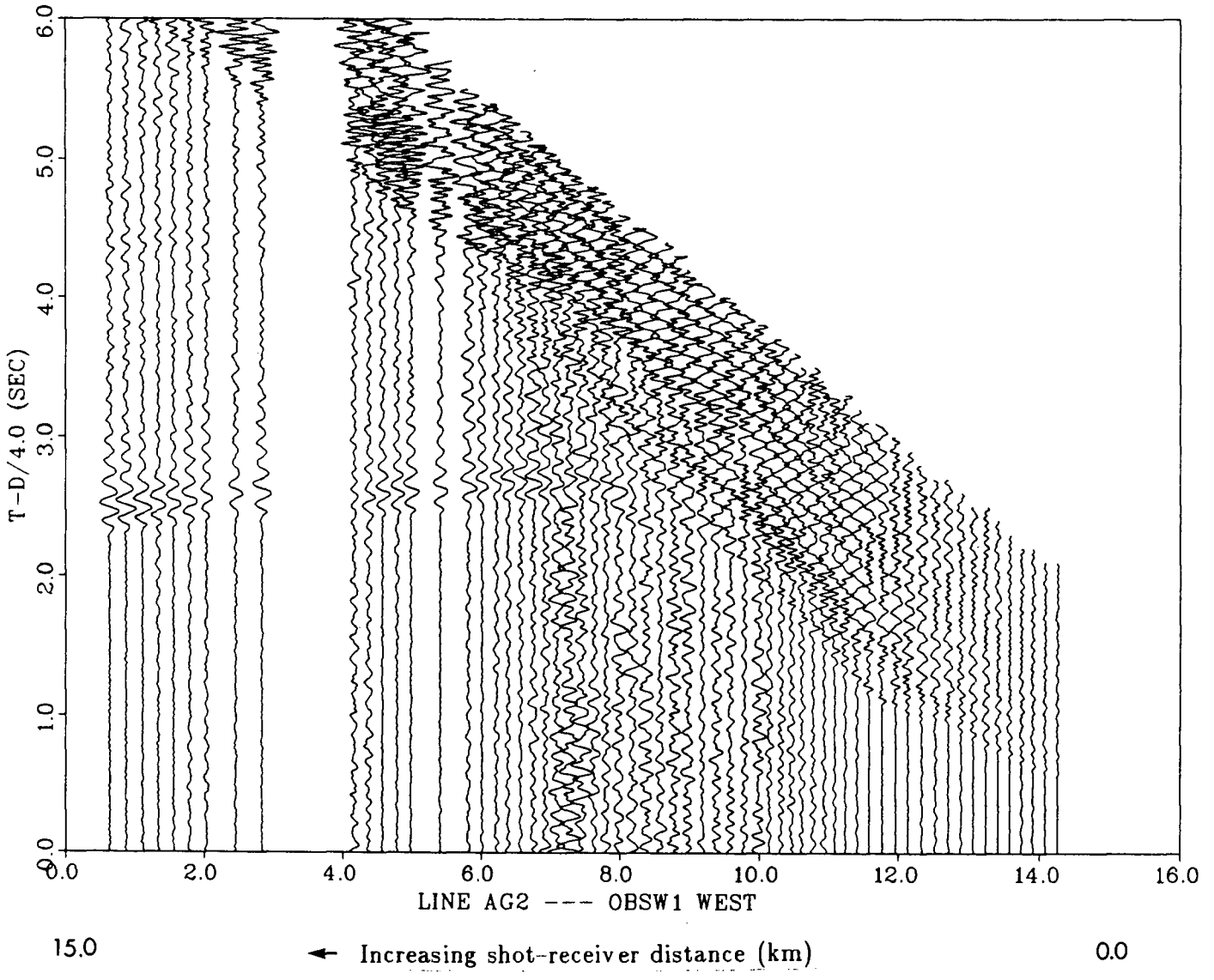
T-D/4.0 (SEC)
0.0
1.0
2.0
3.0
4.0
5.0
6.0
0.0
2.0
4.0
6.0
8.0
10.0
12.0
14.0
16.0
LINE AG2 --- OBSW1 WEST
15.0
← Increasing shot-receiver distance (km)
0.0

# APPENDIX B

Explosion data.

Vertical component data sections for explosion line EX1. Filtering parameters are given with each section. Shot numbers are the central 3 digits of the 5-digit code number plotted with each trace. Distance scales are model distances; shot-receiver distances are also indicated. Spherical spreading corrections and charge size compensations have been applied to the data as described in chapter II. The data plots show relative trace amplitudes after application of these corrections.

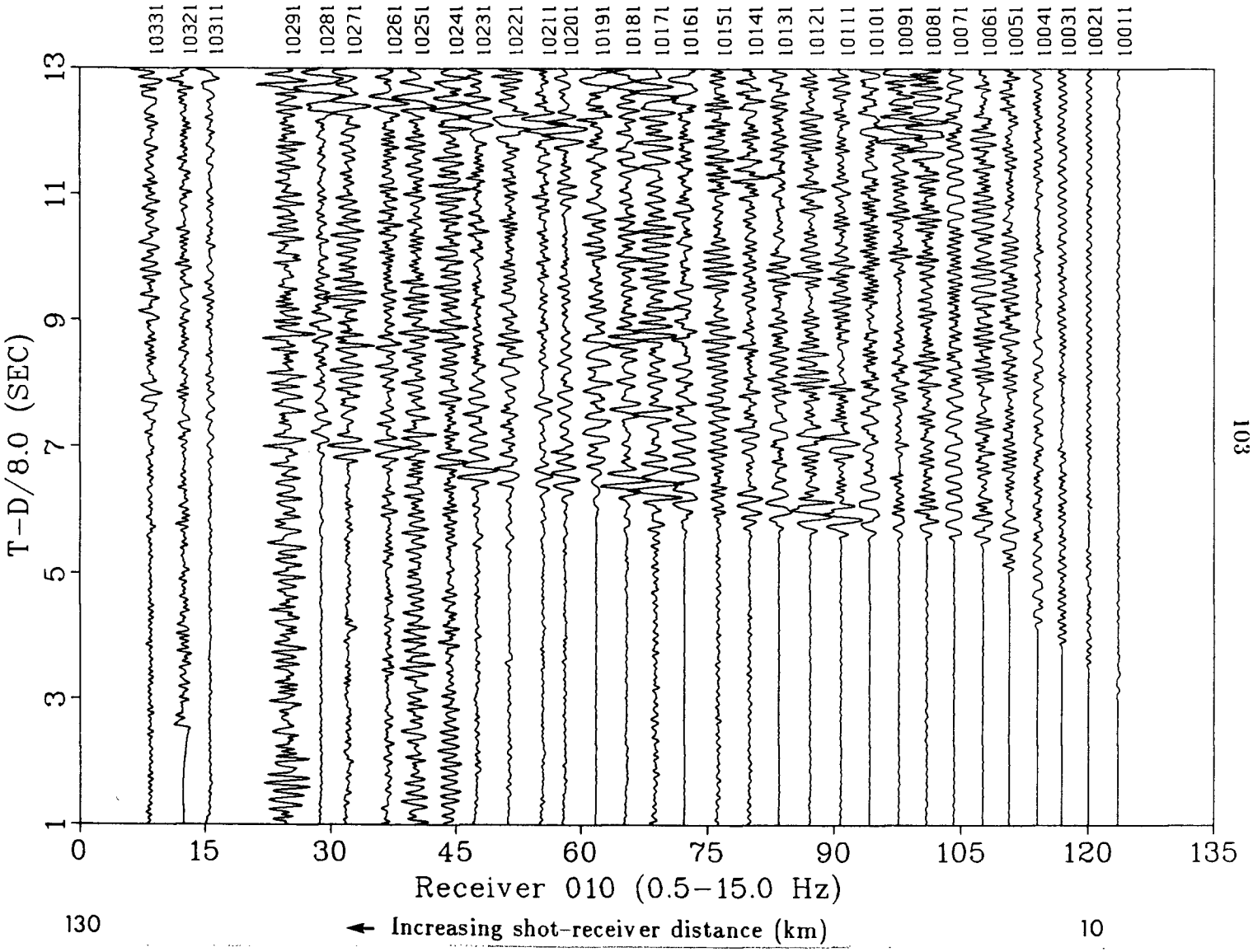
1033I
1032I
1031I
1029I
1028I
1027I
1026I
1025I
1024I
1023I
1022I
1021I
1020I
1019I
1018I
1017I
1016I
1015I
1014I
1013I
1012I
1011I
1010I
1009I
1008I
1007I
1006I
1005I
1004I
1003I
1002I
1001I
T-D/8.0 (SEC)
1
3
5
7
9
11
13
0
15
30
45
60
75
90
105
120
135
Receiver 010 (0.5-15.0 Hz)
130
← Increasing shot-receiver distance (km)
10

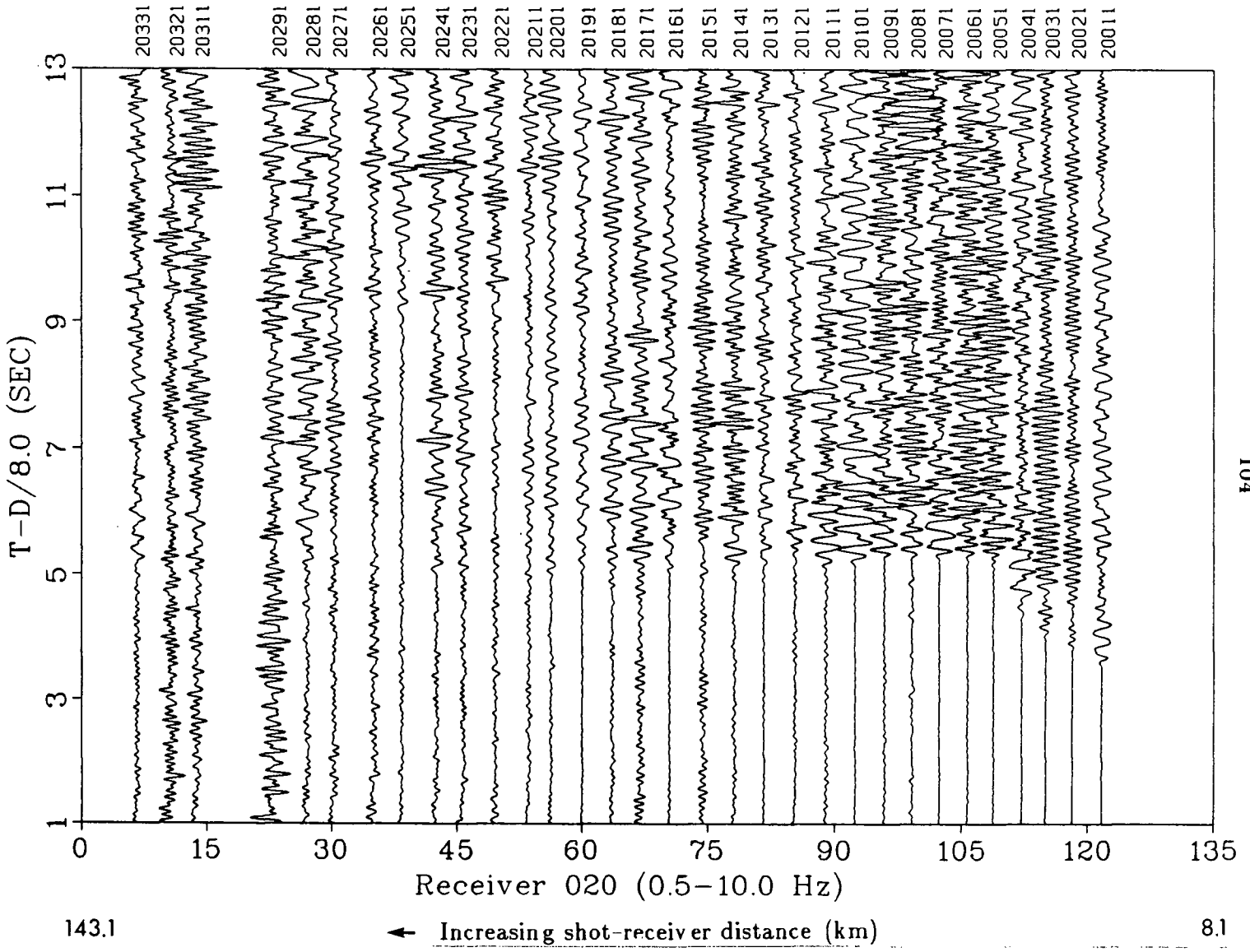
20331
20321
20311
20291
20281
20271
20261
20251
20241
20231
20221
20211
20201
20191
20181
20171
20161
20151
20141
20131
20121
20111
20101
20091
20081
20071
20061
20051
20041
20031
20021
20011
T-D/8.0 (SEC)
1
3
5
7
9
11
13
0
15
30
45
60
75
90
105
120
135
Receiver 020 (0.5-10.0 Hz)
143.1
← Increasing shot-receiver distance (km)
8.1

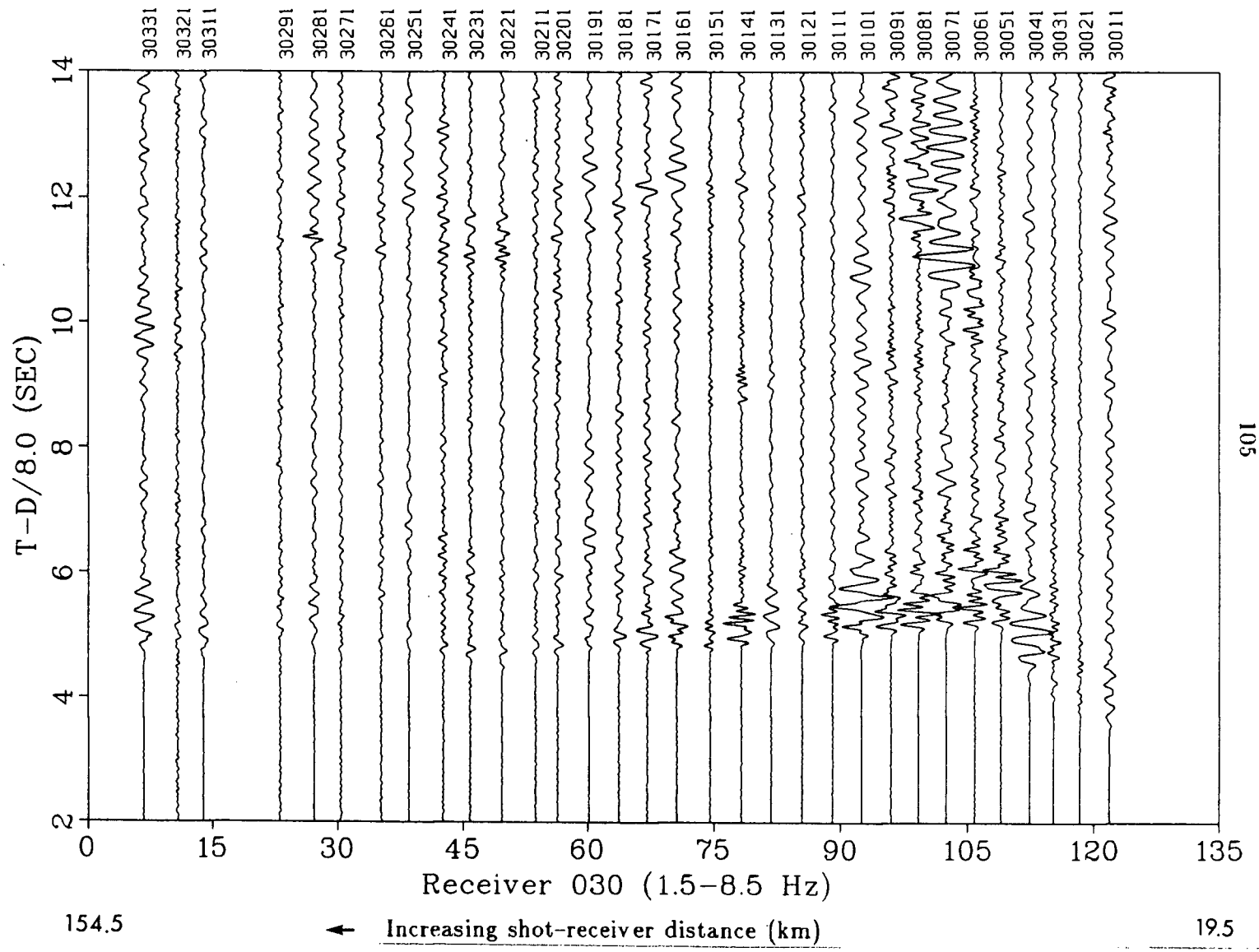
30331
30321
30311
30291
30281
30271
30261
30251
30241
30231
30221
30211
30201
30191
30181
30171
30161
30151
30141
30131
30121
30111
30101
30091
30081
30071
30061
30051
30041
30031
30021
30011
T-D/8.0 (SEC)
2
4
6
8
10
12
14
0
15
30
45
60
75
90
105
120
135
Receiver 030 (1.5-8.5 Hz)
154.5
Increasing shot-receiver distance (km)
19.5

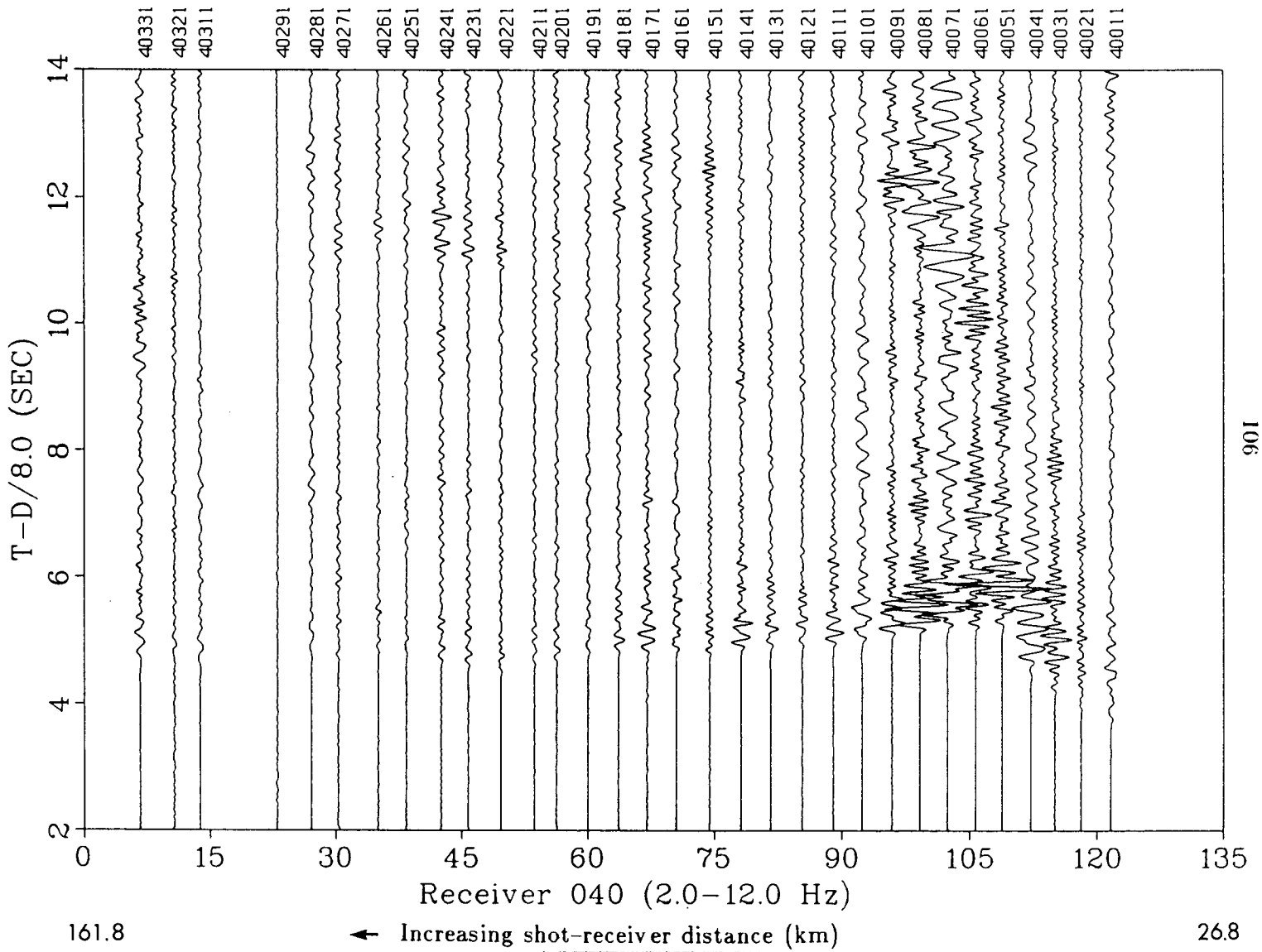
40331
40321
40311
40291
40281
40271
40261
40251
40241
40231
40221
40211
40201
40191
40181
40171
40161
40151
40141
40131
40121
40111
40101
40091
40081
40071
40061
40051
40041
40031
40021
40011
T-D/8.0 (SEC)
2
4
6
8
10
12
14
0
15
30
45
60
75
90
105
120
135
Receiver 040 (2.0-12.0 Hz)
161.8
← Increasing shot-receiver distance (km)
26.8

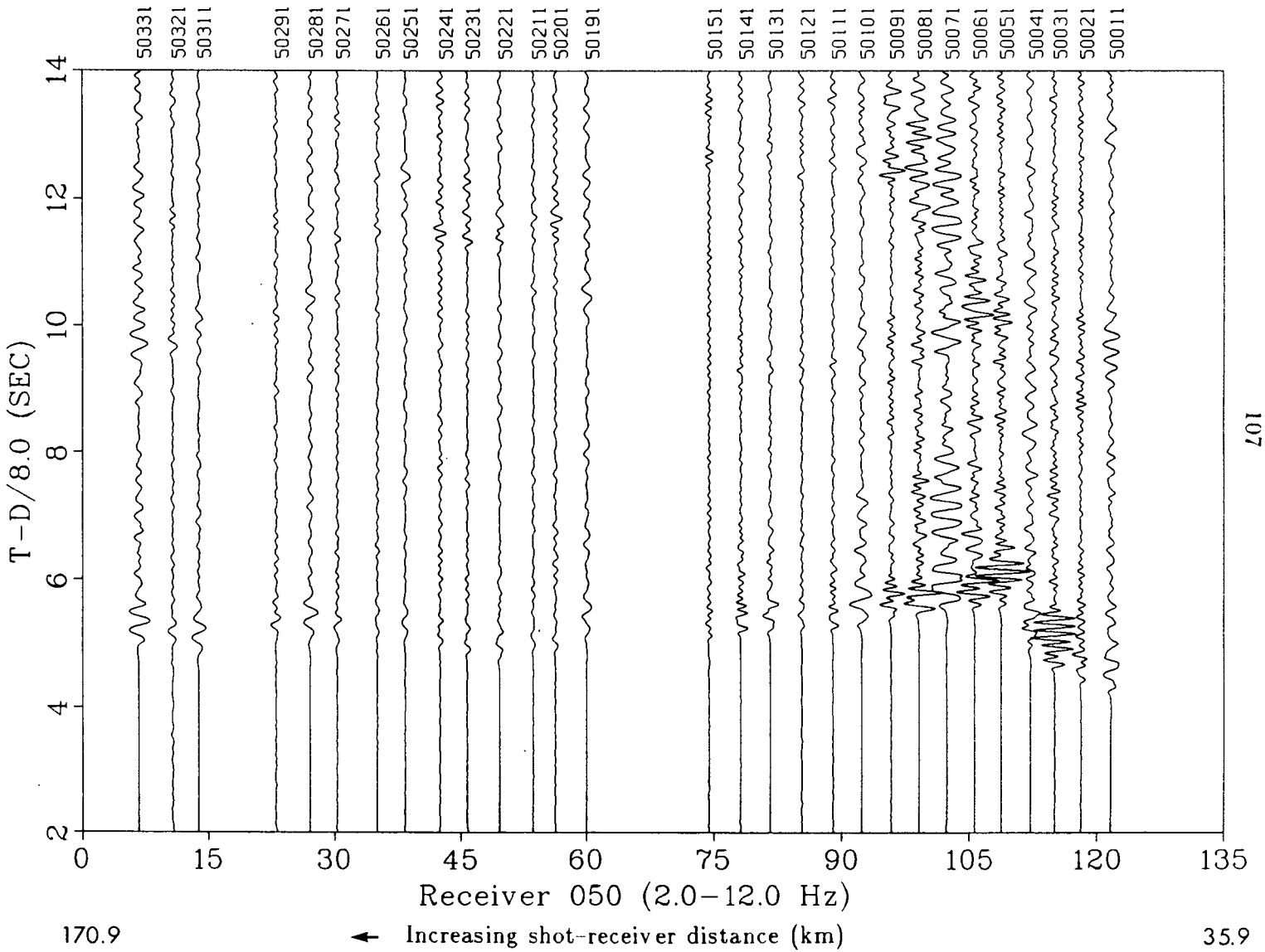
50331
50321
50311
50291
50281
50271
50261
50251
50241
50231
50221
50211
50201
50191
50151
50141
50131
50121
50111
50101
50091
50081
50071
50061
50051
50041
50031
50021
50011
T-D/8.0 (SEC)
2
4
6
8
10
12
14
0
15
30
45
60
75
90
105
120
135
Receiver 050 (2.0-12.0 Hz)
170.9
Increasing shot-receiver distance (km)
35.9

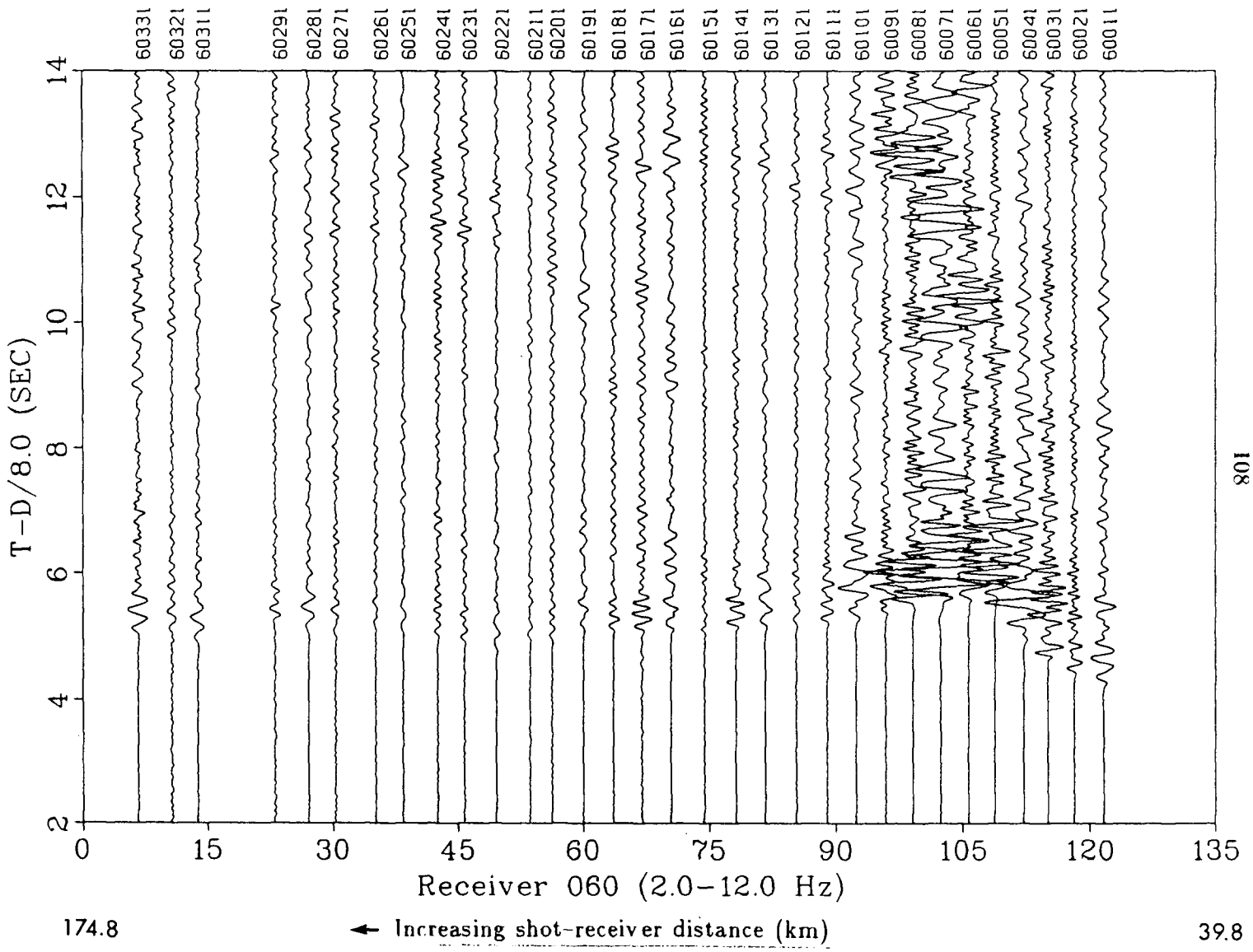
60331
60321
60311
60291
60281
60271
60261
60251
60241
60231
60221
60211
60201
60191
60181
60171
60161
60151
60141
60131
60121
60111
60101
60091
60081
60071
60061
60051
60041
60031
60021
60011
T-D/8.0 (SEC)
2
4
6
8
10
12
14
0
15
30
45
60
75
90
105
120
135
Receiver 060 (2.0-12.0 Hz)
174.8
← Increasing shot-receiver distance (km)
39.8

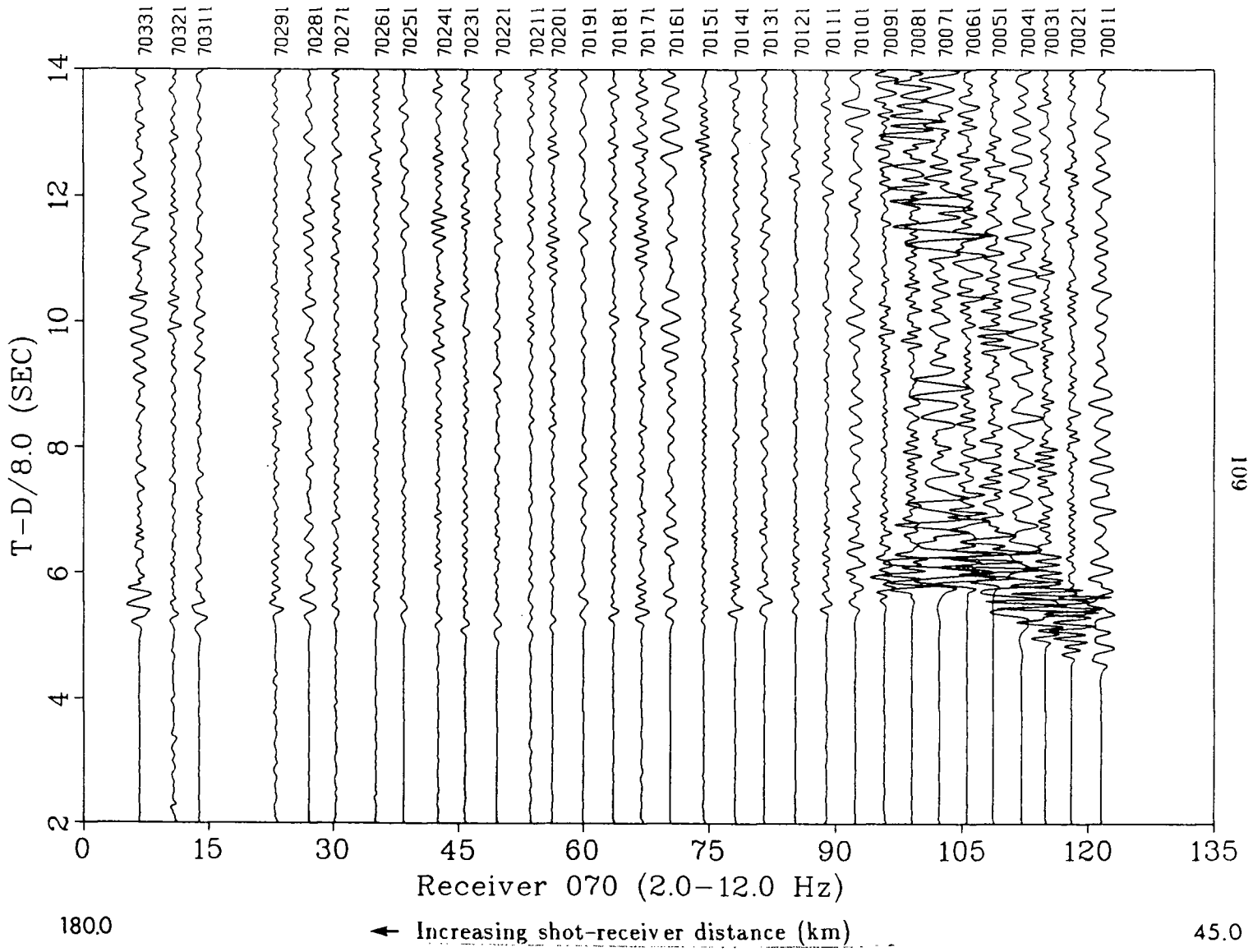
7033I
7032I
7031I
7029I
7028I
7027I
7026I
7025I
7024I
7023I
7022I
7021I
7020I
7019I
7018I
7017I
7016I
7015I
7014I
7013I
7012I
7011I
7010I
7009I
7008I
7007I
7006I
7005I
7004I
7003I
7002I
7001I
T-D/8.0 (SEC)
2
4
6
8
10
12
14
0
15
30
45
60
75
90
105
120
135
Receiver 070 (2.0-12.0 Hz)
180.0
← Increasing shot-receiver distance (km)
45.0

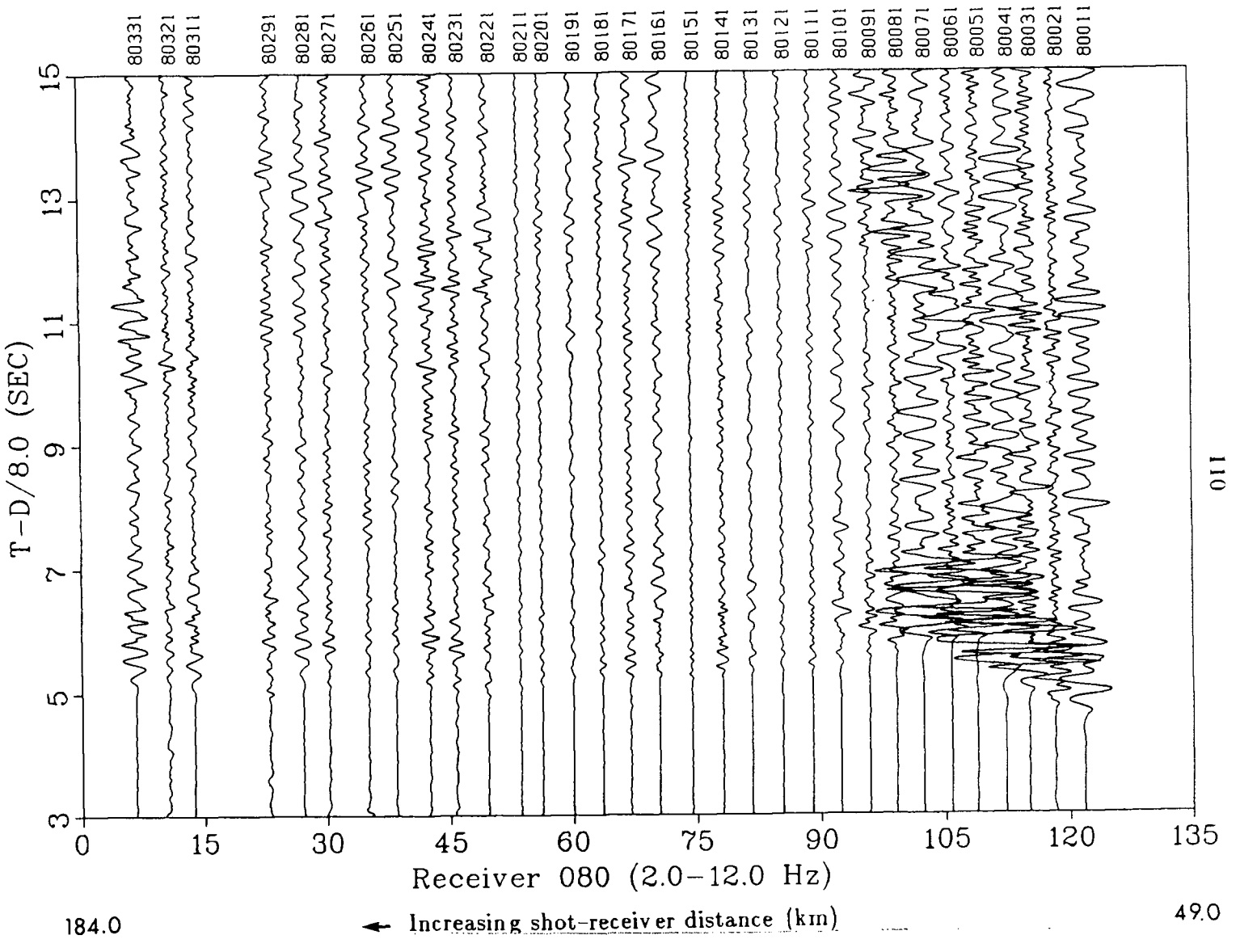
80331
80321
80311
80291
80281
80271
80261
80251
80241
80231
80221
80211
80201
80191
80181
80171
80161
80151
80141
80131
80121
80111
80101
80091
80081
80071
80061
80051
80041
80031
80021
80011
T-D/8.0 (SEC)
3
5
7
9
11
13
15
0
15
30
45
60
75
90
105
120
135
Receiver 080 (2.0-12.0 Hz)
184.0
Increasing shot-receiver distance (km)
49.0

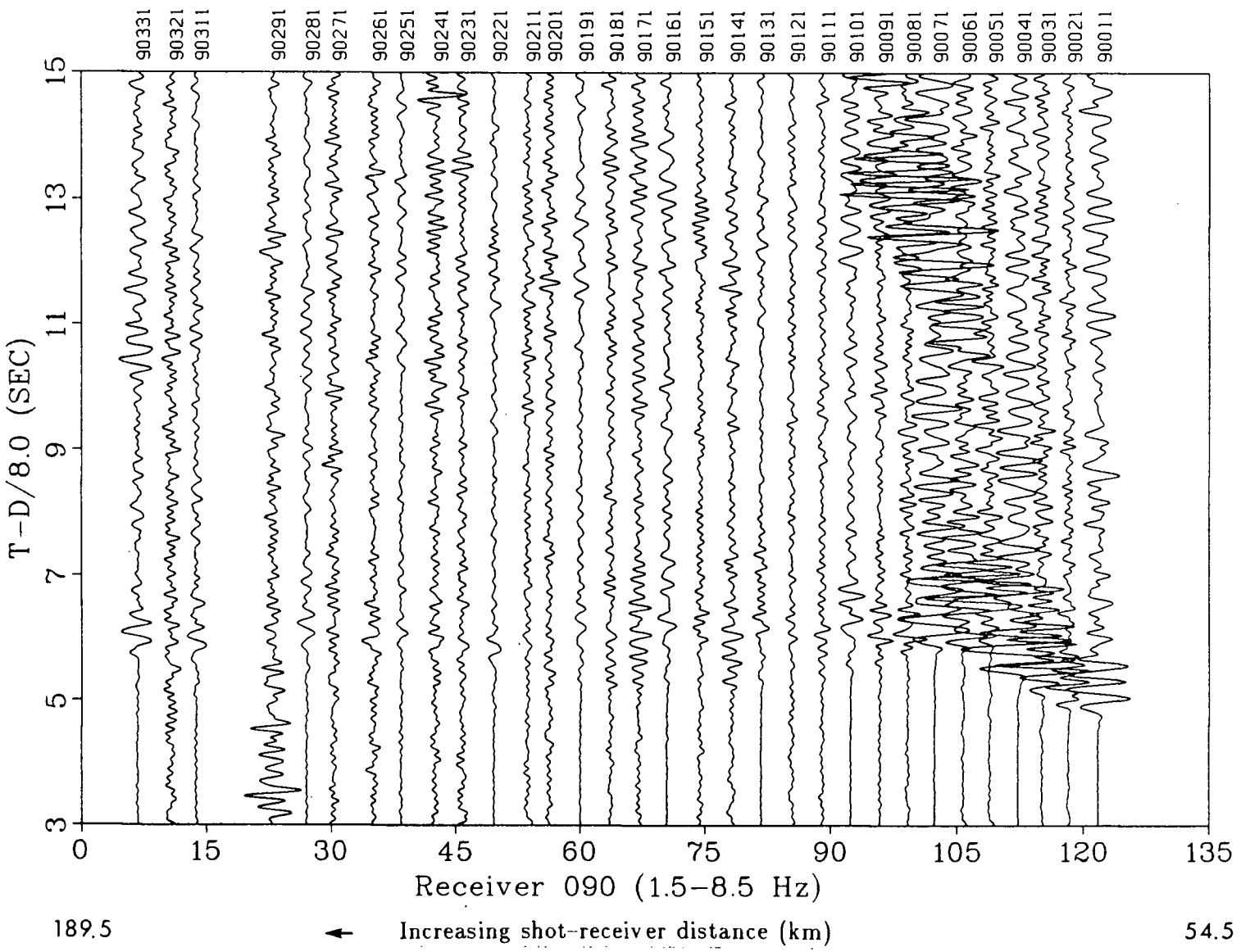
90331
90321
90311
90291
90281
90271
90261
90251
90241
90231
90221
90211
90201
90191
90181
90171
90161
90151
90141
90131
90121
90111
90101
90091
90081
90071
90061
90051
90041
90031
90021
90011
T-D/8.0 (SEC)
3
5
7
9
11
13
15
0
15
30
45
60
75
90
105
120
135
Receiver 090 (1.5-8.5 Hz)
189.5
Increasing shot-receiver distance (km)
54.5

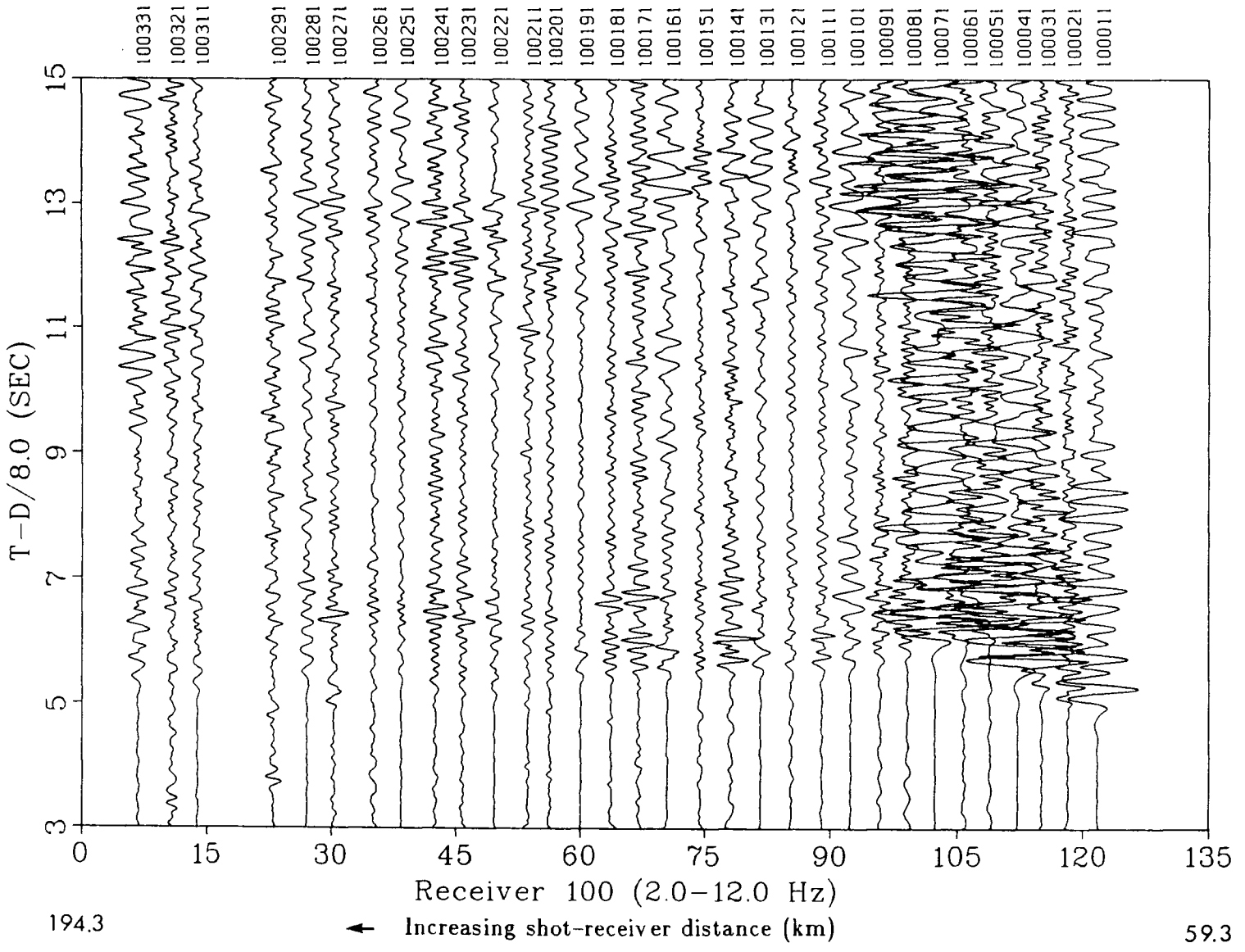
100331
100321
100311
100291
100281
100271
100261
100251
100241
100231
100221
100211
100201
100191
100181
100171
100161
100151
100141
100131
100121
100111
100101
100091
100081
100071
100061
100051
100041
100031
100021
100011
T-D/8.0 (SEC)
3
5
7
9
11
13
15
0
15
30
45
60
75
90
105
120
135
Receiver 100 (2.0-12.0 Hz)
194.3
← Increasing shot-receiver distance (km)
59.3